FAULT RIDE-THROUGH CAPABILITY AT WIND POWER PLANT INTERFACING A THREE-PHASE GENERATOR TO A DC-BUS

by

Inas Mohammed Osman Mohammed

Submitted in partial fulfilment of the requirements for the degree
Philosophiae Doctor (Electrical)

in the

Department of Electrical, Electronic and Computer Engineering
Faculty of Engineering, Built Environment and Information Technology

UNIVERSITY OF PRETORIA

November 2020

SUMMARY

FAULT-RIDE-THROUGH CAPABILITY AT WIND POWER PLANT INTERFACING A THREE-PHASE GENERATOR TO A DC-BUS

by

Inas Mohammed Osman Mohammed

Promoter: Prof. R. C. Bansal (University of Sharjah & University of Pretoria)

Co-promoter: Prof. M. N. Gitau

Department: Electrical, Electronic and Computer Engineering

University: University of Pretoria

Degree: Philosophiae Doctor (Electrical)

Keywords: Voltage control, fault ride-through, Vienna rectifier, wind power, transient stability, DC collection grid, fault clearance, smart grids, modular multilevel converter, permanent magnet synchronous generator

The increased demand for electricity has led to a global energy transition towards the use of renewable energy sources for power generation. Renewable energy has several advantages such as high efficiency, resource availability, cost competitiveness and environmental adequateness, compared to conventional fossil fuel power plants. Recent research studies have therefore focused on developing renewable energy technology. In fact, for alternating current (AC) collection grids, each wind energy conversion system (WECS) on a wind power plant (WPP) includes a wind turbine plus mechanical parts (i.e. gearbox), a generator (squirrel cage induction generator (SCIG), doubly fed induction generator (DFIG), permanent magnet synchronous generator (PMSG)), and a massive 50 or 60 Hz power transformer including controller circuit.

A wind farm with a direct current (DC) transmission link is considered for this study. For a wind farm employing DC collection grid, the massive power transformers in the WECSs are replaced by the power electronic converters. The power electronic converter is significantly more compact and smaller in size compared to a power transformer of identical features. High voltage DC (HVDC) power transmission and distribution systems play an integral role in power systems and renewable energy resources integration technology.

The WPPs have to play an essential function in maintaining grid stability due to the continuous progress in the number of grid-connected wind farms. This growth requires the wind turbine generator (WTG) on wind farm to stay connected to the power grid for any fault conditions. The fault ride-through (FRT) capability is the ability of WECS to stay connected for short periods of fault conditions. This expression can also be used to demonstrate the ability of a wind farm to participate in the voltage stability during grid faults. This study proposes integration of the wind energy conversion unit (WECU) three-phase controlled switch active converters. Two configurations for the converters are considered:

- Vienna rectifier-I
- Modular multi-level converters (MMC)

In these configurations, the switching loss is reduced due to a smaller number of switches used in Vienna rectifier, and low switching frequency in MMC compared with conventional active rectifiers. The dynamic behaviour of the overall DC collection grid is also investigated in terms of (voltage/current) signal perturbations. The small-signal based control method which limits the signal variations to about zero is employed. Intensive simulations are presented with the use of the power simulator (PSim, Rockville, USA) software, to ride-through several DC and AC system faults.

LIST OF ABBREVIATIONS

AC	Alternating current
BPA	Blade pitch angle
DC	Direct current
DFIG	Doubly fed induction generator
DPF	Displacement power factor
EMF	Electromotive force
EMI	Electromagnetic interference
ESS	Energy storage system
FACTS	Flexible AC transmission systems
FHC	Frequency hysteresis control
FRT	Fault ride-through
GSC	Grid-side converter
HVAC	High voltage AC
HVDC	High voltage DC
IGBT	Insulated gate bipolar transistor
LVRT	Low voltage ride-through
MCLS	Modified current-limit strategy
MMC	Modular multilevel converter

MOSFET	Metal oxide semiconductor field effect transistor
MSC	Machine side converter
PI	Proportional integral
PLL	Phase locked loop
PMSG	Permanent magnet synchronous generator
PR	Proportional resonance
PSim	Power simulator
PWM	Pulse-width modulation
QZSR	Quasi-Z-source rectifier
SCIG	Squirrel cage induction generator
SFCL	Supper-conducting fault current limiter
THD	Total harmonic distortion
VCO	Voltage controlled oscillator
VSC	Voltage source converter
VSR	Voltage source rectifier
WECS	Wind energy conversion system
WPP	Wind power plant
WTG	Wind turbine generator

ACKNOWLEDGEMENT

There are many people I need to thank and gratitude for helping me to complete this thesis. Without their constant encouragement and caring support the past five years would have been very difficult.

- My supervisors Professor Ramesh Bansal (University of Sharjah & University of Pretoria) and Professor Michael N. Gitau, and the Head of the Department Professor Raj Naidoo, for encouragement, and endless support technically and financially.
- My parents who sacrificed a great deal in order to give me my opportunities in life. I am truly blessed to have such parents and this thesis would not have been possible without their tireless patience and unselfish sacrifices during my studies.
- Further, I would like to thank my family, friends, and colleagues in the Department of Electrical, Electronic and computer Engineering for encouragement, and unlimited support.
- Finally, I would like to thank my husband Sohaib Osman for his continuous support during my PhD time despite his own challenge with his PhD studies at University of Pretoria, Mechanical Engineering Department, as he was sacrifing with his time to support me. I dedicate it to him and to our children.

TABLE OF CONTENTS

LIST OF FIGURES

LIST OF TABLES

CHAPTER 1 INTRODUCTION

1.1 PROBLEM STATEMENT

1.1.1 Context of the problem

A WPP generally consists of several WECSs interconnected either in series, radial, or series-parallel and injected into the main bus. One of the significant challenges in WECSs is to handle the discontinuity of wind and to protect the grid stability. Voltage stability is a substantial issue to be considered in a power system with large scale wind power integration. As wind power increases, the instability mode of the system changes from angle instability to voltage instability. In voltage instability, the rotor angle of the synchronous generator is average, but the wind farm voltage collapses.

When a considerable amount of wind power is integrated into a power system, the stability feature of the system undergoes significant change and the power of wind farms loses stability and cannot be controlled by the power electronic interface. A variable speed wind turbine can control the power rapidly and flexibly with power electronic converters [1-4].

The energy storage systems (ESSs) and power electronics are principal components to support the continuation of wind power [5-7], and this can be done with the use of FRT capability controllers.

1.1.2 Research gap

Most research studies on the design of DC collection grids for wind farm apply the traditional full-bridge active rectifiers as the topology of power converters in WECS [8]. The conventional full-bridge active rectifier contains large numbers of controlled-switches which increase the complexity of the controller circuit and affect the system efficiency because of the high switching frequency operation of the controlled switch, which reduces the reliability of the system [9, 10].

The motivation of this research is to improve the transient voltage-stability and FRT capability of the WPP. The improvement is made by including an interface between a three-phase variable speed AC synchronous generator and a constant DC-bus, based modular voltage source converters (VSCs), i.e. Vienna rectifier and MMC. To maintain high power, reactive power reduction should be considered, as well as conserving a constant DC-bus voltage.

1.2 RESEARCH OBJECTIVE AND QUESTIONS

This study aims to achieve an interface between three-phase AC synchronous generators running at variable speed integrated with a DC-link, with the use of power electronic converters feeding a DC or AC load. Three virtual wind farms are considered based on AC and DC load to improve the transient voltage stability and FRT capability. The interface is desired to ensure high energy efficiency by maintaining a constant DC-bus voltage. The study will include the following:

- Study the structure of several converters and select the most efficient rectifier and inverter
- Enhance transient voltage stability and FRT capability, and
- Ensure steady-state stability operation by designing a DC voltage controller.

1.3 APPROACH

A WECU consisting of generation unit and AC and DC side converters-based DC-link transmission system is evaluated with cost and efficiency considerations, which effectively realize power filtering, rectification, boosting, transmission, and distribution. DC voltage controller is designed to perform the steady-state stability operation. Simulations are done using PSim software to investigate the FRT capability of AC and DC faults for several operation modes.

1.4 RESEARCH GOALS

The central goal is the development of a WECS based DC transmission technology to improve system stability and FRT capability under several types of faults. The following three models are developed: (i) A three-phase Vienna rectifier-I connected with a PMSG and a DC load considering DC fault. (ii) A three-phase Vienna rectifier-I and MMC linked via a DC-link, and connected with a PMSG and AC load considering DC fault. (iii) A three-phase Vienna rectifier-I connected with a PMSG and a DC load considering AC fault.

1.5 RESEARCH CONTRIBUTION

The integration of the Vienna active rectifier-I with MMC based PMSG is a novel concept which opens up a discussion in this thesis, especially Vienna rectifier-I and MMC integrating with FRT controller circuits. The significant contributions of this research are summarized in three journal articles. The summary of these contributions is listed below:

- The PMSG integrated with a three-phase Vienna rectifier-I based WECS supplying a DC load is formulated and discussed. DC fault is applied and a fault blocking diode and control circuit is used for riding-through the fault. This work is published in a technology and economics of smart grids and sustainable energy (TESG-SE) Journal,

under the title, "Modelling and control of a Vienna smart rectifier-I for wind power systems integrated under transient conditions".

- Active converters (Vienna rectifier-I and MMC) integrated with PMSG supplying AC load are tested for riding through a DC link fault. This work is submitted to Electric power components and systems (EPCS) Journal under the title, "Fault ride-through capability of MMC based wind power plant integrated under a DC-link fault".
- PMSG integrated with Vienna rectifier-I supplying a DC load is applied to ride-through AC fault. This work is accepted for publication in EPCS Journal under the title, "Elimination of the voltage output fluctuations of a Vienna active rectifier-I integrated under unsymmetrical faults based wind power plant".

1.6 RESEARCH OUTPUTS

The publications relevant to this thesis are:

Inas M.O. Mohammed, Michael Njoroge Gitau, Ramesh C. Bansal and Kabeya Musasa, "Modelling and control of a Vienna smart rectifier-I for wind power systems integrated under transient conditions," Technology and Economics of Smart Grid and Sustainable Energy, vol. 4, no. 2, pp. 1-13, 2019.

Inas M.O. Mohammed, Michael Njoroge Gitau and Ramesh C. Bansal, "Elimination of the voltage output fluctuations of a Vienna active rectifier-I integrated under unsymmetrical faults based wind power plant," accepted for publication in *Electric Power Components & Systems*.

Inas M.O. Mohammed, Michael Njoroge Gitau and Ramesh C. Bansal, "Fault ride-through capability of MMC based wind power plant integrated under a DC-link Fault," *Electric Power Components & Systems* (under review).

1.7 THESIS OVERVIEW

This thesis focuses on FRT capability, including AC and DC faults in a WPP based DC transmission system.

In Chapter 2 a literature study on FRT capability of WPPs is provided, and comparative study on several types of active rectifiers.

In Chapter 3, wind turbine and PMSG modelling and control equations are provided, to determine the active rectifiers' electrical and mechanical behavior.

In Chapter 4 an intensive analysis and discussion for Vienna-I rectifier is presented, including the performance analysis of an AC to DC converter. Small-signal modeling of Vienna rectifier-I and MMC was also discussed, including the analysis equations that determine the behavior of the system which governs the system responses that are integrated with Vienna rectifier-I and MMC.

In Chapter 5 a DC voltage controller design is presented; in terms of current and voltage loop controller design, and a dq-frame controller is designed and discussed. The design criteria of the DC voltage controller is also discussed to maintain stable DC voltage at steady-state operation, and the system stability is demonstrated using bode plots.

In Chapter 6 a comprehensive simulations are applied and discussed for three virtual WPPs using PSim software.

In Chapter 7 a conclusion of the work that has been done and the recommendations and future research directions are provide.

CHAPTER 2 LITERATURE STUDY ON FAULT RIDE-THROUGH CAPABILITY AND ACTIVE THREE PHASE RECTIFIERS

2.1 CHAPTER OVERVIEW

The literature studies of capabilities to ride-through faults interfacing several types of converters are discussed in Section 2.2. Section 2.3 compares various topologies of rectifiers to determine the most suitable topology for converting a three-phase input from a generator feeding AC or DC load through a DC bus. The summary of this chapter is presented in Section 2.4.

2.2 FRT CAPABILITY

Since the number of grid-connected wind farms is continuously increasing, the WPP must play a considerable role in maintaining grid stability, which requires that the WTG stays linked to the power grid during any fault conditions. The FRT is an expression used to explain the ability of a wind farm to contribute to the grid during faults, which is critical for assuring the power system stability. The flexible FRT strategy on high wind power penetration increases the FRT capability of the wind farm groups and reduces the wind power contraction during faults [11, 12].

2.3 FRT STRATEGIES BASED VARIABLE SPEED WTGS

The control strategy to improve the FRT capability of a power system based synchronous generator decreases the peak values of the rotor current, DC-link voltage and electromagnetic torque at the instants of occurring and clearing the grid faults [13]. The studies demonstrated that the superconducting fault current limiter (SFCL) based wind turbine connected with the DFIG can reduce the voltage dip effect [14]. A comparison between the active and a common inductive SFCL is summarized to find the difference as follows.

- Installing the inductive SFCL could practically decrease the fault currents flowing through the DFIG's stator and rotor windings.
- Conducting the active SFCL can naturally compensate the DFIG's terminal-voltage and limit its output power fluctuation.
- Involving the active SFCL can only suppress the DFIG's power oscillation amplitude. However, it may not supply a more promising effect on limiting the excess active power during the system fault [15].

A comparative study was done on the determination of critical clearing time using dynamic voltage restorer at an induction generator-based wind generation system to improve the FRT capability. It was recognized that when operating slip is high, critical clearing time is the same for both cases, while it differs significantly at lower operating slip values [16]. A fuzzy controller can improve the FRT capability of variable speed wind turbines equipped with a DFIG. The controller is designed to compensate for the voltage at the point of common coupling [17] by simultaneously regulating the active and reactive power.

An active crowbar protection system can enhance the FRT capability of DFIG based WECS [18]. Three methods to implement the FRT operation of the wind farms were discussed as follows. (i) The rotor current of DFIG was limited by introducing a rotor-side protection circuit. (ii) The DC bus voltage was limited by a DC energy absorb circuit. (iii) Static compensator was used to increase the low-level voltages of the wind farm. The results

specify that the methods proposed can limit the rotor short-circuit current and the DC voltage of the DFIG-wind turbine, but mostly the voltage support to the power system during the fault depends on static compensator installation place [19].

In [20] the blade pitch angle (BPA) control and a protective relay system are used for FRT capability. The use of the protective relay system for a wind turbine can improve the pitch controller to compel the wind turbine to respond rapidly to the voltage dip. When the BPA equals to zero, the power consumed by the windmill is proportional to the performance coefficient. The maximum performance coefficient is fulfilled at enhanced rotational speed when the BPA is equal to zero. The BPA is connected to prevent the generator from over speed; moreover to avoid shifting the operation from the point where the performance coefficient is at its maximum value (BPA equal to zero) by reducing the wind power. When BPA technique is applied significant response limitations are observed due to high functional forces resulting from restoring power at a high rate during the fault occurrence [21-23].

The required capacitor power is proportional to the sag voltage, and the required capacitor size will increase if the voltage sag period increases. In this case resizing the fully rated converters is required, and the capacitor sizing procedure is expensive and an impossible solution [24, 25]. To manage the excess power and restore the power balance in the active crowbar rotor circuit, a braking resistor technique is included in the DC circuit. The active crowbar uses semiconductor switches such as insulated gate bipolar transistors (IGBTs) or gate turn off, which add extra cost to this approach. The active crowbar technology can be used along with the BPA technique to compensate for the continued voltage sags, which lead to high power dissipation. The BPA technique reduces the captured wind power by its controllers, which will decrease the power imbalance and hence, the required braking resistor power.

ESS is one of several methods used for FRT enhancement in WECSs; it can maximize the reliability of power to the loads, and eliminate the fluctuations when connected with a WTG. ESS can help enhance the low-voltage ride-through (LVRT) capability for wind turbines by

providing an alternative path for the generator currents. The merits of this type of compensation are (i) long life (ii) fast response (iii) high scalability, and (iv) low price requirements & materials maintenance. The limitations are that the ESS technique requires proper sizing of the machine side converter (MSC) and it is sensitive to fault severity. The control of fully rated converters can be done in the branches of the followings (i) control of MSC (ii) control of grid side converter (GSC) (iii) control using boost converter [26-30]. Several techniques have been introduced for voltage and reactive power improvement at the point of common coupling with the use of flexible AC transmission systems (FACTS), shunt and series compensation techniques [31- 35]. In [36], the FRT capability for the DFIG using feed-forward transient current control, and direct transient current control methods have been proposed.

The chopper circuit is allocated alongside the DC-link capacitor. The circuit structure is of an IGBT switch and a resistor. It is a cost-effective strategy to enhance the LVRT capability because there is no energy storage-based system and the resistor of the chopper circuit can be over-heated due to the power-consumption [36]. A storm-control is presented to permit variable speed wind turbines to work at wind speeds higher than 25 m/s, without an increase in the structural loads [37]. The work implies pitch angle rates up to 60-70 degrees to limit the aerodynamic forces.

A storm controller is introduced, examined and matched with the conventional control strategy running up to 50 m/s. The controller was limiting the rotor loads. In [38] protection designs for various power electronic converters topologies in order to protect the vulnerable types is proposed. For DFIG, rotor overcurrent representations are obtained for several fault conditions and a series resistor-based protection circuit is recommended to protect the MSC without short-circuiting the rotor winding. Compared with conventional crowbar protection, this is beneficial in avoiding grid voltage decay resulting from reactive power consumption. It is concluded that the proposed method can significantly enhance FRT capability of the DFIG system.

Field-oriented control and direct torque control are the most popular FRT strategies for PMSG [39]. The maximum power point tracking capability designs assist in the peak power extraction throughout different wind speed conditions. The objective of the technique is to provide reference speed ω_{m}, reference electromagnetic torque T_e, or reference power P_s, such that control operation for MSC requires the WECS to follow the maximum power point trajectory. The operating domain for the maximum power point tracking control is between the cut-in and rated wind speed [40, 41]. When PMSG has been integrated with wind-turbine, studies show many advantages of the PMSG, such as:

- Can ride-through several grid-faults
- Able to cut-out from the grid instantly in case of a fault and resume rapidly into regular operation after the fault
- Has the ability to mitigate the intermittent power variation from the wind
- High power density
- Less maintenance needed
- High reliability

For the given merits, a variable speed PMSG based wind-turbine is considered for this work.

2.4 FRT STRATEGIES BASED MMC

Several research works have been done for MMC for riding-through several AC and DC faults. A thorough comparison between the two VSC-HVDC transmission technologies is presented [42], which are neutral point clamped and three-level MMC. The comparison concentrated on reliability aspects, such as their capability to ride-through the faults that involve the symmetrical and unsymmetrical faults. There is also flexibility of the control in both technologies. The results of the investigation are summarized as follows:

- The carrier-based sinusoidal pulse-width modulation (PWM) technique when applied for neutral point-clamped VSC-HVDC transmission systems, performs better than when it's controlled using space vector PWM. Also, they are capable of

riding through different types of faults, such as symmetrical and unsymmetrical faults.

- MMCs based VSC-HVDC transmission systems are capable of riding through different types of AC faults, and have more advantages over conventional VSCs.

Therefore, the use of MMCs in HVDC transmission systems applications is preferred, because with an increased number of levels they generate high output voltage with low total harmonic distortion (THD), improved system reliability and FRT capability. In [43] a DC FRT capability for a MMC using a diode clamped sub-module is proposed, and it was observed that the fault current can be eliminated. Then by blocking additional IGBTs, MMC can rebuild the DC link voltage and can automatically return regular power transmission for non-permanent faults. The principle of fault removal and the voltage stress of new semiconductors has been analyzed. Simulation results confirmed the efficacy of the suggested MMC topology and the proposed protection scheme. In the case of employing the diode clamp sub-module structure, the expected rated voltage of the multilevel converter is half that of MMC, resulting in low cost of the device.

A simulation work for a frequency hysteresis control (FHC) and a modified current-limit strategy (MCLS) for enhancing the FRT capability of a VSC-HVDC link supplying passive industrial installations is proposed in [44], given that industrial loads are more susceptible to voltage drops than frequency variations. An investigation was done for the principal factor influencing the AC voltage.

The active and reactive power obtained from the inverter can be given as follows:

$$P_s = -\frac{3}{2}V_{sd}i_{sd} - \frac{3}{2}V_{sq}i_{sq} \tag{2.1}$$

$$Q_s = \frac{3}{2}V_{sd}i_{sq} - \frac{3}{2}V_{sq}i_{sd} \tag{2.2}$$

where i_{sd}, i_{sq} represent the dq-axis current components. V_{sd}, V_{sq} are the dq-axis voltage components of the VSC.

The q-axis voltage component at the point of common coupling is:

$$V_{sq} = V_s \cos\left(\theta + \frac{\pi}{2}\right) = -V_s \sin\theta \tag{2.3}$$

In transient states, the magnitude of V_{sq} is negative and small, from (2.2) V_{sq} is the coefficient of i_{sd}. Therefore, at the fault's conditions i_{sd} has a small impact of the reactive power, because i_{sq} is the major factor that can affect the reactive power in steady-state and transients, thus the MCLS can be given using (2.4):

$$i^*_{sd\ lim} = \sqrt{i^2_{lim} - i^2_{sq\ ref}},\ i^*_{sq\ lim} = i_{lim} \tag{2.4}$$

where i_{lim} is the current limit of the VSC, which is set as 1.1 times the total load. The $i^*_{sd\ lim}$ is obtained according to $i^2_{sq\ ref}$.

The concept of the MCLS is to boost the current component i_{sq} of the q-axis, during the fault time. The primary role of the FHC is to create a new reference frequency of the VSC output voltage based on the amount of the AC voltage at the point of common coupling. When the voltage declines due to grid fault, the FHC reduces the set frequency of the VSC at the receiving side. Throughout the fault period, the reduction of V_{sq} can also increase i_{sq}, which can increase the reactive power output provided by the VSC at the receiving side.

Three steps are discussed for developing the control methods. Step 1: to improve the voltage stability more efficiently, the principal factor which can affect the AC voltage in the passive industrial system is investigated. Step 2: the modified current-limit strategy is introduced to enhance the AC voltage in transient conditions, according to the analytical results. Step 3: the frequency hysteresis control is added to the VSC controller with the modified current-limit strategy to give the strategy a better control result which can also improve the AC voltage of the passive system. It is concluded that the control strategies proposed for this work could improve the voltage stability of the passive industrial installations efficiently.

In [45] a structure to perform DC-FRT capability in multi-terminal DC networks using H-bridge MMC is proposed. The investigated system consists of four VSCs for HVDC transmission.

The DC fault response of the system was analyzed, and the controller is designed based on the selective DC fault detection techniques. The current sensors installed at the ends of each line part in the network send the signals to the controller. When the fault occurs, the protection of the converter is enabled. In conclusion, if there is a fault in any part of the grid, only the faulty line part due to overcurrent at one cable is selectively detected. As a result, H-bridge MMC achieve worse than grids which make use of half-bridge MMCs combined with fast DC breakers.

An improved control approach that uses the generated negative sequence voltages to easily inject the negative sequence currents throughout unsymmetrical AC faults is proposed [46]. The motivation of the analysis was the drawbacks of controlling the fault currents at zero-sequence during unsymmetrical AC faults. The overvoltage of phases through unsymmetrical AC faults is controlled by modifying the setting of the positive sequence voltage reference for the network developing offshore HVDC converter, which takes the recognized zero and negative sequence voltages into consideration. The drawback of the project was the high risk of protection mal-operation due to absence of fault currents, which also does prevent the recovery of AC voltage in post-fault.

The single thyristor method is one of several technologies that have been used to protect the freewheeling diode in the active switches during faults. A thyristor is commonly connected in parallel to the AC terminals of the MMC sub-module for sharing the fault current with the freewheeling diode. This approach can only prevent semiconductor devices, but not reduce the AC fault current feeding the DC side. A suspension for this limitation was presented later by employing double thyristors [47]. Some topologies are used to permit adequate handling of DC-side short circuits after reducing power losses compared to implementation with full-bridges. The semi-full-bridge model is one of the methods [48, 49], which require parallel connections of capacitors during regular operation as well as the H-bridge model, which controls the capacitor voltage balance when the converter DC-link voltage fails during DC faults.

2.5 ACTIVE RECTIFIERS

This section discusses the topologies of several active three-phase converters to identify the most suitable rectifier type for converting a variable voltage-variable frequency generator output to a DC voltage. The various characteristics of several rectifier topologies and control techniques are compared to identify the most suitable one for converting a three-phase input from a generator type input to a constant DC output voltage for this work.

The conventional converters have the following limitations [50-52]:

- Only a buck or a boost converter, i.e. their attainable output DC voltage is higher or lower than the input AC voltage.
- Susceptible to electro-magnetic interference (EMI), which reduces system reliability.
- Contains many controlled switches compared to Vienna rectifier, rectifier switching action generates high-frequency harmonics, which affects efficiency.

2.6 VOLTAGE SOURCE RECTIFIER

The voltage source rectifier (VSR) is one of several types of conventional rectifiers. A basic VSR-HVDC, as shown in Figure 2.1, consists of two converter stations which use series-connected active-switches (i.e. MOSFET (metal oxide semiconductor field-effect transistor)). It has been used in several high power applications [50] to transform three-phase AC voltage into a DC at the front-side of the DC-link, due to its several advantages, such as:

- The system can be interfaced easily
- Lower environmental impact compared to line commutated converter
- Can control both real and reactive power
- Low space requirements

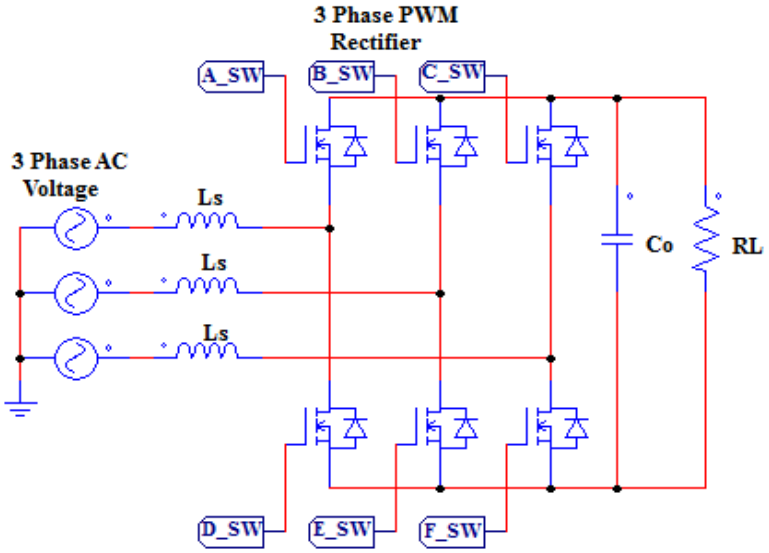

Figure 2.1. Three-phase VSR topology [53]

On the other hand, there are some demerits of the VSR, which can be summarized as:

- High harmonic distortion
- High stresses resulting in high-frequency noise [50-53]

2.6.1 Z-source and quasi-Z-source rectifier

Z-source and quasi-Z-source rectifiers (QZSR) structure have been proposed to overcome the traditional VSR problems. Figures 2.2 and 2.3 show Z-source and QZSR topologies.

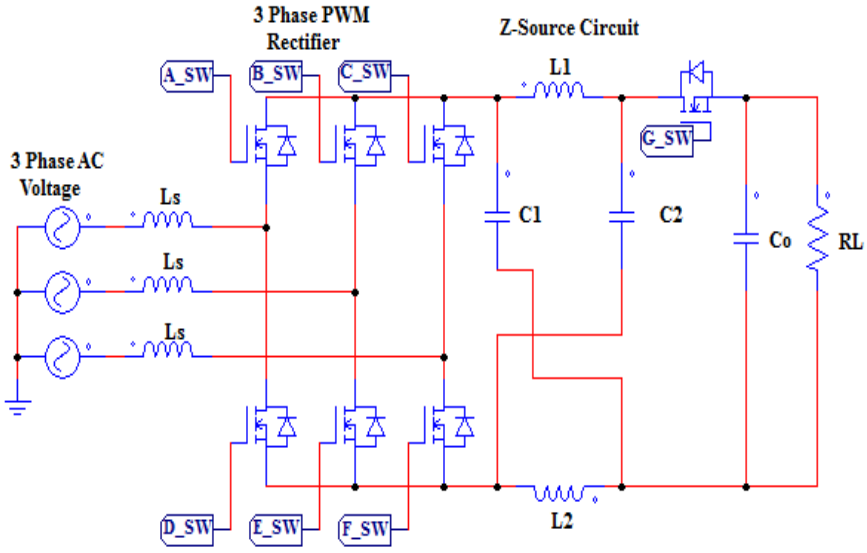

Figure 2.2. ZSR topology [53]

Several merits of Z-source and QZSR can be summarised as follows:

- The possibility of a cascade connection of Z-source rectifier (ZSR) allows boosting the voltage two to three times [54].
- Power flows in a bidirectional way in the use of a three-phase ZSR, unlike in conventional rectifiers [55].
- Unlike the ZSR, the output capacitor, C_0 of the QZSR filters only the low amplitude current harmonics flowing through inductor L1; therefore, the voltage and current rating of the output capacitor for the QZSR are much lower than those of the ZSR output capacitor.
- Less EMI problems in QZSR compared to ZSR, due to less complicated installation of components in QZSR [56].

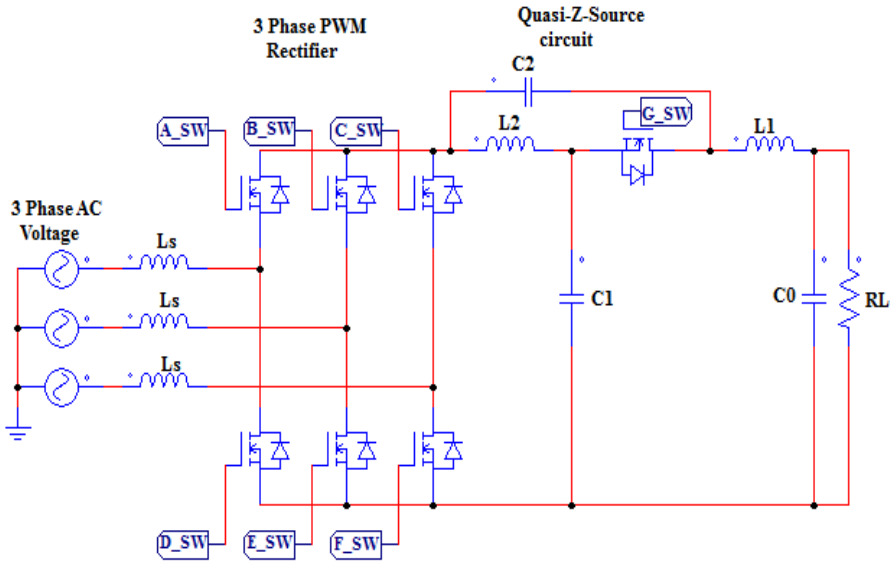

Figure 2.3. QZSR topology [57]

The limitations of ZSR and QZSR can be described as follows:

- The voltage across ZSR capacitors is larger than the input voltage; this enforces the use of larger capacitors, which increases the overall cost and size [57].
- The inrush current and resonance in the ZSR network at startup are not suppressed.
- Higher switching losses compared to modular converters [58]
- Lower-rated capacitors for QZSR
- The blocking voltages of capacitors C_1 and C_2 in the ZSR are equal and higher than the blocking voltage of capacitor C_2 in the QZSR; this results in a lower capacitor C_2 voltage rating in the QZSR [59-61].
- Compared to Vienna active rectifier and MMC, the rated capacitors are lower for ZSR and QZSR, and the EMI is less in Vienna rectifier and MMC.

2.6.2 Vienna rectifier

The Vienna rectifier shown in Figure 2.4 [62], is a three switch rectifier that features a split output DC-bus. It has the following advantages when used over HVDC transmission systems:

- Implementation is more straightforward compared to other rectifiers which have many numbers of switches [63].
- The control is only required for three switches, which makes it uncomplicated.
- Low THD of input currents compared with conventional rectifiers.
- High efficiency compared with conventional rectifiers, due to a smaller number of switches which results in fewer losses.
- There are many switching methods, which are different from those of three-level topologies [64].
- It is more suitable for HVDC systems because the switch only sustains half of the DC-bus voltage.

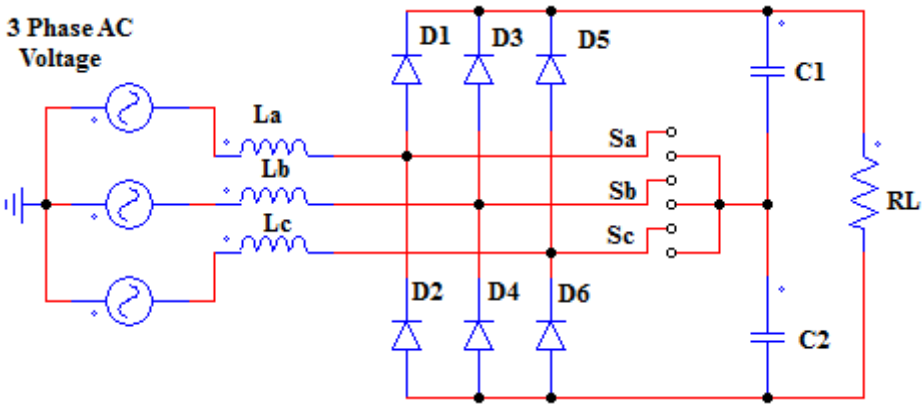

Figure 2.4. Vienna rectifier topology [64]

The drawback of the Vienna rectifier implementation in the HVDC system is the high boost-ratio and hence, high output voltage required [65].

2.6.3 Vienna rectifier-I

The three-phase Vienna-I topology as shown in Figure 2.5, involves a single switch per power cell [66]. The rectifier structure has three cells, each one is a bridge rectifier, the mid-points of one leg of each rectifier are connected to a middle link of output capacitors. The middle link of the capacitors is functionally connected to a neutral power by connecting the

middle link of one arm of the diode bridges of all three phases. For boost operation, each bridge cell is connected to an inductor in the input and output sides, as shown in Figure 2.5. The interface to be developed is therefore expected to address input and output side harmonics concerns.

Vienna-I rectifiers are widely used in several high voltages, high power applications because of the following merits [66-68]:

- The capability of double boosting effect because each bridge consists of two inductors in input and output sides, which can improve the rectifier features.
- The ability of buck-boost operation compared to conventional full-bridge rectifiers.
- Allows transmitting the energy to the DC capacitors even if the mains voltage is positive or negative.
- Involvement of a single switch per power cell.
- Permits building a highly reliable rectifier.
- While it is used for three-phase applications, it could even be used for single- phase rectification.
- Obtainability of three DC output voltages.
- The DC ripples decrease for a given capacitor value.
- Less input current harmonic distortion than the conventional topologies [68].
- The possibility of continuous current and power-factor correction operation mode compared with conventional rectifiers.
- Less number of active semiconductor devices.
- High power density due to the three switches which are based on three-level configurations.

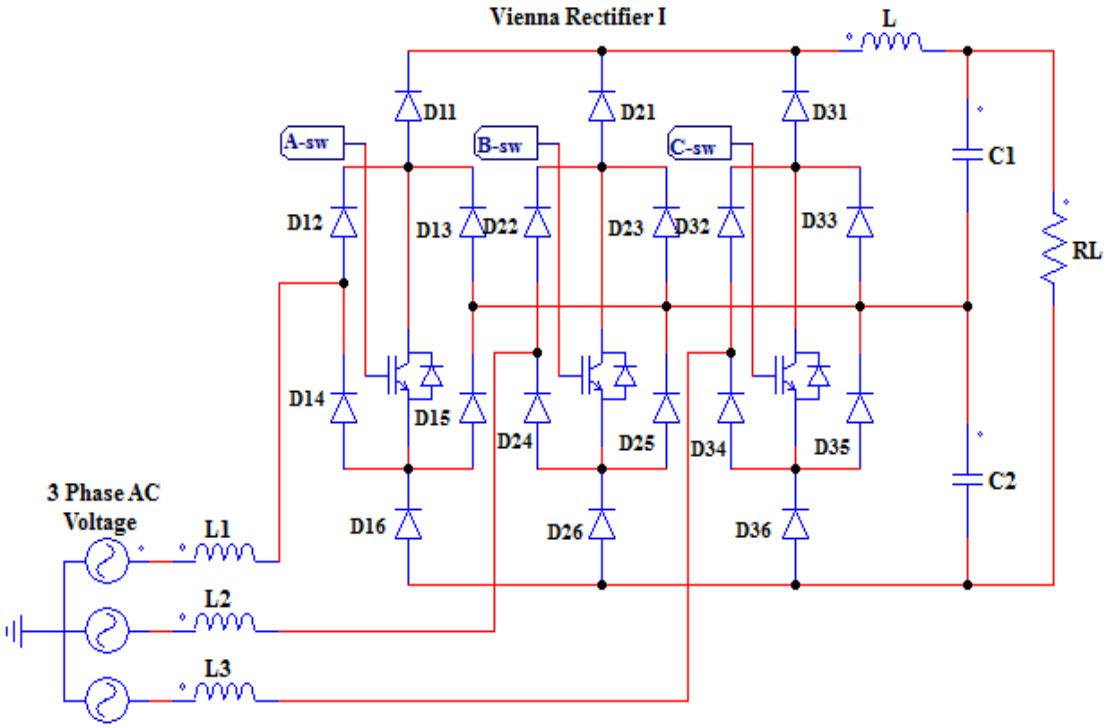

Figure 2.5. Three-phase Vienna-I rectifier topology [12, 66-68]

The drawback of Vienna-I rectifier is related to implementation of two inductors [67].

2.6.4 Vienna-II rectifier

The Vienna-II rectifier is a power circuit of a single-stage three-phase boost type PWM rectifier system; Figure 2.6 illustrates the topology. The rectifier has several merits over conventional rectifiers which can be listed as follows [69].

- The structure of the power and control circuits is simple
- The input current shape is sinusoidal
- No low-frequency harmonics of the output current
- The maximum volt seconds resulting across the rectifier are limited and are defined by the output voltage and the pulse period
- The blocking voltage of the output diodes is defined by the output voltage (with low inductance) and is independent of the main voltage
- There is more than one output voltage

- High-frequency isolation of the output voltage

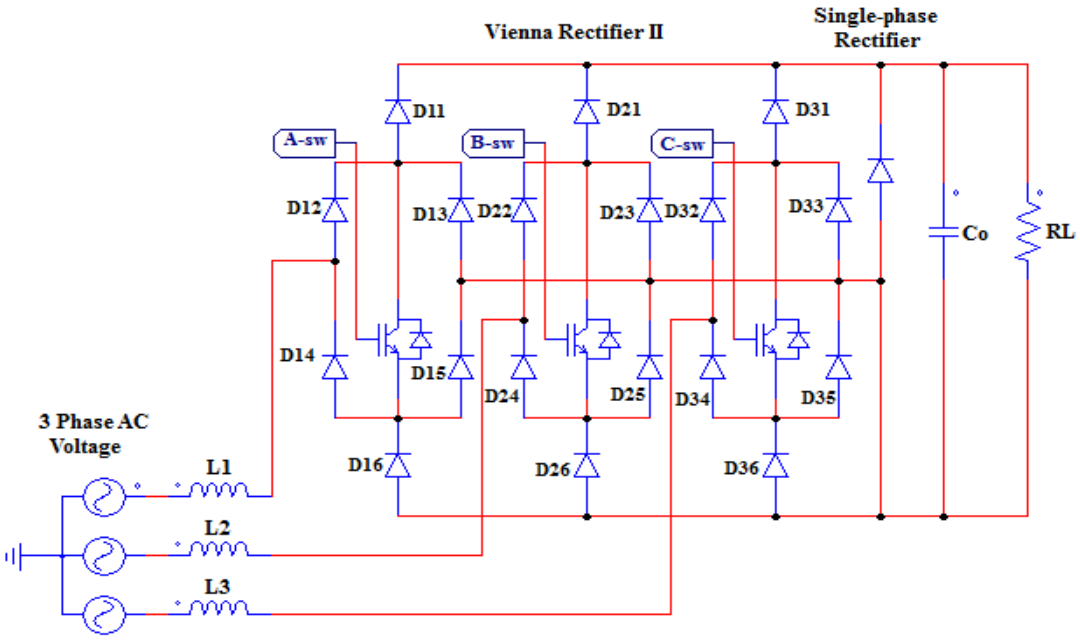

Figure 2.6. Vienna-II rectifier topology [69]

The disadvantages of using a Vienna-II rectifier over HVDC systems can be summarized as:

- It is only a boost type of operation
- There is a discontinuous output current shape
- There is a right-half-plane zero of the transfer function between the average output current and the modulation depth of the converter
- A limitation of the rectifier input voltage of the blocking voltage across the power semiconductors on the input side is required.
- No direct current limitation and no direct startup for an output voltage short circuit are possible [69].

2.6.5 Modular multilevel converters

The MMC is structured of a modular arm topology designed by a cascade combination of many chopper cells with floating DC capacitors as shown in Figure 2.7. These cells are called sub-modules and can be efficiently constructed into a converter for high- or medium-voltage power conversion systems.

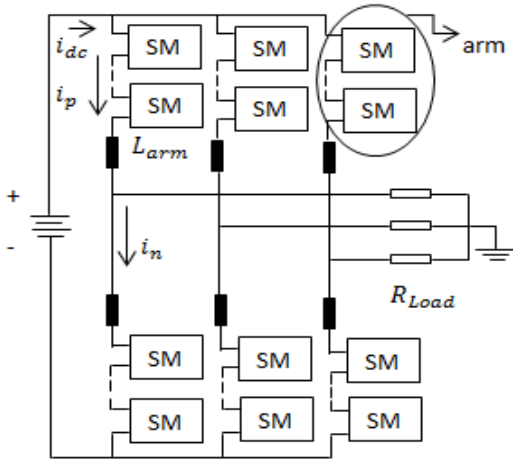

Figure 2.7. MMC topology [70]

The merits of using MMC are:

- Less harmonic distortion due to less switching frequency
- Ability of self-isolation of faults
- Can be used for medium and high voltage applications by controlling the number of sub-modules

The demerit is that, the control scheme is more complicated [70].

2.7 CHAPTER SUMMARY

Section 2.2 presents literature studies for FRT capability. It was observed that limited and complicated types of controllers were applied for riding-through AC and DC faults; most of the studies that have been done for FRT capability are based on DFIG. An analysis of several

types of active power converters to determine the most competitive one was provided in Section 2.3.

The rectifier topologies discussed demonstrate that the Vienna-I rectifier and MMC offer the best compromise in terms of performance, active switch numbers and controllability. There is no prior research which focused on the literature on Vienna rectifier-I integrated with MMC. It proposes the same or better performance than most topologies while utilizing fewer switches, in the case of Vienna-I rectifier, and ability of self-isolation of faults, in the case of MMC. With the double-boost constant switching frequency controller, the Vienna-I rectifier is easy to control and it is just as easy to set-up an equivalent control mode.

CHAPTER 3 PMSG BASED WECU, DYNAMIC MODELLING AND ANALYSIS

3.1 CHAPTER OVERVIEW

Many researchers have paid attention to the development of WPPs technologies due to their low running cost, lower environmental impact and resources availability compared to conventional fossil fuels power plants [71, 72]. A wind farm connection in a power system network needs solving numbers of technical problems to ensure safe operation and maintenance of these sources. Fixed speed WTGs do not employ power converters in WECS. Section 3.2 discusses the wind turbine modelling, which includes the wind power equation and a comparative study between AC and DC-based power transmission.

The dynamic model of a PMSG is shown in Section 3.3. The control parameters (voltage, current, frequency) of SCIG are done using the static compensators or flexible AC transmission system devices installed on the grid [73]. The disadvantage of this topology is that no tracking of maximum wind power mechanism is provided. However, for the variable speed wind turbine, the power electronic converters are employed in the WECS. The DFIG and PMSG are the most used types of generators for the WECS based variable speed wind turbine. The PMSG has been recognized as the most efficient generator technology used in wind power systems and has several advantages discussed in this chapter [72]. The summary of this chapter is provided in Section 3.4.

3.2 WIND TURBINE MODELLING

The growth of wind power is due to many problems faced by fossil fuel power generation. In a WECS the kinetic energy of the wind is converted into mechanical energy and transmitted to the generator through a shaft coupling, which in turn is converted into electrical energy.

The mechanical power converted from the kinetic energy captured from the wind can be written as [71-74]:

$$P_t = P_w \times C_p(\lambda, \beta) = \frac{1}{2}\pi\rho r^2 C_p(\lambda, \beta) V_w^3 \quad (3.1)$$

where, P_t is the wind-turbine output power, P_w is the wind power, C_p is power coefficient (dimensionless) which is a function of β "blade pitch angle" and λ "the tip speed ratio", ρ is the air density (1.225 kg/m^3), r is the blade radius (m), and V_w is the velocity of the wind (m/s). The power is proportional to the cube of wind velocity and the square of the radius of the air stream created by the blades.

The tip speed ratio is given as follows:

$$\lambda = \frac{\omega}{V_w} \times r \quad (3.2)$$

where ω is the rotational speed in radians per second.

3.2.1 Wind farm-based AC collection grid

Conventional wind farms are realized using several WECUs based AC transmission systems. Each WECU includes a wind-turbine with mechanical parts (wind-turbine blades, gearbox, and the shaft), a generator (PMSG, SCIG, and DFIG), and a large 50 or 60 Hz power transformer (step-up). The transformer also contains a large number of magnetic components employed in the power transformer, which makes the WECUs less compact and not strong enough to withstand the high wind speeds.

The connection modes can be parallel, series, series-parallel, ring, radial, or star [75]. The wind farm output power is transmitted through high voltage AC (HVAC) transmission lines or cables to the distribution side, which also includes large transformers (step-down). However, due to environmental issues, the wind farms are located far from the consumers, which increases the total loss of the system.

3.2.2 Wind farm-based DC collection grid

The HVDC transmission technology will be a better option due to high charging currents associated with AC cables for an extensive HVAC transmission system. The number of DC cables needed for the same power rating is reduced, which decreases the cost, losses, corona loss and radio interference. It is also easy to integrate with renewable energy sources with uncomplicated control strategies at low cost. The system efficiency is higher due to the absence of reactive power. Nevertheless, HVDC comes up with the lowest running cost and reliable performance after approximately 50 km distance for underground cables and 600-800 km for overhead lines with the same transmission capacity. Figure 3.1 shows the financial cost of overhead transmission lines with HVAC and HVDC transmission systems.

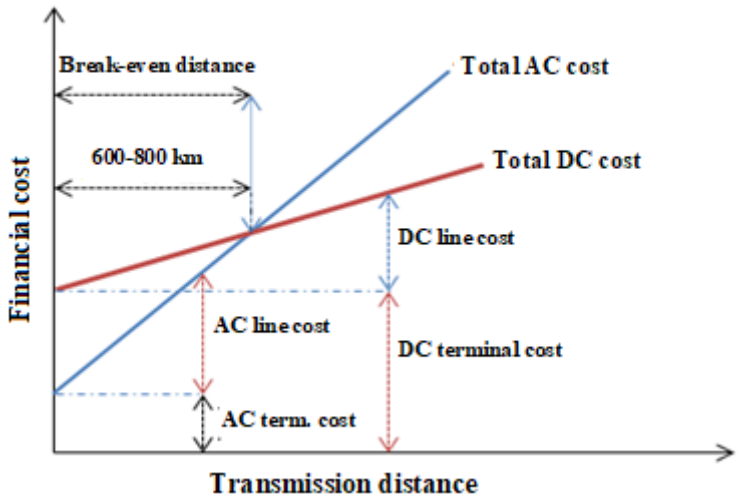

Figure 3.1. Cost estimation between AC and DC transmissions [12]

As shown in Figure 3.1, after the break-even distance, the cost of a HVDC transmission line is considerably less than that of HVAC.

This work considers a wind farm with a DC collection grid. The large size transformers are replaced by compact power electronics converters [12, 76-79]. For a wind farm-based DC collection grid, the connection modes can be parallel or series connection. Parallel connections increase the current rating and thus obtain a high enough power. In series connections, voltage is built high enough for the HVDC collection grid [80, 81].

3.2.3 Types of wind turbines

Wind turbines are categorised into two primary groups: horizontal-axis wind-turbine and vertical axis design. Horizontal-axis wind-turbine either has two or three blades, and the rotor shaft and electrical generator are mounted on top of a tower. This structure has many advantages, such as high efficiency, and can capture high wind speed. The disadvantages are related to difficulty in accessing generator for maintenance. The second type is vertical-axis wind-turbine, here the rotor shafts are arranged vertically, and the main advantage of this category is the ability to place the unit on the ground. This allows easy maintenance and it can receive the air from any direction (no yaw control needed). The drawbacks of this topology are lower wind speed, less efficiency and lack of self-starting ability [82].

3.3 DYNAMIC MODEL OF A PMSG

A WPP generally consists of many WTGs linked jointly at the main bus. WTGs are grouped into two categories [83-86]:

1. Fixed speed WTG, e.g. the wind-turbine with a SCIG.
2. Variable speed WTG, this group is classified into two types as follows:

   (i) Full rating converter-based wind turbine, such as PMSG.

   (ii) Partial rating converter-based wind turbine, such as DFIG.

The demerit of fixed speed WTG topology is that no tracking of maximum wind power mechanism is provided. However, the variable speed WTGs can monitor the power rapidly and flexibly with active power electronic converters. One of the considerable challenges in WECSs is to handle the discontinuity of the wind to protect the grid stability. The power electronic converters and energy storage systems are substantial components to maintain the continuation of wind power.

PMSG has several merits and is the most considered type of generators for the WECS based variable speed wind-turbine synchronous generators (does not allow more than 30% speed variation). PMSG can provide a continuous load for the power consumers; with power electronics' assistance. Power can be monitored rapidly and flexibly with the help of active power electronic converters. The full-rating converters cut-out the synchronous engine speed from the grid frequency and produce flexible control over a wide range of speed [87, 88].

The PMSG is connected to the grid with a MSC and a GSC through a DC-link. Figure 3.2 shows the PMSG based wind-turbine which is modelled and discussed.

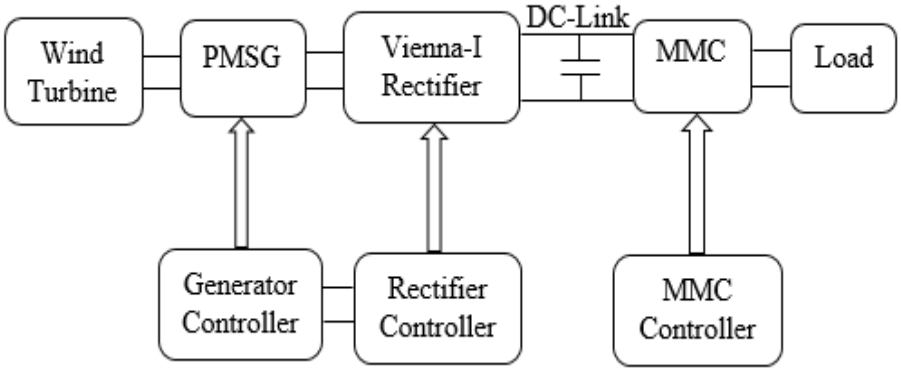

Figure 3.2. PMSG based wind power system.

The output power of PMSG is expressed as follows:

$$P = \frac{3V_S V_C}{X_S} \sin\delta \tag{3.3}$$

where V_s is the output voltage of the PMSG (or stator voltage), V_c is the input voltage to

the power converter, X_s is the synchronous reactance, and δ is the power angle.

Voltage equations of the PMSG in the d-q frame can be formulated as follows [89]:

$$V_{sd} = R_s i_{sd} + \frac{d\emptyset_{sd}}{dt} - \omega_{dq}\emptyset_{sq} \tag{3.4}$$

$$V_{sq} = R_s i_{sq} + \frac{d\emptyset_{sq}}{dt} + \omega_{dq}\emptyset_{sd} \tag{3.5}$$

where V_{sd} and V_{sq} are the stator voltages of the d-q frame, R_s is the stator resistance, i_{sd} and i_{sq} are the stator currents of the d-q frame, ω_{dq} is the rotor angular speed. $\emptyset_{sd}$ and $\emptyset_{sq}$ are the stator flux linkage in the d-q frame, and can be presented as follows:

$$\emptyset_{sd} = L_{sd} i_{sd} + \emptyset_{rd} \tag{3.6}$$

$$\emptyset_{sq} = L_{sq} i_{sq} \tag{3.7}$$

where L_{sd} and L_{sq} are the stator inductances of the d-q frame and $\emptyset_{rd}$ is the rotor permanent magnet flux linkage.

The mechanical equation of the PMSG can be expressed as [90]:

$$J\frac{d\omega}{dt} = T_e - T_m - f\omega \tag{3.8}$$

The electromagnetic torque delivered to the generator can be expressed as:

$$T_e = \frac{3}{2}p(\emptyset_{sd} i_{sq} + \emptyset_{rd} i_{sq}) \tag{3.9}$$

where p is the numbers of pole pairs, $\emptyset_{sd}$ is the stator permanent magnet flux linkage.

3.4 CHAPTER SUMMARY

This chapter discussed some of the components that describe the distributed power grid network; these include a comparison between DC and AC transmission links for a wind farm. A description of the control technology implemented by each WECU of the wind farm is provided. It was observed that the DC-link transmission is a better candidate for technical

and economic benefits. The dynamic modeling of a wind-turbine and PMSG which has been applied for this work was also discussed. The PMSG is the most practical generator model following variable-speed generators that are selected to integrate with the grid.

CHAPTER 4 ANALYSIS AND SMALL SIGNAL MODELLING OF VIENNA-I RECTIFIER AND MMC

4.1 CHAPTER OVERVIEW

The Vienna rectifier-I was chosen as the most convenient rectifier topology for converting a generator output AC power into a DC power in a WPP; for its excellence over conventional rectifier topologies discussed in Chapter 2. In Section 4.2, the performance analysis of AC to DC converters is discussed. In Section 4.3 the switching power loss that occurs instantaneously during ON-OFF transitions is discussed. The criteria for selecting power converters is shown in Section 4.4. Section 4.5 shows the Vienna rectifier structure and analysis, which provides the mathematical models that depict the state space equations for a Vienna-I rectifier as small-signal modelling. The transfer function that represents the model is also provided.

Section 4.6 shows the MMC structure and analysis, as a GSC, MMC has been used for this work. One of the main technical challenges of this inverter is complicated construction with several sub-modules per arm. A precise model can be obtained to design an appropriate control strategy. The small-signal modelling of this converter is provided according to the state-space equations. The summary of this chapter is given in Section 4.7.

4.2 PERFORMANCE ANALYSIS OF AN AC-DC CONVERTER

The output voltage of a rectifier is DC, but it contains ripples. The ripple value should be decreased to the smallest possible amount, and the rectifier input current should be managed to be as close to sinusoidal and in phase with an input voltage as possible, to enhance power factor. More parameters must be considered to minimize the harmonic content of the voltage and current waves to improve the rectifier performance [91, 92]. The rectifier output voltage contains two components: DC value, and AC ripple value.

The output DC power is given by (4.1):

$$P_{dc} = V_{dc} \times I_{dc} \tag{4.1}$$

where V_{dc} is the average DC output voltage, and I_{dc} is the average DC output current.

The rectifier output AC active power is written as follows:

$$P_{ac} = V_{rms1} \times I_{rms1} \tag{4.2}$$

where V_{rms1} is the root mean square or rms value of the rectifier output ripple voltage, I_{rms1} is the rms of the current ripple wave.

In an ideal rectifier, the ripple voltage and current should equal to zero [93]. Many factors affect the power system efficiency and are briefly discussed to study the power quality problems.

4.2.1 Ripple factor

The ratio of an absolute value of an AC component to the DC component in the rectifier output is called a ripple factor or correction factor. It is essential to study the ripple factor to determine the efficiency of the rectifier. The smaller the ripple factor, the more efficient the rectifier, due to variations in the output voltage caused by ripples, it can also cause heating in a DC circuit component.

The ripple factor can be written as follows [93]:

$$\gamma = \frac{V_{rms}}{V_{dc}} = \frac{I_{rms}}{I_{dc}} \tag{4.3}$$

The ripple should be equal to zero for an ideal rectifier.

4.2.2 Form factor

The form factor is the ratio of the absolute value of a rms value to the average value of an alternating quantity [94].

The form factor:

$$FF = \frac{V_{rms}}{V_{av}} = \frac{I_{rms}}{I_{av}} \tag{4.4}$$

$$V_{av} = \frac{2 \times V_m}{\pi} \tag{4.5}$$

For an ideal waveform (with no harmonics), the form factor should equal to 1.11; form factor is used to determine the smoothness of waveform towards DC.

4.2.3 Peak factor

The peak factor is defined as the absolute value of a ratio of the maximum amount to the rms amount of an alternating magnitude [93, 94], and it is used for designing the cable insulation.

The peak factor:

$$PF = \frac{V_m}{V_{rms}} = \frac{I_m}{I_{rms}} \tag{4.6}$$

4.2.4 Total harmonic distortion (THD)

The THD is a measure of the distortion due to the harmonic content of the supply AC components (current or voltage) and can be formulated as follows:

$$THD = \sqrt{((I_{rms}^2 - I_{s1}^2)/I_{s1})} \tag{4.7}$$

where I_{s1} is a fundamental component of AC current, I_{rms} is the rms magnitude of the distorted current wave.

The THD can also be formulated as the summation of all harmonic components of the voltage or current waveform divided by the fundamental component as follows:

$$THD = \frac{\sqrt{(V_2^2 + V_3^3 + V_4^2 + \cdots + V_n^2)}}{V_1} \times 100\% \tag{4.8}$$

The THD should equal to zero for an ideal rectifier.

The displacement power factor (DPF) can be formulated as the cosine of the angle between the fundamental components of the input voltage and current, which is called the displacement angle, and could be given as follows:

$$DPF = cos\, \emptyset_1 \tag{4.9}$$

The DPF should be equal to 1, for an ideal rectifier.

The distortion factor is defined as the distortion of a waveform compared to the sinusoidal waveform. It is also defined as the ratio of the rms magnitude of the fundamental component (I_{s1}) against the rms magnitude of the distorted current waveform (I_s) [93, 94].

$$Distortion\ factor = \frac{I_{s1}}{I_s} \tag{4.10}$$

4.3 SWITCHING LOSSES

This is a loss of power that occurs instantaneously during ON-OFF transitions of a semi-conductor switch. Although the ON-OFF transition is a few nanoseconds, power loss may be a considerable amount. Figure 4.1 is a DC-DC boost converter that represents the switching losses equations.

Based on Figure 4.1,

$$i_a(t) + i_b(t) = i_L(t) \tag{4.11}$$

The instantaneous power dissipated by the transistor can be given by (4.12):

$$v_a(t) \times i_a(t) \tag{4.12}$$

While the transistor is in OFF state, the energy loss is given by:

$$W_{OFF} = 0.5 \times V_g \times i_L \times \textit{turn OFF time} \tag{4.13}$$

When $v_a = V_g$, then the diode becomes forward biased; when the transistor is in ON state the energy loss can be given by:

$$W_{ON} = 0.5 \times V_g \times i_L \times \textit{turn ON time} \tag{4.14}$$

The total energy that can be wasted during switching period is $(W_{ON} + W_{OFF})$, and the total power which can be dissipated during the switching period can be given as:

$$P_{sw} = (W_{ON} + W_{OFF}) \times f_{sw} \tag{4.15}$$

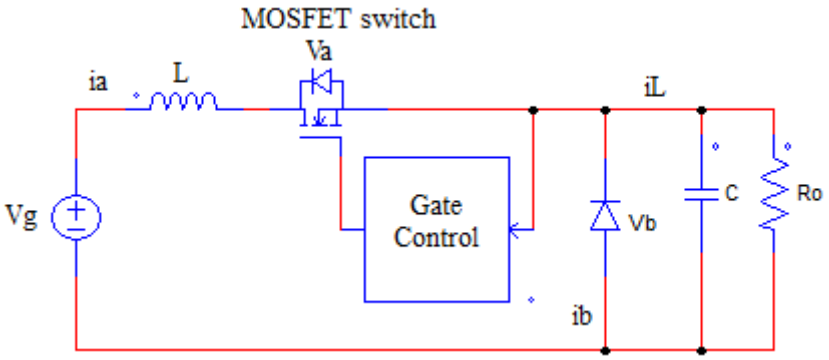

Figure 4.1. MOSFET switch representation [94]

4.3.1 Efficiency versus switching frequency

The electrical system efficiency (η) can be given by the following equation:

$$\eta = \frac{P_{out}}{P_{out}+P_{loss}} \tag{4.16}$$

Here, P_{out} is the converter output power, P_{loss} is power dissipated due to losses.

$$P_{loss} = P_{cond.} + P_{fixed} + P_{sw} \tag{4.17}$$

where, $P_{cond.}$ is conduction losses, P_{fixed} is fixed losses and P_{sw} is switching losses.

These equations can be applied to all electrical equipment.

$$P_{sw} \propto P_{loss}$$

$$P_{sw} = W_{total} \times f_{sw} \tag{4.18}$$

$$W_{total} = W_{ON} + W_{OFF} \tag{4.19}$$

$$P_{sw} \propto f_{sw}$$

The critical frequency can be given by:

$$f_{cri.} = \frac{P_{cond.}+P_{fixed.}}{W_{total}} \tag{4.20}$$

Switching losses cause efficiency to decrease at high frequencies, and the Vienna rectifier has a minimum number of switches compared with other types of active rectifiers.

4.4 CRITERIA FOR SELECTING POWER CONVERTER'S TOPOLOGIES

The selection of power converters for a WECU is based on capability to ensure zero THD, zero ripple factor, unity power factor, unity DPF and unity form factor based on (4.1) to (4.20). The control of those parameters requires controlling the AC-side voltage by maintaining the reactive power.

To control the active power, the voltage and current signals must be maintained, for example for angle control; the power has to be controlled using (3.3); which was defined previously and can be rewritten as:

$$P = \frac{3V_s V_c}{X_s} \sin \delta \tag{4.21}$$

Converters can attenuate the voltage and current ripple and harmonic distortion; the power converters in a WECS working at high switching frequency generate low current harmonic distortion. In this work, the WECS is integrated with Vienna active rectifier-I and MMC systems. Nevertheless, the power is not high compared with conventional converters. The generator's power output is typically controlled along with the variation of the converter duty cycle or delay angle [95].

4.5 THE VIENNA-I RECTIFIER STRUCTURE AND ANALYSIS

Vienna active rectifier-I [62], is one of several types of converters that can be selected as a MSC for WECS. The converter topology is shown in Figure 4.2. It contains three identical power electronic legs; each one is connected separately to a phase input. Each power cell includes one active switch (MOSFET or IGBT) and six diodes. The control of the three switches ensures sinusoidal waves input current and desired balanced output DC voltage.

There are three levels of the output voltage, $\boldsymbol{V_{C1}}$ and $\boldsymbol{V_{C2}}$; each is half of the thorough output voltage and the third level is the total ($\boldsymbol{V_{C1}} + \boldsymbol{V_{C2}}$) and should be higher than the maximum supply voltage because the converter is used here as a boost type. The output of all stages is connected to a middle joint with output capacitors; the midpoint of the capacitors is functionally clamped to a neutral power by connecting it to mid-points of one arm of the diode bridges of the three phases [96-100].

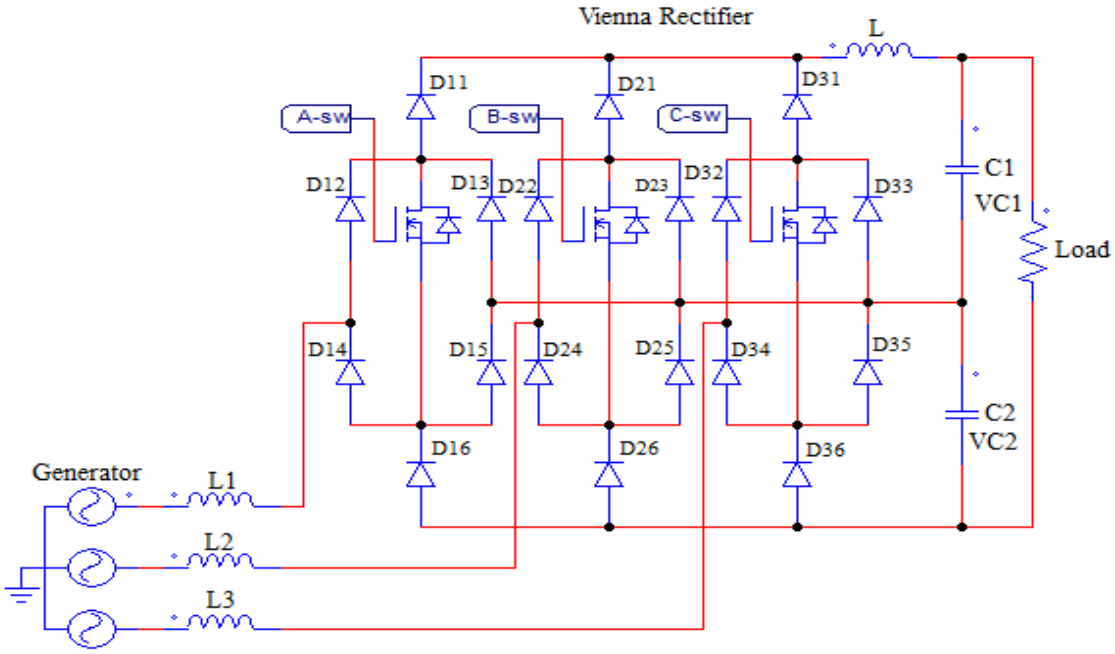

Figure 4.2. Three-phase Vienna active rectifier-I topology [12, 96]

The switching frequency is too high compared with the supply frequency. The output voltage of the considered rectifier does not affect the polarity of the AC input, as well as the switching states.

The Vienna rectifier-I is beneficial and cost-effective, and is conforms with the specifications of power quality and power flexibility applications. Also, it has a fewer number of active semiconductor devices and less voltage stress compared with conventional rectifiers because the output capacitor is separated into two sections with two equivalent values (C1, and C2) as shown in Figure 4.2, to ensure continuous conduction. It has low

current THD and high-power density, due to fewer numbers of active switches used, compared to conventional rectifiers. Therefore, it has been used in several high voltages and high-power applications. The operation details of the considered converter have been explained in [96-99].

The generator-side three-phase voltages can be presented as follows [97]:

$$\begin{aligned} e_a &= E\,sin(\omega_s\,t) \\ e_b &= E\,sin(\omega_s\,t - 120) \\ e_c &= E\,sin(\omega_s\,t + 120) \end{aligned} \tag{4.22}$$

where, e_a, e_b, and e_c are the three-phase generator instant voltages, E is the maximum generator output voltage, ω_s is the generator-angular velocity.

Equation (4.22) can be rewritten as shown in (4.23).

$$\begin{aligned} e_a &= Ri_a + L\frac{di_a}{dt} + v_{an} \\ e_b &= Ri_b + L\frac{di_b}{dt} + v_{bn} \\ e_c &= Ri_c + L\frac{di_c}{dt} + v_{cn} \end{aligned} \tag{4.23}$$

where, R is the internal generator resistance, L is the generator inductance, v_{an}, v_{bn}, and v_{cn} are the terminal voltages of the rectifier [12, 96-99].

4.5.1 Small-signal modelling of Vienna rectifier-I

The analysis of the system response to small disturbances is called small-signal modelling of the system.

The nonlinear state-space equation describing the system operation can be represented as follows:

$$\dot{x} = Ax + Bu \tag{4.24}$$

where *A* is the system matrix, *B* is the input matrix, *x* is the state vector, and *u* is the input vector.

By referring to Figure 4.2, applying Kirchhoff's rules to the converter's AC-side circuit yields the following equations that are principally time-variant concerning AC signs and switching states [101].

$$[v_d\ v_q\ v_0]^T = Z[v_a\ v_b\ v_c]^T \tag{4.25}$$

$$[i_d\ i_q\ i_0]^T = Z[i_a\ i_b\ i_c]^T \tag{4.26}$$

$$[d'_d\ d'_q\ d'_0]^T = Z[d'_1\ d'_2\ d'_3]^T \tag{4.27}$$

where *Z* is the abc/dq0 transformation matrix, v_o is the total DC output voltage, and can be depicted as:

$$v_o = v_{o,u} + v_{o,l} \tag{4.28}$$

$$\Delta v_o = v_{o,u} - v_{o,l} \tag{4.29}$$

where Δv_o is the variation between the two partial DC output buses which should be equal to zero, $\Delta V_o = 0$

$$\begin{bmatrix} V_d \\ V_q \\ V_{s0} \end{bmatrix} = \begin{bmatrix} \sqrt{2}\,V_s \\ 0 \\ 0 \end{bmatrix} \tag{4.30}$$

$$\begin{bmatrix} I_d \\ I_q \\ I_0 \end{bmatrix} = \begin{bmatrix} \sqrt{2}\,I_s^* \\ 0 \\ 0 \end{bmatrix} \tag{4.31}$$

where V_s is the supply rms voltage, I_s and V_o are the reference values of the generator output current and a total DC output voltage.

$$V_{o,u} = V_{o,l} = \frac{V_o}{2} \tag{4.32}$$

With reference to the state-space equation shown in (4.24), where the state vector, $x = [i_d\ i_q\ v_o\ \Delta v_o]^T$, and the input vector, $u = [v_d\ v_q\ ]^T$

The state matrix, $A = \begin{bmatrix} G_{id11}(s) & G_{id12}(s) & G_{id13}(s) \\ G_{id21}(s) & G_{id22}(s) & G_{id23}(s) \\ G_{vd11}(s) & G_{vd12}(s) & G_{vd13}(s) \\ G_{\Delta vd11}(s) & G_{\Delta vd12}(s) & G_{\Delta vd13}(s) \end{bmatrix}$

The input matrix $B = \begin{bmatrix} G_{iv11}(s) & G_{iv12}(s) \\ G_{iv21}(s) & G_{iv22}(s) \\ G_{vv11}(s) & G_{vv12}(s) \\ G_{\Delta vv11}(s) & G_{\Delta vv12}(s) \end{bmatrix}$

$$\frac{d}{dt}\begin{bmatrix} i_d \\ i_q \\ v_o \\ \Delta v_o \end{bmatrix} = \begin{bmatrix} G_{id11}(s) & G_{id12}(s) & G_{id13}(s) \\ G_{id21}(s) & G_{id22}(s) & G_{id23}(s) \\ G_{vd11}(s) & G_{vd12}(s) & G_{vd13}(s) \\ G_{\Delta vd11}(s) & G_{\Delta vd12}(s) & G_{\Delta vd13}(s) \end{bmatrix}\begin{bmatrix} i_d \\ i_q \\ v_o \\ \Delta v_o \end{bmatrix} + \begin{bmatrix} G_{iv11}(s) & G_{iv12}(s) \\ G_{iv21}(s) & G_{iv22}(s) \\ G_{vv11}(s) & G_{vv12}(s) \\ G_{\Delta vv11}(s) & G_{\Delta vv12}(s) \end{bmatrix}\begin{bmatrix} v_d \\ v_q \end{bmatrix} \quad (4.33)$$

where the symbol is in the form $G_{ab\beta\gamma}$, such as a is output, i.e. an element of the vector x, b is input, i.e. an element of a vector u, β is rank of the output a in the vector x, and γ is the rank of the input b in the vector u [101].

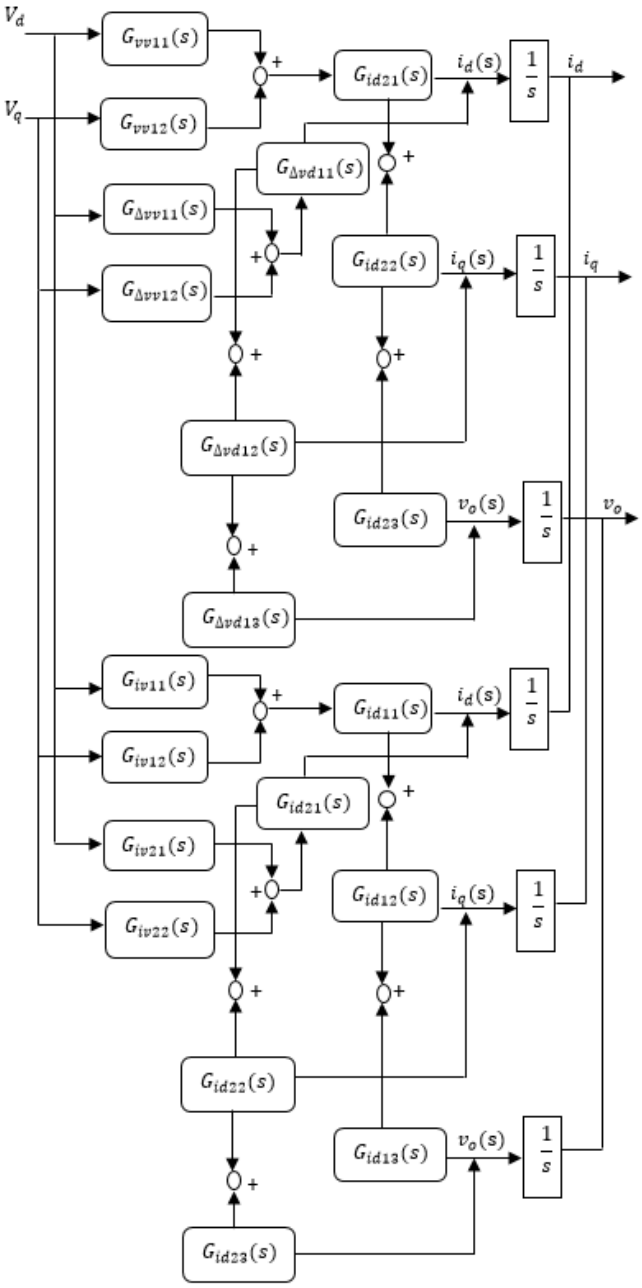

Figure 4.3. Transfer-function block diagram of the rectifier in the small-signal procedure

The list of transfer functions $G_{ab\beta\gamma}$, their parameters and the block diagram that represents the summarized model is given in Addendum A. The equivalent transfer function that represents the Vienna-I rectifier is given by taking Laplace transform for (4.33), which is represented in Figure 4.3.

4.6 MMC STRUCTURE AND ANALYSIS

The MMC initially introduced in 2003 [102] offers several advantages compared with other converters, such as low harmonic output signals, lower losses, efficient and modular output voltage waveforms, and it is ideal for high power applications. The demerit of this topology is that the stability and control structure is complicated [102]. The topology of MMC is presented in Figure 2.7 and is repeated in Figure 4.4 (a) [102-105].

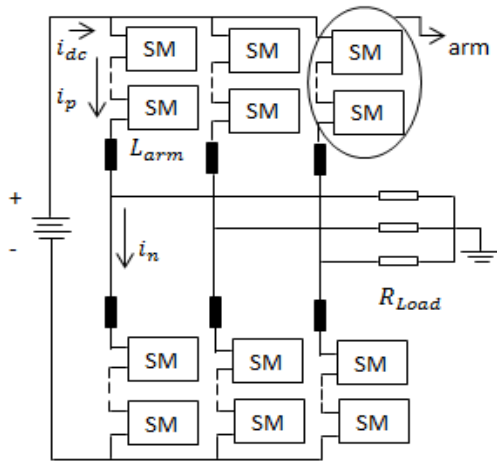

(a)

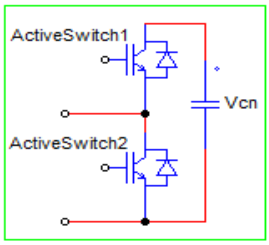

(b)

Figure 4.4. (a) MMC topology (b) Structure of half-bridge sub-module

It consists of three-phases, each with upper and lower arms, and the arm consists of N series-connected sub-modules and a series inductor L_{arm} to control the circulating current and to limit the fault current. The voltage levels of the MMC converter are defined by the number of sub-modules that are included in the upper and lower arms, as depicted in Figure 4.4 (b). It is a half-bridge circuit consisting of two active switches and capacitor connected in parallel.

The advantage of this topology compared to other MMC topologies is that only two switches are used, which results in minimization of the number of components and increase in MMC efficiency. The demerit of this topology is difficulty to control DC-side faults when used as a rectifier [106].

4.6.1 Operation principles of the MMC

The half-bridge sub-module shown in Figure 4.4 (b), consists of two IGBT switches and a capacitor. In steady-state operation, only one of the switches is turned on at any instant of time. The charging and discharging of the capacitor are dependent on the current direction. A half-bridge cell is a DC chopper topology where the output voltage is depending on the switching states, thus is either equal to zero or equal to the capacitor voltage. The output voltage of a topology and the switching states are clarified in Table 4.1. When either of the switches is turned on, the other one of the same topologies should be switched OFF to avoid short-circuiting. There are three switching states, i.e.:

- ON state or insert mode, in this case, active switch 1 is ON, and active switch 2 is OFF. The output voltage V_{SM} equals the capacitor voltage V_C, and the capacitor can charge and discharge in this interval.
- OFF state or bypass mode, in this case, the active switch 2 is ON, and the active switch 1 is OFF. The output voltage V_{SM} is zero, and the capacitor will not charge or discharge.
- Blocked state, in this case, both switches are OFF, and the current can conduct only through the freewheeling diodes. The capacitor will charge if the current is positive [106].

Table 4.1 Switching states of a half-bridge MMC

Switching state	S_1	S_2	V_{out}
ON state	ON	OFF	V_C
OFF state	OFF	ON	0
Blocked state	OFF	OFF	0

The following equations give the AC reference phase voltage and current:

$$v_{ac}^{*} = V_{ac}\, sin(\omega_0\, t) \tag{4.34}$$

$$i_{ac}^{*} = I_{ac}\, sin(\omega_0 t + \theta) \tag{4.35}$$

4.6.2 Modulation and modelling of MMC

4.6.2.1 Modulation techniques

The sinusoidal PWM and space vector PWM techniques are the most commonly used for implementing the PWM strategy for multilevel inverters. The space vector PWM is seen as a better technique of PWM implementation compared to sinusoidal PWM due to proper utilization of DC-bus voltage, low current ripple, lower switching frequency, less THD, simplicity, easy and direct implementation in a digital signal processor, and can be efficiently and effectively accomplished in a few microseconds [106-108].

4.6.2.2 Equivalent circuit model

The equivalent representation of a three-phase MMC is depicted in Figure 4.5. The sub-module in each arm is simulated as a single equivalent DC voltage source. This model is simple and easy to analyze and simulate [106, 107]. It can also be employed to control various current components circulating through the arm and to show the decoupled current models [106].

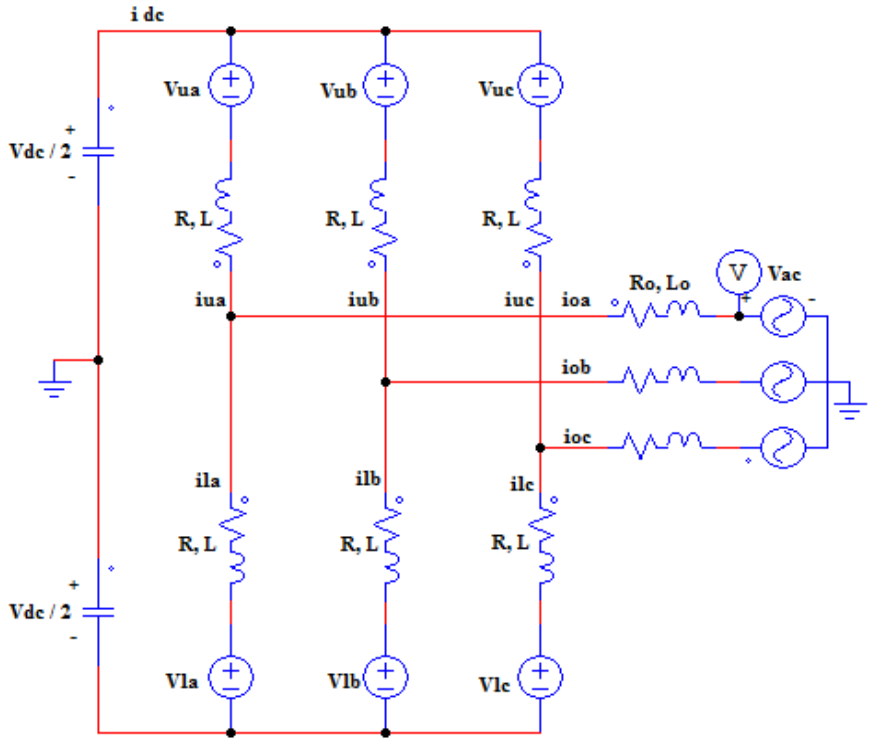

Figure 4.5. Equivalent circuit model of an ideal arm three-phase MMC

This simplified model is convenient when the sub-module capacitance is large enough to model as a constant DC voltage source. Increasing the sub-modules of MMC can contribute in decreasing the harmonic components of the voltage sources.

4.6.2.3 Mathematical modelling

The interaction between the variable line quantities and the arm generates low and high-frequency components in the DC and AC parts of the MMC. The operation and behavior of the MMC during the steady-state condition is complicated. Simulations are utilized to investigate the behavior of the converter. A control platform is required to handle the control objectives of the converter. However, the simulation process and the controller design are challenging work due to much time that can be expended for several sub-modules per arm. Several equivalent mathematical models is proposed in the literature to address the problems mentioned above [106-108].

From Figure 4.5, the upper (positive) and lower (negative) arm currents of phase *k*, *k* = *a*, *b*, *c* can be explained by the following equations [107]:

$$i_{u,k} = \frac{i_{DC}}{3} + i_{circ,k} + \frac{i_k}{2} \tag{4.36}$$

$$i_{l,k} = \frac{i_{DC}}{3} + i_{circ,k} - \frac{i_k}{2} \tag{4.37}$$

where i_{DC} is the DC-link current, $i_{circ,k}$ is the circulating current within phase *k*, i_k is the AC side phase currents.

The circulating current based on (4.36) and (4.37) can be given by (4.38):

$$i_{circ,k} = \frac{i_{u,k}+i_{l,k}}{2} - \frac{i_{DC}}{3} \tag{4.38}$$

The mathematical equations that adjust the functional behavior of the MMC phase-*k* are shown as follows [108]:

$$\frac{V_{DC}}{2} - v_{u,k} = L_{arm}\frac{di_{u,k}}{dt} + R_{arm}i_{u,k} + v_k + V_{ac} \tag{4.39}$$

$$\frac{V_{DC}}{2} - v_{l,k} = L_{arm}\frac{di_{l,k}}{dt} + R_{arm}i_{l,k} - v_k - V_{ac} \tag{4.40}$$

where V_{DC} is the DC-link voltage, $v_{u,k}$, and $v_{l,k}$ represent the upper and lower arm voltages of the MMC phase-*k*, respectively, L_{arm} is the arm inductor, R_{arm} is arm resistor, v_k and v_{ac} are voltage loss and AC output voltage, respectively.

The AC voltage of MMC can be obtained as follows [108]:

$$V_{ac} = \frac{v_{l,k}-v_{u,k}}{2} - \frac{R_{arm}}{2}i_k - \frac{L_{arm}}{2}\frac{di_k}{dt} - v_k \tag{4.41}$$

The circulating current of the MMC is obtained by the following equation:

$$L_{arm}\frac{di_{circ,k}}{dt} + R_{arm}i_{circ,k} = \frac{V_{DC}}{2} - \frac{v_{u,k}+v_{l,k}}{2} - R_{arm}\frac{i_{DC}}{3} \tag{4.42}$$

The following equations explain the upper and lower arm voltages of the MMC phase-k:

$$v_{u,k} = n_{u,k} v_{su,k} \tag{4.43}$$

$$v_{l,k} = n_{l,k} v_{sl,k} \tag{4.44}$$

where $n_{u,k}$ and $n_{l,k}$ are the number of sub-modules per upper and lower arm per phase-*k*. $v_{su,k}$ and $v_{sl,k}$ is the capacitor voltages of individual sub-modules of the upper and lower arms.

By substitute $v_{u,k}$ and $v_{l,k}$ from (4.43), and (4.44) in (4.41), and (4.42), the output voltage can be obtained as follows:

$$v_k + V_{ac} = \frac{n_{l,k} v_{sl,k} - n_{u,k} v_{su,k}}{2} - \frac{L_{arm}}{2} \frac{di_k}{dt} - \frac{R_{arm}}{2} i_k \tag{4.45}$$

$$L_{arm} \frac{di_{circ,k}}{dt} + R_{arm}\, i_{circ,k} = \frac{V_{DC}}{2} - R_{arm} \frac{i_{DC}}{3} - \frac{n_{l,k} v_{sl,k} + n_{u,k} v_{su,k}}{2} \tag{4.46}$$

4.7 MMC CONTROL

4.7.1 Circulating current control

Circulating currents flowing via the MMC arms are sinusoidal but at twice the output frequency. These currents are caused by the inner voltage differences among the three-phase arms and contain negative sequences. There is no adverse influence on the AC-side voltages and currents due to circulating currents. Despite that, if not controlled properly, they will boost the peak and rms magnitudes of the phase-arm currents, which can then raise the ripple value of the capacitor voltages, as well as converter power losses [106, 107]. However, the challenge to control the circulating current is accurate sizing of the arm inductor.

The inner three-phase electromotive force (EMF) required voltage (e_k) is controlled as a sinusoidal waveform as follows [107]:

$$e_k(t) = E_k \sin \omega_0 t = \frac{V_{DC}}{2} \times z \times \sin \omega_0 t \tag{4.47}$$

where E_k represents the peak magnitude of the inner EMF, ω_0 is the radian frequency, and *z* is constant and represents the amplitude modulation index, and can be expressed as follows:

$$z = \frac{E_k}{v_{dc}/_2} \tag{4.48}$$

By considering (4.48), the upper and lower arm voltages are obtained as follows [108]:

$$V_{uk}(t) = \frac{1}{2}V_{DC} - e_k(t) = \frac{1}{2}V_{DC}[1 - z.sin(\omega_0 t)] \tag{4.49}$$

$$V_{lk}(t) = \frac{1}{2}V_{DC}[1 + z.sin(\omega_0 t)] \tag{4.50}$$

Due to dual fundamental-frequency, the upper and lower arm voltages can be expressed as follows [107]:

$$V_{uk}(t) = \frac{1}{2}V_{DC}[1 - z.sin(\omega_0 t)] + \frac{V_{2f}}{2}sin(2\omega_0 t + \varphi) \tag{4.51}$$

where V_{2f} is the voltage value at the double fundamental frequency.

$$V_{lk}(t) = \frac{1}{2}V_{DC}[1 + z.sin(\omega_0 t)] + \frac{V_{2f}}{2}sin(2\omega_0 t + \varphi) \tag{4.52}$$

The double fundamental-frequency voltage triggers the circulating current passing through two arm inductors, so the peak value of circulating current can be explained as follows [109]:

$$i_{2f}(t) = -\frac{V_{2f}}{4\omega_0 L_0}sin\left(2\omega_0 t + \varphi - \frac{\pi}{2}\right) = I_{2f}\,cos(2\omega_0 t + \varphi) \tag{4.53}$$

where $i_{2f}(t)$ represents the instant value of the circulating current, I_{2f} is the maximum value of the circulating current, and f is the fundamental frequency.

The equations that clarify the three-phase inner circulating currents can be depicted as follows [106]:

$$i_{circ,a} = \frac{i_{DC}}{3} + I_{2f}\,sin(2\omega_0 t + \varphi_0) \tag{4.54}$$

$$i_{circ,b} = \frac{i_{DC}}{3} + I_{2f}\,sin[2(\omega_0 t - \frac{2\pi}{3}) + \varphi_0] \tag{4.55}$$

$$i_{circ,c} = \frac{i_{DC}}{3} + I_{2f}\,sin[2(\omega_0 t + \frac{2\pi}{3}) + \varphi_0] \tag{4.56}$$

The frequency of the circulating current is double the fundamental frequency and the current is sinusoidal.

The relationship between the circulating current and voltage amplitudes can be obtained as follows [106]:

$$I_c = \frac{V_c}{\sqrt{R^2+(2\omega_0 L)^2}} \tag{4.57}$$

where I_c is the circulating current, V_c is the voltage amplitude.

The energy base for a converter arm is defined as follows [108]:

$$W_{base} = 0.5\, NC_{SM}\left({}^{X_{dc}V_{DC}}/_{N}\right)^2 = 0.5({}^{C_{SM}}/_{N})X_{dc}^2V_{DC}^2 \tag{4.58}$$

where C_{SM} is the sub-module capacitance, ${}^{X_{dc}V_{DC}}/_{N}$ is the average capacitor voltage.

To design an arm inductance for a given circulating current (4.59) can be used.

$$L_{arm} = \frac{1}{8\omega_0^2\times C_{SM}\times V_C}\left[\frac{P_s}{3\times I_{2f}} + V_{DC}\right] \tag{4.59}$$

4.7.2 Small-signal modelling of MMC

The small-signal modelling of the system is the analysis of the system response to small disturbances, which can be analysed from the regular state-space model to simplify the analysis and simulation models [109, 110],

$$\dot{x} = Ax + BU \tag{4.60}$$

where *A* is the system matrix, *B* is the input matrix, *x* is the state vector, and *u* is the input vector.

x and *u* can be presented in their steady-state and small-signal components as follows:

$$x = x^{-} + x_{\circ} \tag{4.61}$$

$$u = u^{-} + u_{\circ} \tag{4.62}$$

Substituting (4.61) and (4.62) into (4.60) yields:

$$\dot{x^-} + \dot{x_\circ} = Ax^- + Ax_\circ + Bu^- + Bu_\circ \tag{4.63}$$

Equation (4.63) can be separated as:

$$\dot{x^-} = Ax^- + Bu^- \tag{4.64}$$

$$\dot{x_\circ} = Ax_\circ + Bu_\circ \tag{4.65}$$

Equations (4.64) and (4.65) identify the small-signal model and steady-state model, respectively.

The following dynamic equation describes the MMC model [110]:

$$\frac{d}{dt}\begin{bmatrix} i_{circ} \\ \sum V_{Cu} \\ \sum V_{Cl} \end{bmatrix} = \begin{bmatrix} -\frac{R_{arm}}{L_{arm}} & \frac{m_u}{2L_{arm}} & \frac{m_l}{2L_{arm}} \\ \frac{-m_u}{C_{arm}} & 0 & 0 \\ \frac{-m_l}{C_{arm}} & 0 & 0 \end{bmatrix}\begin{bmatrix} i_{circ} \\ \sum V_{Cu} \\ \sum V_{Cl} \end{bmatrix} + \begin{bmatrix} \frac{-V_{DC}}{2L_{arm}} \\ \frac{-m_u i_{conv.}}{2C_{arm}} \\ \frac{m_l\, i_{conv.}}{2C_{arm}} \end{bmatrix} \tag{4.66}$$

where C is the capacitance of one sub-module, $C_{arm} = {}^{C}/_{N}$, i_{circ} is the circulating current, V_{Cu} and V_{Cl} are the upper (positive) and lower (negative) pole voltages respectively, $\sum V_{Cu}$ and $\sum V_{Cl}$ are the sums of the maximum voltage of upper and lower arms respectively, i_{conv} and i_{ac} are the same; but if the load is AC at the load side it is named i_{ac} and the current flowing through the inverter is called i_{conv}, and is equal to $(i_{u,k} + i_{l,k})$, V_{DC} is the DC-bus voltage, m_u and m_l are modulation indices of the corresponding arms.

The control modulation signals m_u and m_l can be presented as follows [110]:

$$m_u = 0.5(1 - M\,cos(\omega t - \theta_m) - M_2\,cos(2\omega t - \theta_{m2})) = (0.5)_0 - \left(\frac{M_d}{2}\right)_d cos(\omega t) - \left(\frac{M_q}{2}\right)_q sin(\omega t) - \left(\frac{M_{d2}}{2}\right)_{d2} cos(2\omega t) - \left(\frac{M_{q2}}{2}\right)_{q2} sin(2\omega t) \tag{4.67}$$

$$m_l = 0.5(1 + M\,cos(\omega t - \theta_m) - M_2\,cos(2\omega t - \theta_{m2})) = (0.5)_0 + \left(\frac{M_d}{2}\right)_d cos(\omega t) + \left(\frac{M_q}{2}\right)_q sin(\omega t) - \left(\frac{M_{d2}}{2}\right)_{d2} cos(2\omega t) - \left(\frac{M_{q2}}{2}\right)_{q2} sin(2\omega t) \tag{4.68}$$

where subscripts d, q indicate the two components in the coordinate frame rotating at the fundamental frequency $\omega_0 = 2\pi f$, while subscripts d_2, q_2 indicate the two components in the coordinate frame rotating at second harmonic $2\omega_0$, and subscript 0 denotes the zero-sequence. Components, M and M_2 are the modulation indices, M_d and M_q are the fundamental sine signals, M_{d2} and M_{q2} are the second harmonic sine signals.

The transfer function that represents the MMC model, when taking Laplace transform from (4.66) can be expressed in Figure 4.6.

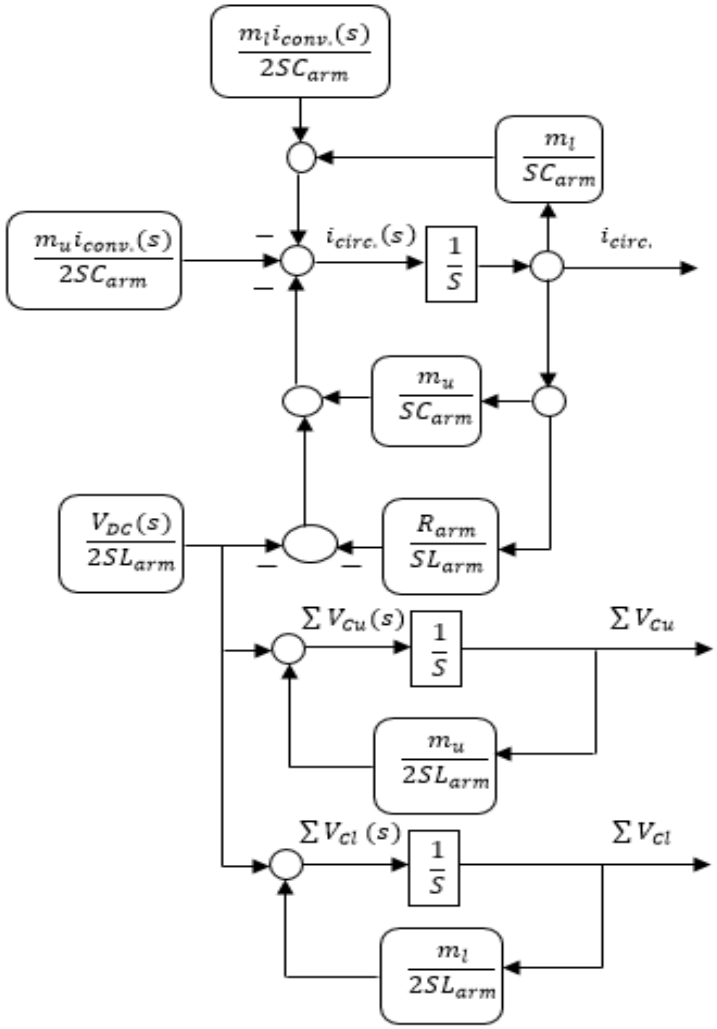

Figure 4.6. MMC state-space transfer function

4.8 CHAPTER SUMMARY

This chapter investigated the feasibility of integrating a three-phase active rectifier in a WECU. The analysis includes factors that affect the performance and criteria for selecting power converters. The small-signal modelling of the converters used for this work were discussed to analyze the system response to small disturbances. The system response at steady-state operation is investigated in Chapter 5.

In Section 4.2, presents the performance analysis of AC-DC converters. The factors that caused power losses and affected the system efficiency were discussed, thus enhancing the system efficiency by improving the power quality of the system. The ripple and the THD are discussed in the analysis, and all these factors are considered in a simulation process. In Section 4.3, the switching losses and efficiency versus switching frequency analysis equations were discussed.

The performance analysis of an AC to DC converter is discussed to determine the criteria for selecting power converters' topologies which are introduced in Section 4.4. Section 4.5 presents the Vienna rectifier-I structure and analysis. The performance, construction and small-signal modelling of three-phase Vienna rectifier-I is analyzed and discussed. The MMC structure and analysis is shown in Section 4.6. The performance, construction, small-signal modeling of three-phase MMC is analyzed and discussed.

CHAPTER 5 DC-VOLTAGE CONTROLLER DESIGN

5.1 CHAPTER OVERVIEW

Section 5.2 discusses the design of a DC-voltage controller. The aim of controlling the DC-bus voltage is to regulate the voltage and current across the DC-bus during steady-state operation by ensuring that no ripple waves move to the generator-side. The governor of the control circuit is an output voltage and sinusoidal supply input current. The output voltage is sensed and subtracted from the reference voltage to produce the error signal. It is desirable to minimise the error signal, and the current reference is used to maintain the sinusoidal supply current. The summary of the chapter is presented in Section 5.3.

5.2 DC-VOLTAGE CONTROLLER DESIGN

Current and voltage loop controllers are essential in modern applications in power electronics, such as micro-grids, variable speed drives, and active power filters [111-115] to maintain a stable voltage in a steady-state operation.

5.2.1 Current-loop controller design and analysis

The voltage and current loops are cascaded and adjusted using serial adjusting. The bandwidth of the current loop is fixed to the highest magnitude allowed by the system stability, to (i) raise the functional performances (ii) reduce the interactions with the voltage loop (iii) reduce the steady-state quantity and phase error; desirable zero error magnitude (iv) limit the peak current to avoid overload conditions (v) track the required reference

current during transient changes (vi) minimize low order harmonics of the load current, and (vii) decrease the DC-link voltage ripple. Figure 5.1 shows the schematic representation of the voltage and current control in a dq-frame. The topology shows the three-phase generator integrated with Vienna rectifier-I; the internal inductors and resistors for the rectifier are shown for analysis purposes. The terminal voltage becomes larger (smaller) than its steady-state value if the output power starts to increase (decrease) depending on the value of L and the rise time of the output power [116-119].

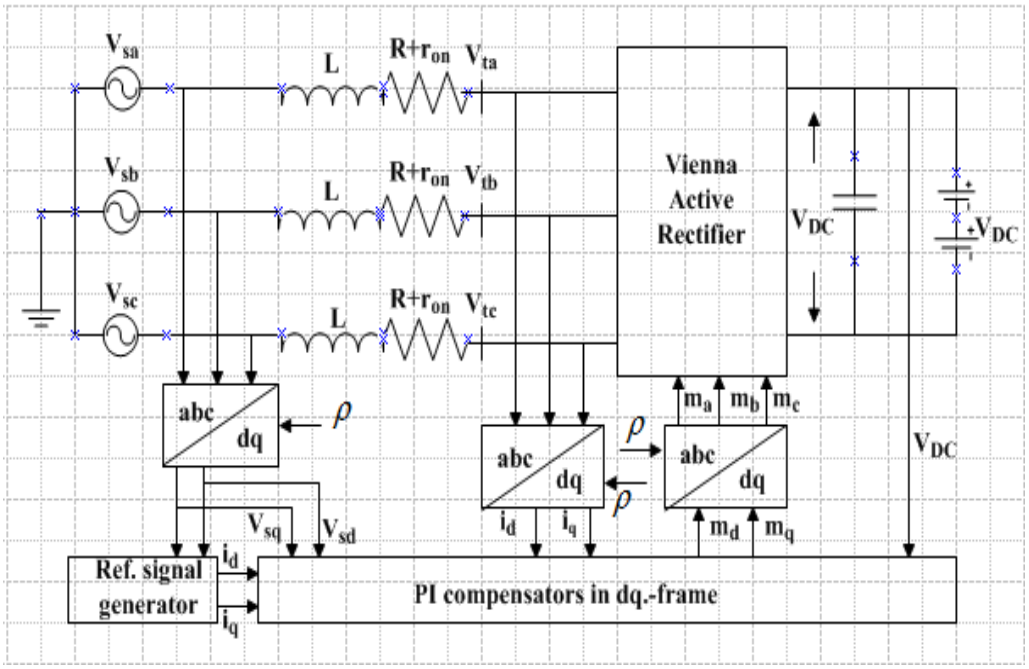

Figure 5.1. Graphical representation of the current-control in a dq-frame [111]

The AC voltages in a rectifier system shown in Figure 5.1 are presented as follows [111-114]:

$$V_{sa}(t) = \hat{V}_s cos(\omega_0 t + \theta_0)$$
$$V_{sb}(t) = \hat{V}_s cos(\omega_0 t + \theta_0 - \frac{2\pi}{3}) \quad (5.1)$$
$$V_{sc}(t) = \hat{V}_s cos(\omega_0 t + \theta_0 - \frac{4\pi}{3})$$

where $\hat{V}_s$ is a peak value of phase voltage, ω_0 is the AC source frequency, and θ_0 is the initial rotor angle.

The nonlinear system in Figure 5.1 can be described by the following equations:

$$L\frac{di_d}{dt} = V_{td} + L\omega(t)i_q - \hat{V}_s\, cos(\omega_0 t + \theta_0 - \rho) - (R + r_{on})i_d \qquad (5.2)$$

$$L\frac{di_q}{dt} = V_{tq} - L\omega(t)i_d - \hat{V}_s\, sin(\omega_0 t + \theta_0 - \rho) - (R + r_{on})i_q \qquad (5.3)$$

where i_d, i_q and ρ are the state variables, V_{td}, V_{tq} and ω are the control inputs.

Assuming steady-state operating conditions and substitute for $\omega(t) = \omega_0$, then, (5.2) and (5.3) will be written as follows:

$$L\frac{di_d}{dt} = V_{td} + L\omega_0 i_q - (R + r_{on})i_d - V_{sd} \qquad (5.4)$$

$$L\frac{di_q}{dt} = V_{tq} - L\omega_0 i_d - (R + r_{on})i_q - V_{sq} \qquad (5.5)$$

where V_{sd} and V_{sq} are disturbance inputs.

The relationship between the modulating signal and a corresponding AC-side terminal voltage can be given by the following equations:

$$\vec{V}_t(t) = \frac{V_{DC}}{2}\vec{m}(t) \qquad (5.6)$$

$$V_{td}(t) = \frac{V_{DC}}{2}m_d(t) \qquad (5.7)$$

$$V_{tq}(t) = \frac{V_{DC}}{2}m_q(t) \qquad (5.8)$$

$$m_d = \frac{2}{V_{DC}}(V_{sd} + U_d - L\omega_0 i_q) \qquad (5.9)$$

$$m_q = \frac{2}{V_{DC}}(V_{sq} + U_q + L\omega_0 i_d) \qquad (5.10)$$

where U_d and U_q are control inputs.

Substituting the m_d and m_q from (5.9) and (5.10) in (5.7) and (5.8), yields:

$$V_{td}(t) = (V_{sd} + U_d - L\omega_0 i_q) \qquad (5.11)$$

$$V_{tq}(t) = (V_{sq} + U_q - L\omega_0 i_d) \qquad (5.12)$$

Also substituting $V_{td}(t)$ and $V_{tq}(t)$ from (5.11) and (5.12), in (5.4) and (5.5), yields:

$$L\frac{di_d}{dt} = U_d - (R + r_{on})i_d \tag{5.13}$$

$$L\frac{di_q}{dt} = U_q - (R + r_{on})i_q \tag{5.14}$$

Then, (5.13) and (5.14) depict two separate first-order linear systems; i_d and i_q can be controlled by U_d, and U_q, respectively, as shown in Figure 5.2 (a) and (b).

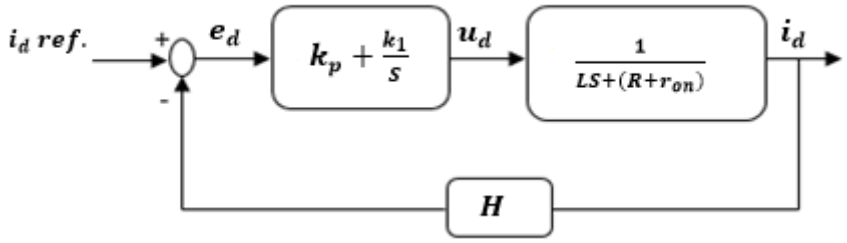

(a)

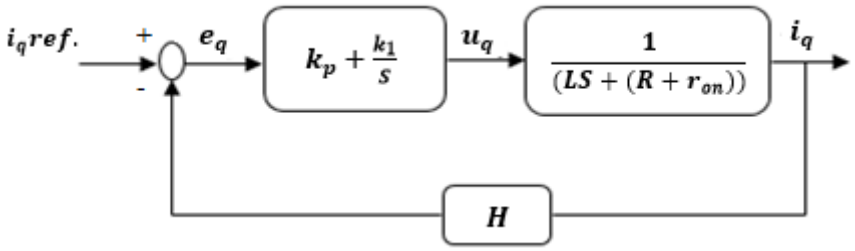

(b)

Figure 5.2. Closed-loop current controller (a) d- axis controller (b) q- axis controller [111]

The voltage loop controls the converter output voltage by fixing the current reference, and the current loop controls the converter to track the command, and this causes the current loop to be faster in response than the voltage loop [115].

The output signals (i_d and i_q) are sensed by the gain sensor H and transformed back and subtracted from the input current reference value. The control block diagram of the closed-loop system is shown in Figure 5.3., where G_v(s) and G_i(s), are the voltage and current compensators, respectively. V_{dq}^*, and i_{dq}^* are the reference voltage and current vectors.

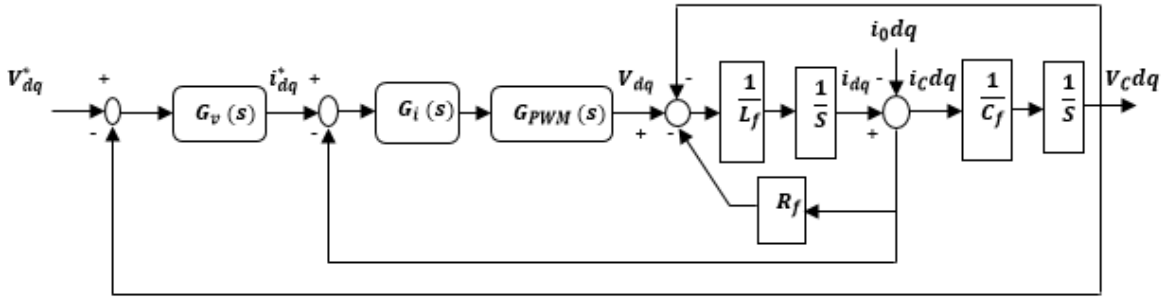

Figure 5.3. Block diagram of the closed-loop PWM controller [111, 119]

L_f is the filter inductor, R_f is the equivalent series resistance of the inductor, C_f is a filter capacitor value. Gpwm (s) is a transfer function related to PWM delays, $Gpwm\,(s) = [1-(Td/2)]/[1+(Td/2)]$, where T is the time delay of the system, and $= 1.5Ts = 375\ \mu s$.

The rate at which the electronic switch performs its function is called a switching frequency and is equal to $(1/T)$. The switching frequency directly affects the power dissipation in switching elements such as the diode, and transistors. These losses usually come from switching losses, resistance, inductor and capacitor losses. The design of the WECS must consider the various losses and reduce the efficiency associated with the high frequencies. A measure of the output power has to be included in the voltage regulation loop, as a feed-forward signal, to enhance the transient response (rise time, settling time, and overshoot) of the DC-bus voltage [116, 118].

The current compensator $G_i(s)$ that was designed and analyzed is proportional resonance (PR) compensator and can be given using (5.15):

$$G_i(s) = k_p + \frac{2\omega_{c1}k_iS}{S^2+2\omega_{c1}S+(h\omega_0)^2} \tag{5.15}$$

where, $k_p = 2\pi f_{bw}L$, and $k_i = \frac{R_f}{L_f}k_p$, f_{bw} is assumed to be 600 Hz; for the current control. This type of compensator has been selected due to its suitability for grid-connected converters' current control.

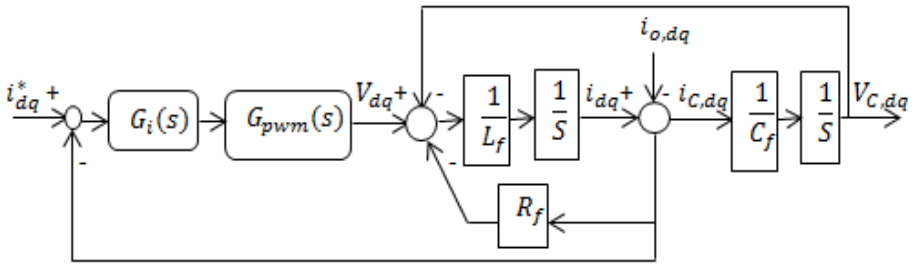

Figure 5.4. Block diagram of the designed current loop system [119]

It is demonstrated that the known drawbacks associated with proportional integral (PI) controllers like the need for decoupling for three-phase converters and the steady-state error for single-phase converters can be alleviated. The selective harmonic compensation is also possible with PR controllers.

The closed-loop control system must have high bandwidth compared to AC system frequency, to ensure adequate tracking performance and small steady-state errors. The bandwidth frequency of the closed-loop current control should be around ten times the system frequency. For most control structures, the bandwidth of the closed-loop voltage control is selected to be sufficiently lower than that of the current loop [111], where $\omega_0 = 2\pi \times 60 = 377$ rad/s is the fundamental resonant frequency, ω_{C1} is a damping frequency and assumed to be 10 rad/s.

The current closed-loop transfer function from Figure 5.4, can be determined in (5.16) as:

$$i_{dq}(s) = \frac{G_i(s)G_{pwm}(s)C_f(s)}{L_fC_fS^2+R_fC_fS+G_i(s)G_{pwm}(s)C_fS+1} i^*_{dq} + \frac{1}{L_fC_fS^2+R_fC_fS+G_i(s)G_{pwm}(s)C_fS+1} i_{0,dq} \quad (5.16)$$

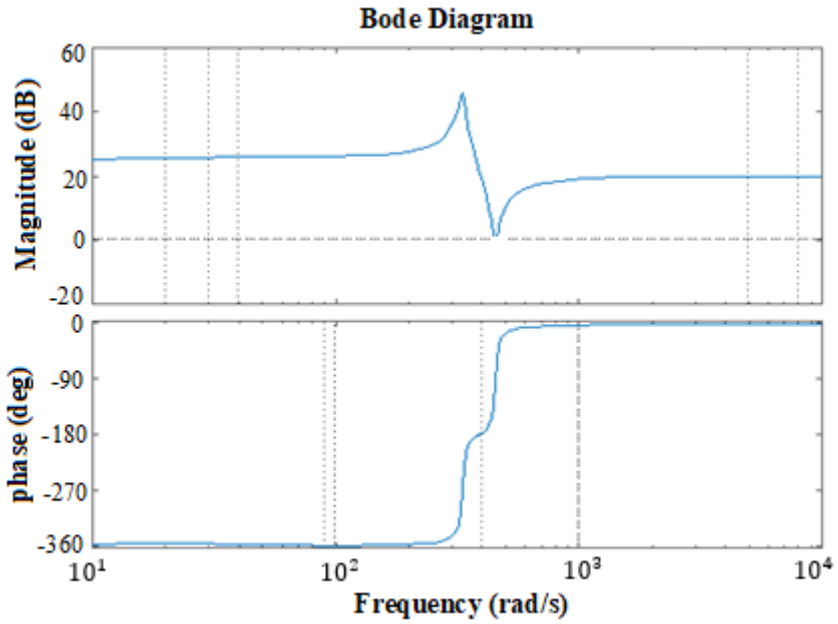

Figure 5.5. Closed-loop frequency response of the inner current loop

Figure 5.5 shows the frequency response of the transfer function in (5.16). The controller can produce zero steady-state error at the desired frequency (600 Hz).

5.2.2 Voltage loop control using phase-locked loop (PLL)

A PLL controller is a closed-loop feedback control system in which a generated signal is locked to a reference signal in phase and frequency [111, 115, 117]. The PLL control technique has been chosen for this work due to its advantages, such as demonstrating satisfactory behavior under certain conditions.

The AC voltages presented in (5.1) are rectifier input voltage equations, which can be rewritten in (5.17), and could be applied in Figure 5.6.

$$\begin{aligned} V_{sa}(t) &= \hat{V}_s \cos(\omega_0 t + \theta_0) \\ V_{sb}(t) &= \hat{V}_s \cos(\omega_0 t + \theta_0 - \tfrac{2\pi}{3}) \\ V_{sc}(t) &= \hat{V}_s \cos(\omega_0 t + \theta_0 - \tfrac{4\pi}{3}) \end{aligned} \tag{5.17}$$

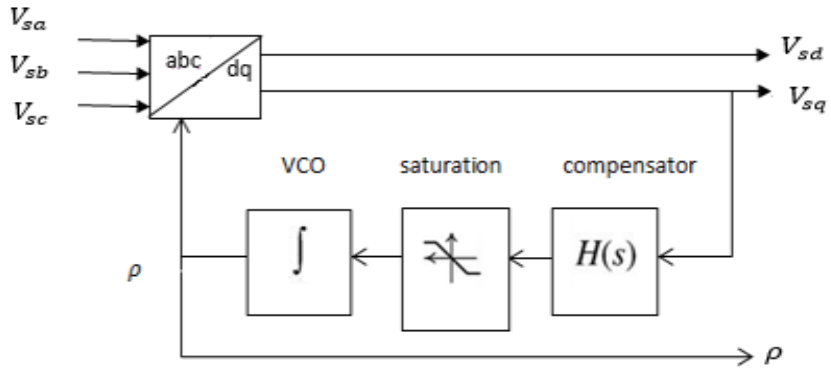

Figure 5.6. Graphical representation of the voltage control in a dq-frame [111, 115]

Based on the space phase:

$$f_d + jf_q = \vec{f}(t)e^{-j\rho(t)} \tag{5.18}$$

The voltage expressed in a dq-frame can be given by:

$$V_{sd} = \hat{V}_s \cos(\omega_0 t + \theta_0 - \rho) \tag{5.19}$$

$$V_{sq} = \hat{V}_s \sin(\omega_0 t + \theta_0 - \rho) \tag{5.20}$$

where ρ is the phase shift and,

$$\frac{\partial \rho}{\partial t} = \omega(t) \tag{5.21}$$

From (5.21), $\omega(t)$ is the input to the voltage-controlled oscillator (VCO) as shown in Figure (5.6), and it is integrated to produce the desired value of ρ.

The compensator output equation can be formulated as:

$$\omega(t) = H(p)V_{sq}(t) \tag{5.22}$$

where $H(p)$ is a compensator transfer function and p is a differentiation operator.

The PLL compensator H(s) in Figure 5.6, can be formulated as follows:

$$H(s) = \left(\frac{h}{\hat{V}_{sn}}\right) \times \frac{S^2 + (2\omega_0)^2}{S(S + 2\omega_0)^2} \times F(s) \tag{5.23}$$

where $\hat{V}_{sn}$ is the nominal value of $\hat{V}_s$, h is a constant gain, *F(s)* is a convenient transfer function with no zero at S = 0, and can be obtained using (5.24).

$$F(s) = \left(\frac{S+(p_1/\alpha)}{S+p_1}\right)^2 \tag{5.24}$$

where p_1 is the filter pole, α is a real constant and should be greater than 1.

The maximum phase margin of the filter is assumed to be 60° and can be given by (5.25) as follows:

$$\delta_m = sin^{-1}\left(\frac{\alpha-1}{\alpha+1}\right) \tag{5.25}$$

The maximum phase margin takes place at the frequency given as follows (5.26):

$$\omega_m = \frac{p_1}{\sqrt{\alpha}} \tag{5.26}$$

ω_m could be equal to the crossover frequency ω_c, which is assumed to be 250 rad/s.

The loop gain can be solved using (5.27)

$$l(s) = h \times \frac{S^2+(2\omega_0)^2}{S^2(s+2\omega_0)^2} \times F(s) \tag{5.27}$$

Assume $\boldsymbol{l(s) = 1}$, and substitute for h, then $\boldsymbol{h = 1.09 \times 10^6}$

Using parameters given in Table 5.1, the loop gain can be addressed and plotted to determine the frequency response. The bode plot in Figure 5.7, shows that L(s) declines with the slope of -20 dB when ω is greater than ω_C, the gain and phase margins are 75 dB and 60° respectively. A phase margin of 60° is an indication of a higher degree of stability because it allows for the fastest settling time.

Table 5.1 Parameters used for compensator design

Parameter	Description	Value
Phase margin	δ_m	60°
Crossover frequency	ω_c	250 rad/s
Supply frequency	$\omega = \omega_0$	377 rad/s
Peak value of phase voltage	$\hat{V}_s$	577 V

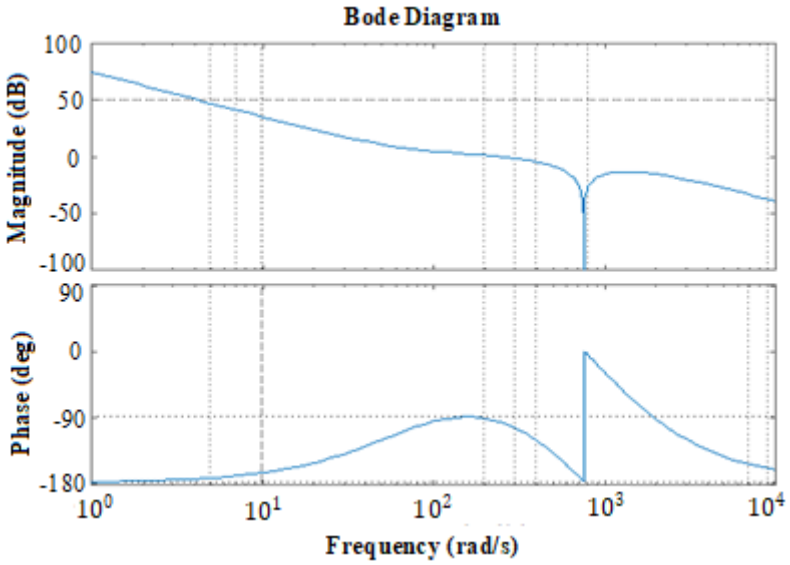

Figure 5.7. The frequency response of the PLL for the loop gain L(s)

5.3 CHAPTER SUMMARY

The DC voltage controller is a central part of the WECS which regulates the system voltage during steady-state operation. This chapter has presented a design of the closed-loop; inner current loop and outer voltage loop controllers in a dq-frame using PLL. In addition to an adequate DC voltage supply, it must also transfer the circuit connecting the sensor to the device receiving the output signal and then back to the transmitter, which is named a loop. The transmitter controls the current signal of the loop according to the sensor's measurement.

There are voltage and current loops; the higher the bandwidth, the faster the loop responds. The same data used for building the simulated system is used for designing the controller, and bode plot has demonstrated that the system is stable.

CHAPTER 6 SIMULATION RESULTS AND DISCUSSION

6.1 CHAPTER OVERVIEW

The significant contributions to this study are organized and discussed in this chapter. Simulations have been carried out using PSim software, and three virtual wind farms are simulated and discussed, for riding through AC and DC faults. The technical benefits of the proposed WECU models in a DC collection grid are discussed in terms of fluctuations and short-circuit rejection capability. The control strategies are derived and the system performance is investigated. Section 6.2 shows the virtual wind farm-I model analysis. The virtual wind farm-II model is analyzed in Section 6.3. Section 6.4 shows the analysis of the virtual wind farm III. The harmonic distortion and ripples occurring in the voltage/current signals are appropriately moderated.

This study has introduced the combination of three-phase active converters into the PMSG based WECU with a DC collection grid. The main objective of the investigation is to ride-through AC and DC faults to contribute to the reliability of WECSs. Most of the studies that have previously been done in this area applied the conventional three-phase full-bridge active rectifier in WECSs. There studies focused on modular converters, but there is no combination of Vienna-I rectifier and MMC in the literature. The summary of this chapter is outlined in Section 6.5.

The merits of this WECSs include low power loss, high efficiency, low number of controlled switches and low cost. The demerit of the system is complex control circuits. The DC voltage controller is designed to maintain the steady-state operation for a long time.

6.2 THE VIRTUAL WIND FARM I MODEL

6.2.1 System analysis

The WPP consists of three parallel-connected WECUs, as shown in Figure 6.1 (a). The fault is considered to be at the DC-link connected to unit 1, the DC fault that occurs close to unit 1 terminal will cause large fault currents in its proximity. This type of fault is due to the short circuit of a transmission line. The output current will be zero due to the flow of the fault current through the system.

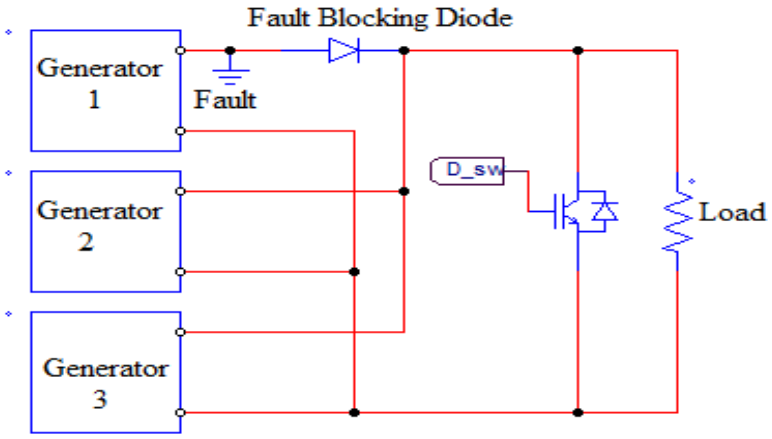

(a)

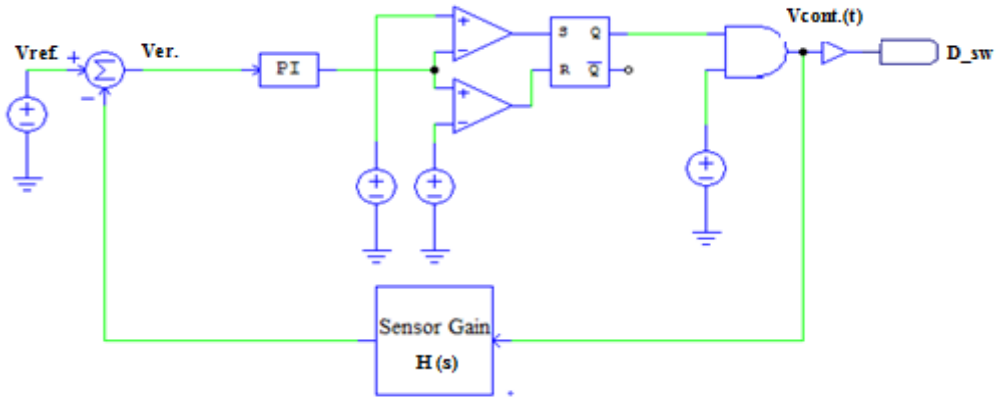

(b)

Figure 6.1. The simulated circuit (a) Three units connected in parallel (b) FRT controller

Figure 6.1 (b) shows the controller that has been used to ride through the fault through D_sw, and the fault blocking diode, which blocks the generator from feeding the DC-bus during the fault.

Table 6.1 Parameters used for simulations

Parameter	Description	Value
Generator voltage rating	V_g	400 V
Generator current rating	I_g	40 A
Turbine voltage rating	V_t	500 V
Turbine current rating	I_t	40 A
DC link capacitance	C_1, C_2	1000 μF
Load	R	50 Ω

The controller output voltage V_{cont} (t) is sensed with the gain sensor H (s), the sensor output will be H (s)×V_{cont} (s) and is compared with a reference input voltage $V_{ref.}$. The aim is to get H (s)×$V_{cont.}$ (s) closer to $V_{ref.}$. The variation between the reference input V_{ref} and the sensor output H (s)×V_{out} (s) is called an error signal. In an ideal system, the error signal is zero. Practically, the error signal should be a small value. In any case of disturbance, the compensator should compensate the error signal to the desired value.

Simulations have been done and the values of the parameters used are shown in Table 6.1. Three WECUs are linked in parallel; due to the reliability of the parallel connection, so if one unit collapses, the system remains in synchronism. Several modes of operation have been simulated and discussed as follows.

6.2.2 Steady-state mode of operation

In a steady-state operation condition, the switch will be locked for a long time, so that voltage and current waves are in stable operation. Figure 6.2 (a) and (b), shows the output voltage and current waveforms in the steady-state operation.

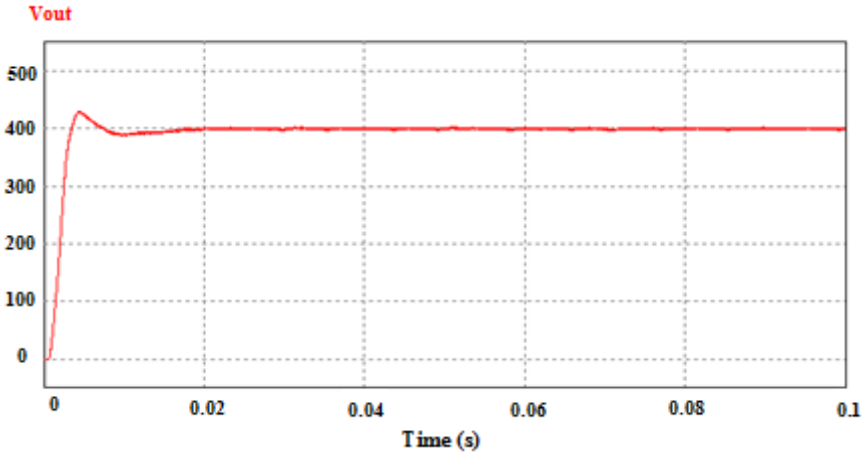

(a)

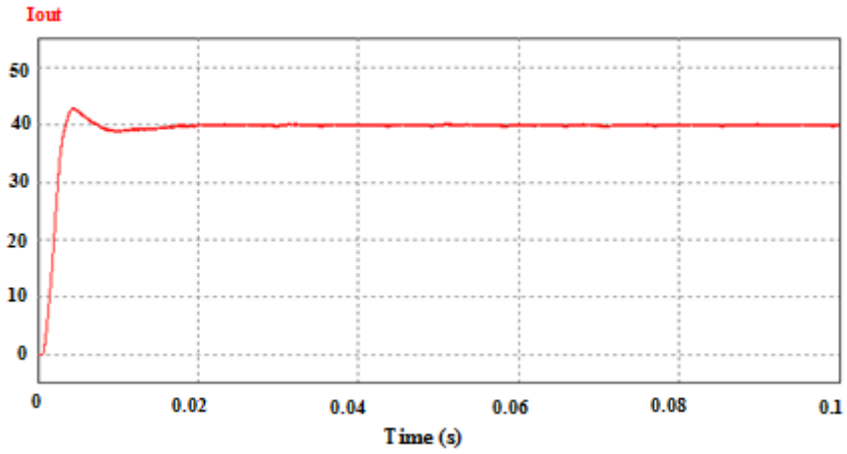

(b)

Figure 6.2. (a) Output voltage (b) Output current

The voltage output, as shown in Figure 6.2 (a) is in steady-state condition and is stable at 400 V after small overshooting (around 5 %) due to the system startup. Similar to the output voltage, the output current, as shown in Figure 6.2 (b), is in steady operation and stable at

40 A after overshooting (around 5 %).

6.2.3 Fault mode of operation

When the fault is applied in unit 1, the fault current will flow through the system and will result in system collapse. The collapsed output voltage and current waveforms which represent the faulted system are shown in Figure 6.3 (a) and (b).

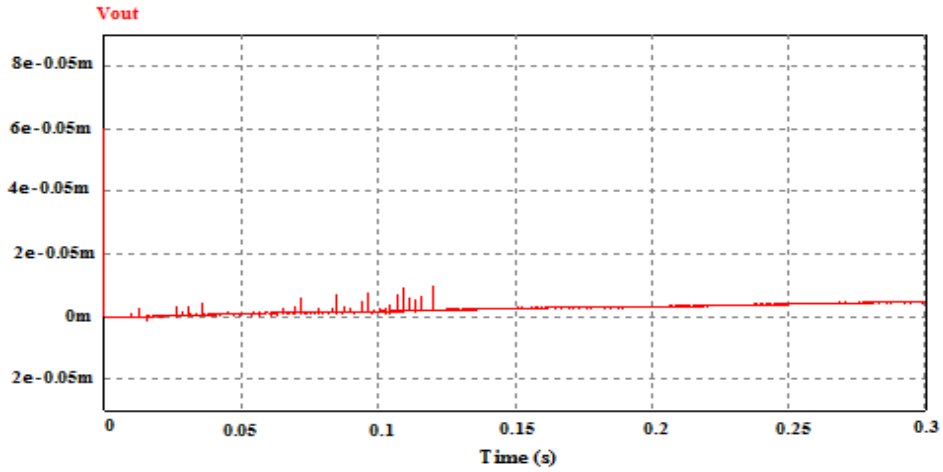

(a)

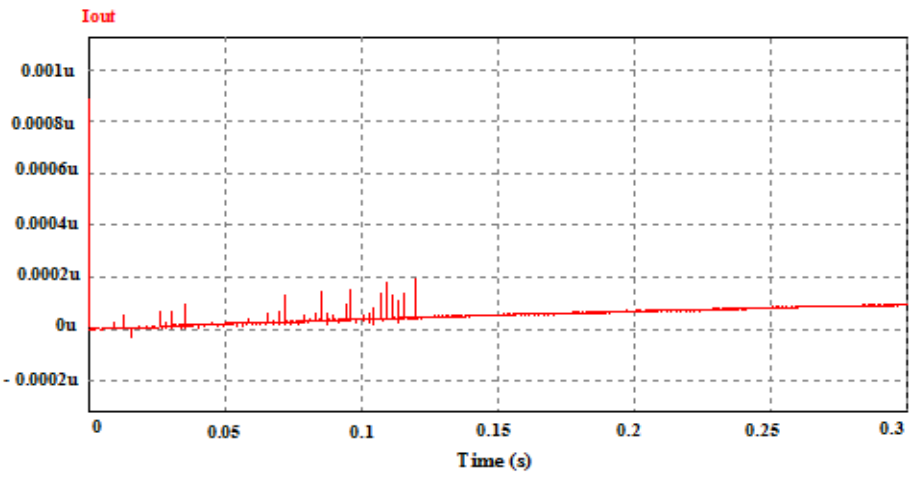

(b)

Figure 6.3. (a) Output voltage (b) Output current

6.2.4 FRT mode of operation

The FRT is achieved by connecting the controller that was proposed in Figure 6.1. Figure 6.4 shows the output voltage and current waveforms after applying FRT controller. The fault blocking diode and simulation results show that the controller can ride-through the fault properly because the output voltage and current waveforms are similar to steady-state operation "before applying the fault".

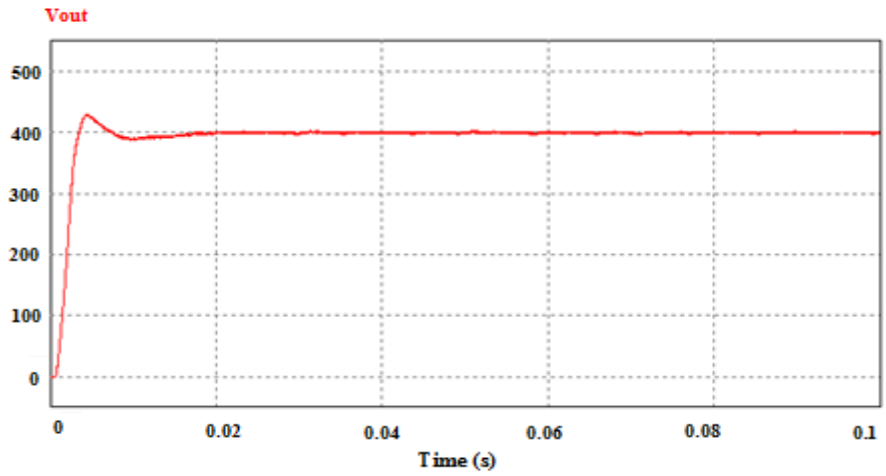

(a)

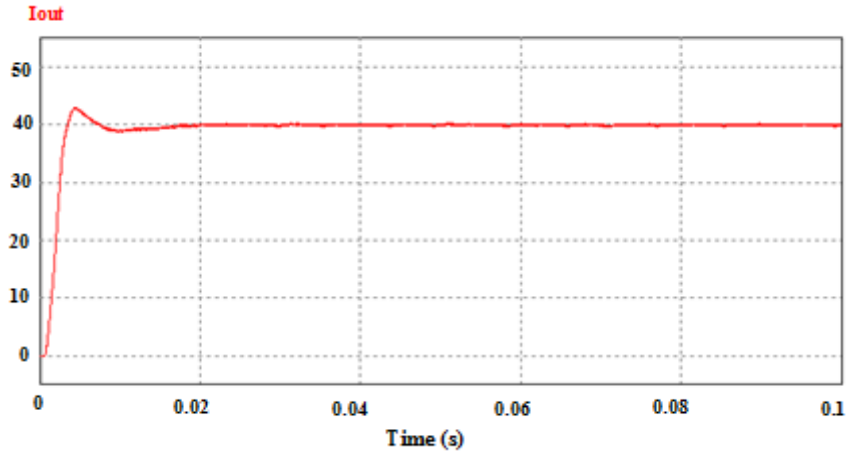

(b)

Figure 6.4. (a) Output voltage (b) Output current

In [120], a similar work is done using a fault blocking diode in a DC transmission line to block the fault current. They created a WECS based DC transmission technology to transfer unidirectional power into a faulted AC system while maintaining the capability to block DC faults. They considered control procedures including fault blocking diode and its performances under AC and DC faults using electromagnetic transient simulations, and they concluded that the topology is a viable candidate. They demonstrated that the fault blocking diode approach is a practical and efficient controller that participates in power system stability. The variation between this work and their work is that they used a line commutated converter and MMC as a MSC and a GSC, respectively. Here a Vienna-I feeding a DC load and a controller integrated with the fault blocking diode have been used.

6.3 THE VIRTUAL WIND FARM II MODEL

6.3.1 System analysis

The simulation analysis has been carried out using the data given in Table 6.2, as rated values. The system consists of three-generation units connected in parallel and integrated with power electronic converters via a DC-link and AC load, to study the transient performance of the system.

Table 6.2 Parameters used in the simulation program

Parameter	Value
Generator voltage rating	400 V
Generator power rating	16 kW
Turbine power rating	16 kW
Generator frequency	60 Hz
Load resistance	50 Ω
Load inductance	1 mH
ΔV_{pp}	5 %
ΔI_{pp}	5 %
Arm inductance, L_{arm}	0.001 mH
Sub-module capacitor, C_{SM}	14 μF

The simulated system consists of three primary circuits; the generation unit which consists of the turbine and PMSG, the Vienna rectifier-I circuit (Figure 6.5), and the MMC circuit (Figure 6.6).

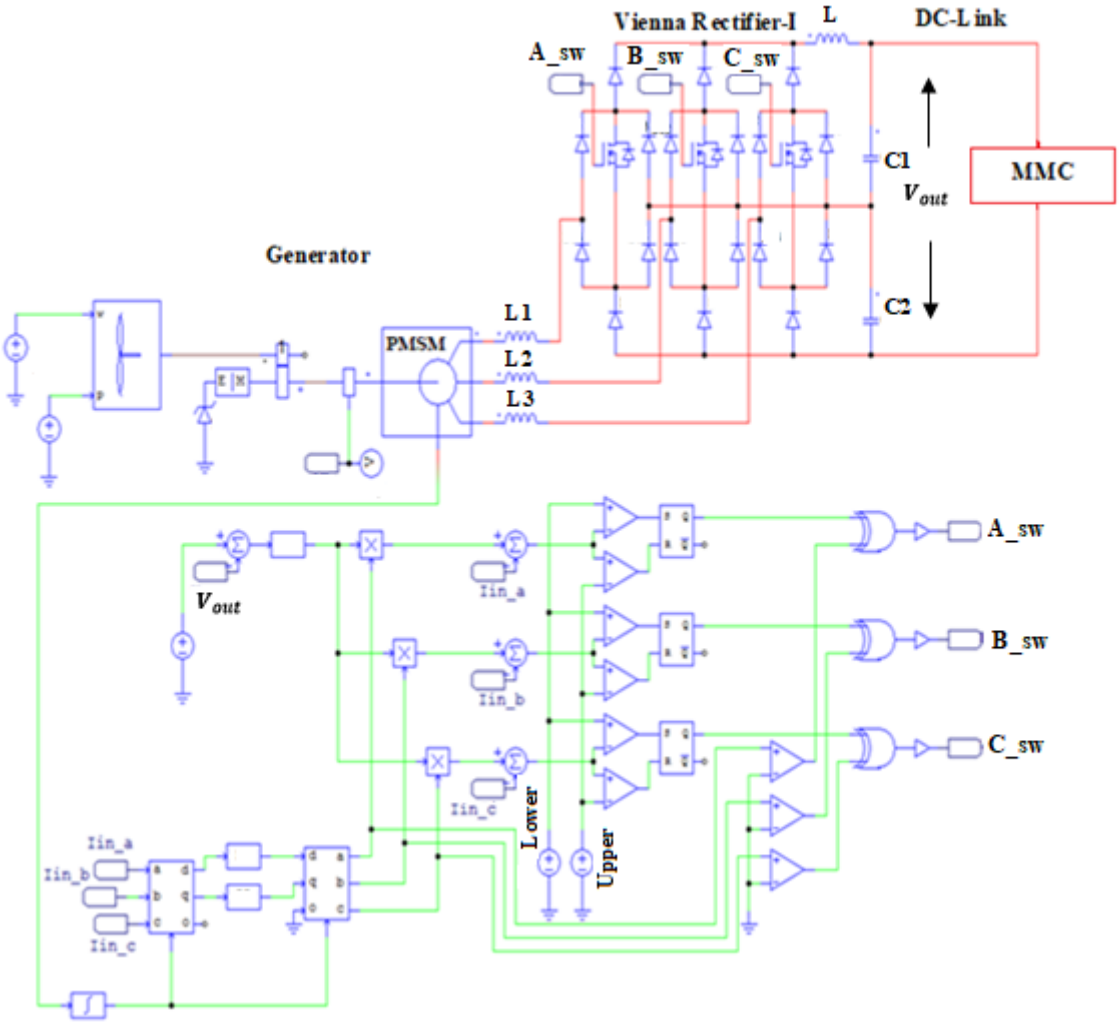

Figure 6.5. The rectifier-side simulated circuit

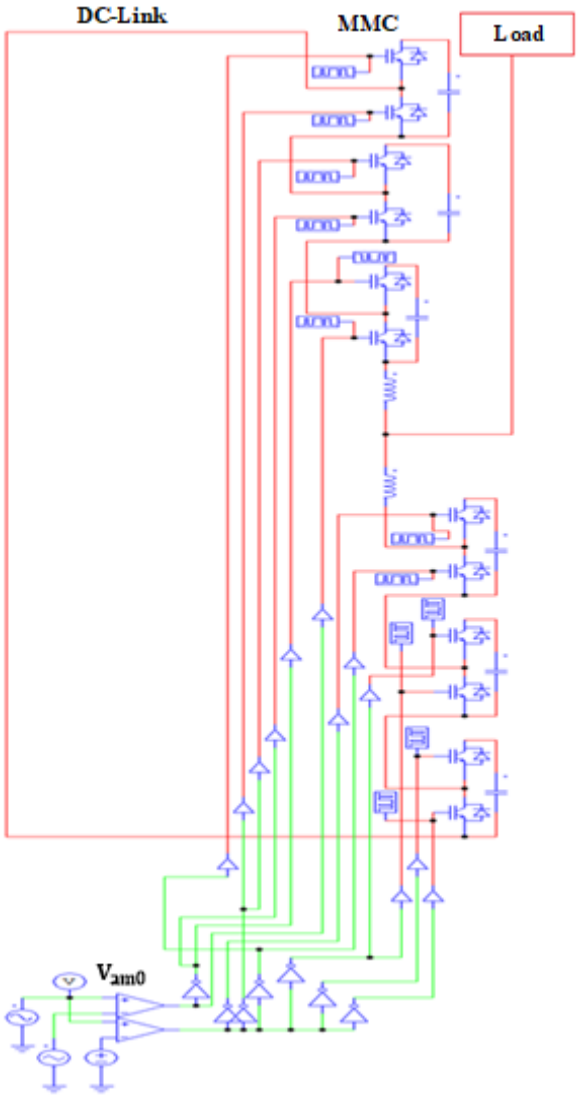

Figure 6.6. The inverter-side simulated circuit (one leg MMC) representation

The proposed sub-module is shown in Figure 6.7 (a). In the steady-state operation, the MMC runs with the half-bridge sub-module (the active switch 1 and active switch 2 are connected in parallel with the capacitor (Figure 6.7 (a)). The arm capacitor voltage is equal to V_{dc}/N, where V_{dc} is the DC-link voltage and N is the number of sub-modules per arm. In the instant of the DC-link fault occurrence, the diode D2 in each sub-module will create a path for fault current and will cause a trip of active switch 2.

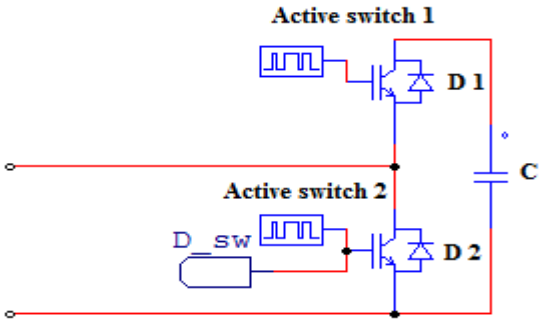

(a)

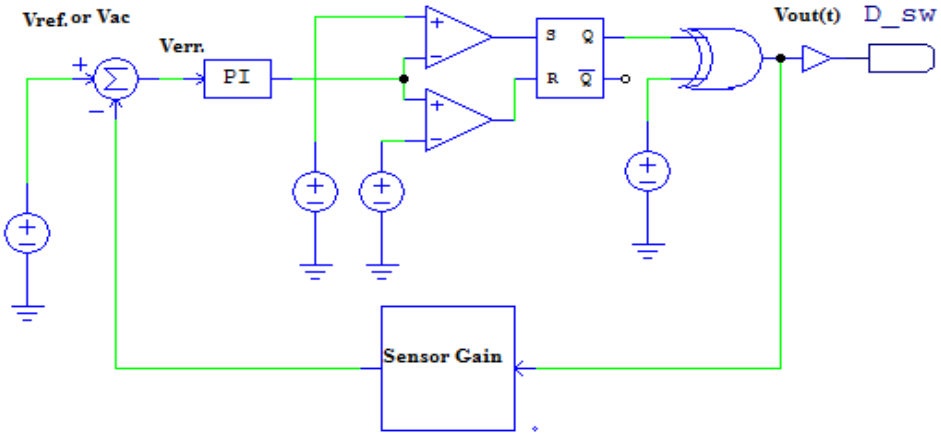

(b)

Figure 6.7. (a) Sub-module proposed topology (b) FRT controller circuit

When the current reaches the pre-defined value, the controller shown in Figure 6.7 (b), can sense the output voltage and instantly triggers the active switch 2 gates.

The fault blocking diode will block the fault, and the current starts flowing through the inverter. L_{arm} is expected to discharge, and the current through the inductance will increase. In this case, each active switch 2 is in ON state. This mode of operation is uninterrupted until the fault removal as shown in the flow-chart in Figure 6.8.

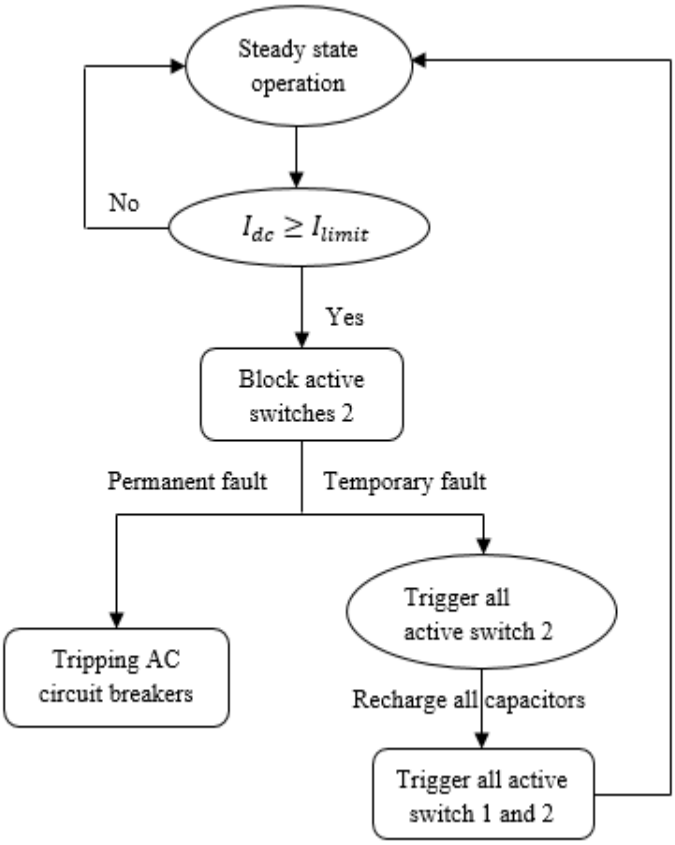

Figure 6.8. Flow chart of the FRT controller

The proposed strategy to ride-through the fault is uncomplicated and cost-competitive compared with other types of modules proposed in the literature. The fault blocking diode and the proposed sub-module topology were introduced to improve the FRT capability of the five-level three-phase MMC based DC transmission system.

The system is examined over several modes of operation, and the performance of the FRT controller is explained as follows:

6.3.2 Steady-state mode of operation

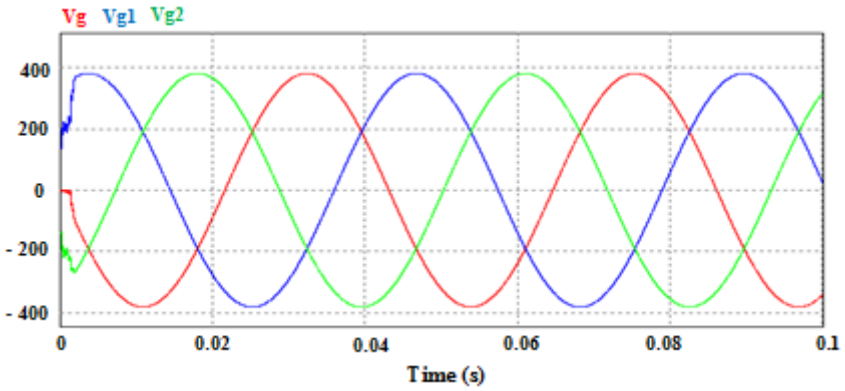

(a)

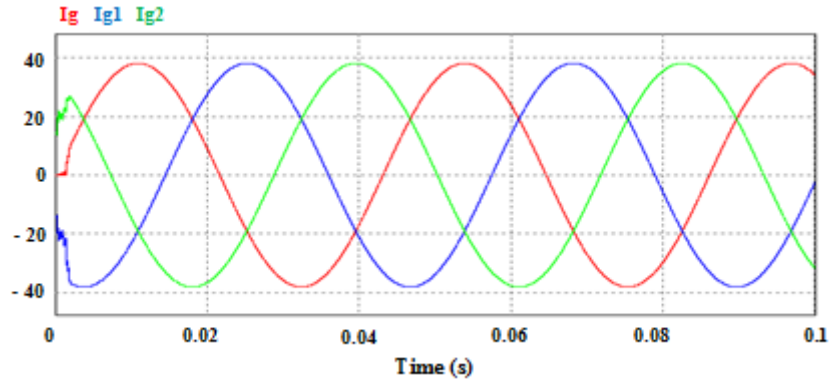

(b)

Figure 6.9. Generator output (a) Output voltage (b) Output current

Figure 6.9 (a) and (b) expresses the generator three-phase AC output voltage and current waveforms, respectively. The generator output voltage and current are 390 V and 38 A, respectively; there are small transients at the beginning of the wave due to generator starting.

6.3.3 Simulation results without using a fault blocking diode

In the steady-state operation mode, the system is tested with and without the use of fault blocking diode to demonstrate that the fault blocking diode can be treated as a permanent device that can be fixed in the system to clear the fault.

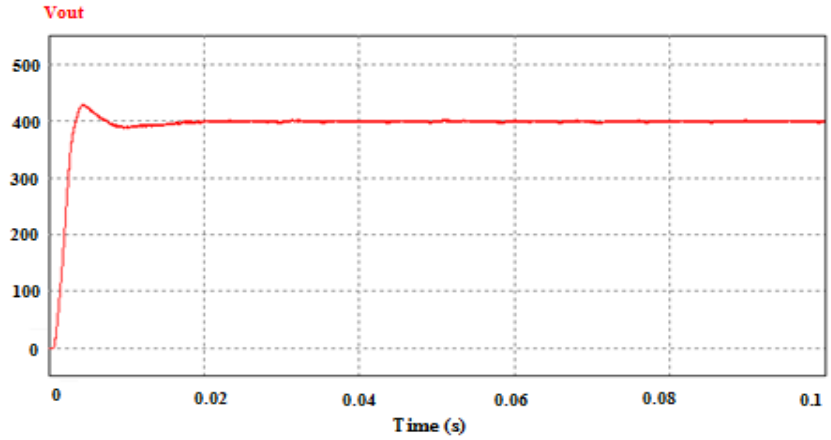

(a)

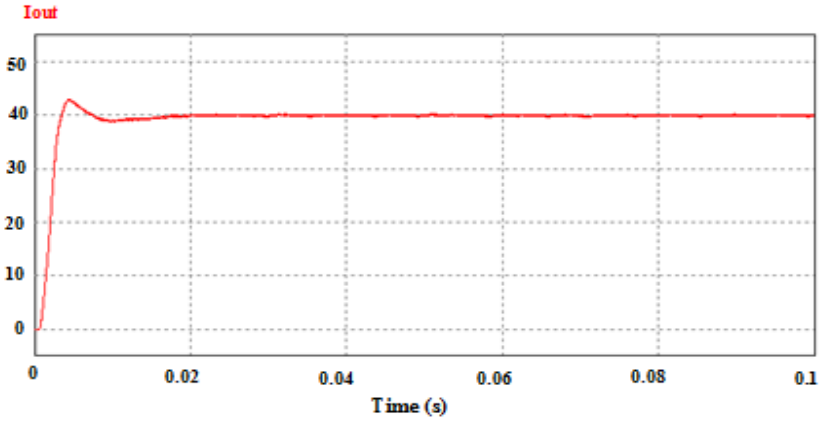

(b)

Figure 6.10. Rectifier output (a) Output voltage (b) Output current

The rectifier and inverter output voltage and current magnitudes when the system runs at the steady-state mode of operation are shown in Figures 6.10 and 6.11, respectively. The rectifier output voltage and current are around 400 V and 40 A, respectively, with quite small ripple magnitudes. The accepted ripple percentage is around 5 % for the voltage and current. The positive points of these waveforms are (i) less transient time; 0.01 s for voltage and current waveforms (ii) no under or overshooting in the waveforms (iii) high output voltage and current values compared with the rectifier input values; due to the boost ability of the rectifier (iv) small ripple percentage; around 5 % for voltage and current.

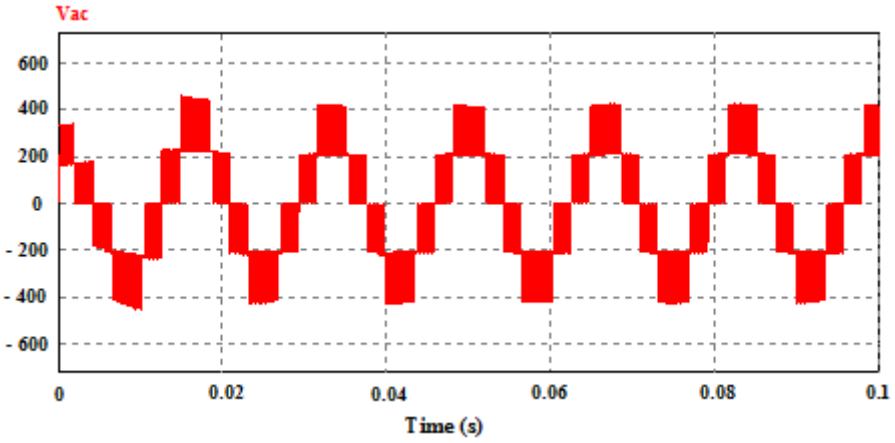

(a)

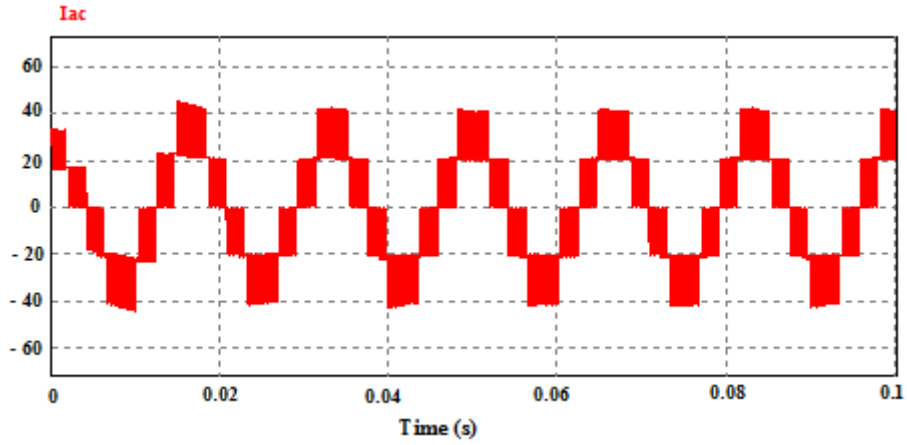

(b)

Figure 6.11. Inverter output (a) Output voltage (b) Output current

The inverter output voltage and current values are around 400 V and 40 A, respectively. V_m is equal to 480 V, and I_m is equal to 48 A. The THD is 1.2 % for AC voltage and current waves at a switching frequency of 60Hz. It was observed that there are not many transients of the voltage and current waveforms. As shown in Figure 6.11 (a) the peak value of the first cycle of the voltage wave is around 320 V, for the second cycle, the peak value is around 480 V, and the rated value of the rest is around 400 V.

From Figure 6.11 (b) the peak value of the first cycle of the current wave is around 32 A. For the second cycle, the peak value is around 48 A, and the rated value of the rest is 40 A.

It can be concluded that a stable voltage and current waveforms can be obtained.

6.3.4 Simulation results with the use of fault blocking diode

In the steady-state operation with the permanent use of fault blocking diode, the rectifier and inverter output voltage, and current waveforms can be drawn as shown in Figures 6.12-6.14.

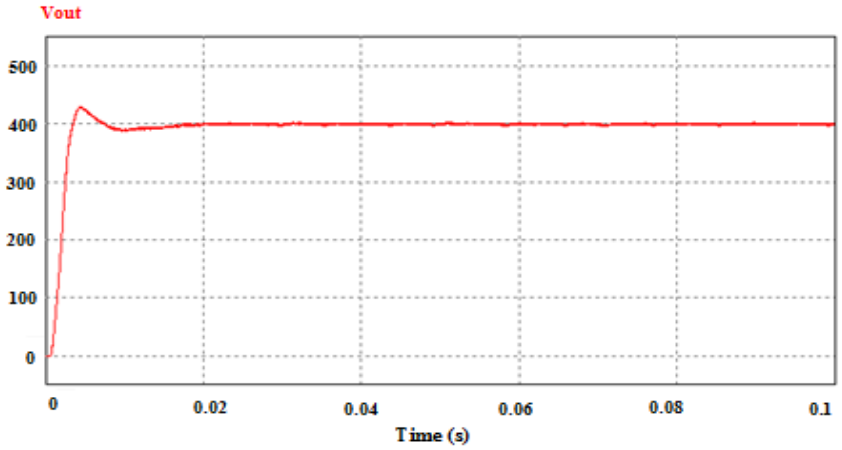

(a)

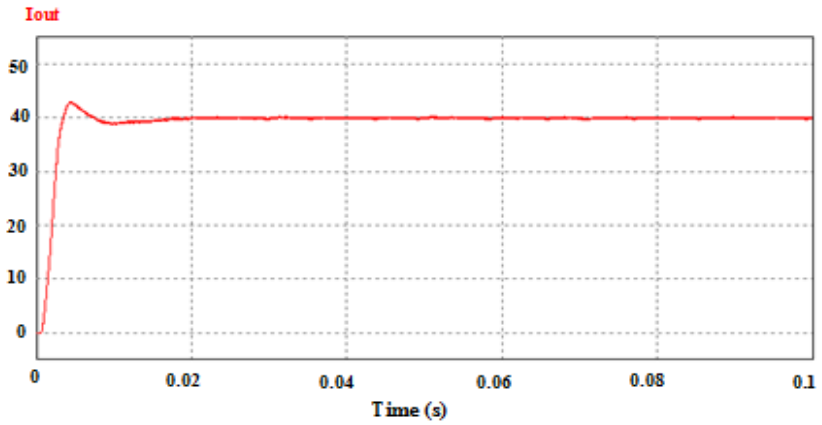

(b)

Figure 6.12. Rectifier output (a) Output voltage (b) Output current

The rectifier output voltage and current magnitudes are around 2300 V and 47 A, respectively, with small ripple magnitudes. The rectifier output in Figure 6.12 (a) and (b) is similar to Figure 6.10 (a) and (b).

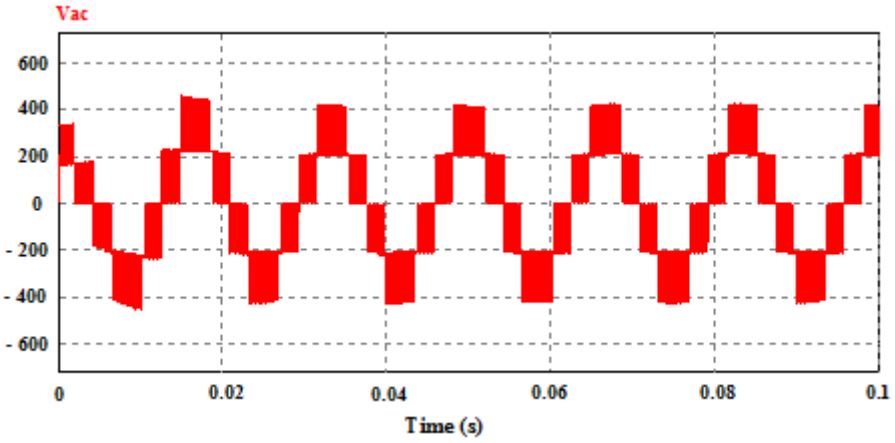

(a)

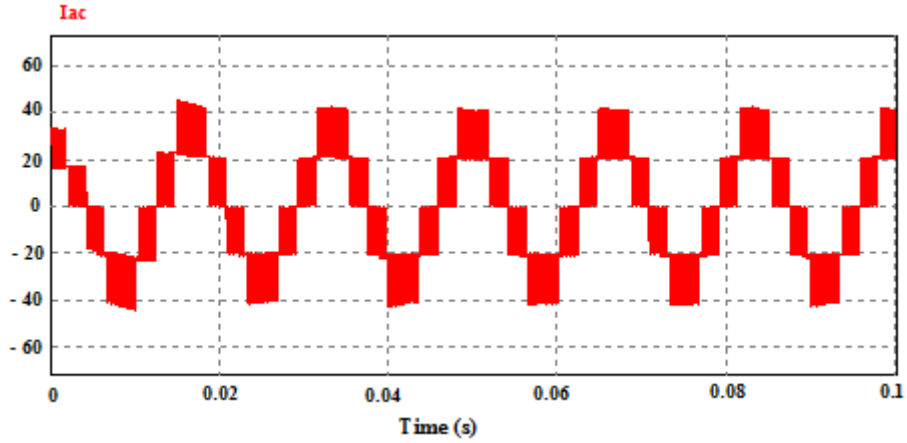

(b)

Figure 6.13. Inverter output (a) Output voltage (b) Output current

The inverter output voltage and current values in Figure 6.13 (a) and (b) are around 400 V and 40 A, respectively. Also, the waves shown in Figure 6.13 and Figure 6.11 are identical. Comparing Figure 6.13 with Figure 6.11, and Figure 6.12 with Figure 6.10; it can be concluded that the fault blocking diode can be used permanently in the practical power circuit for blocking the DC fault.

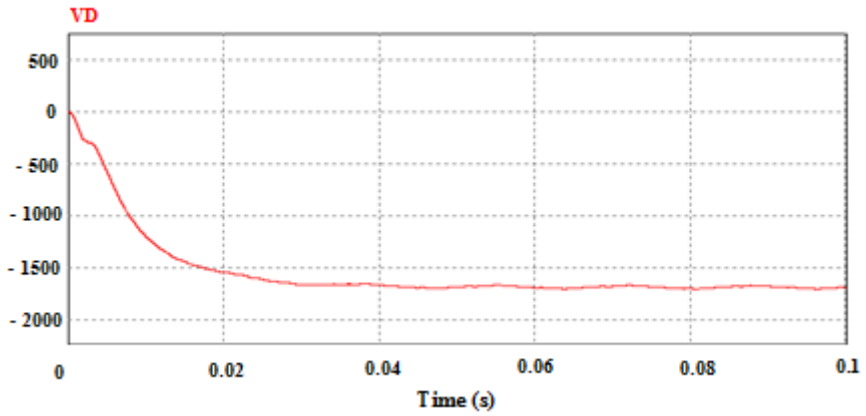

(a)

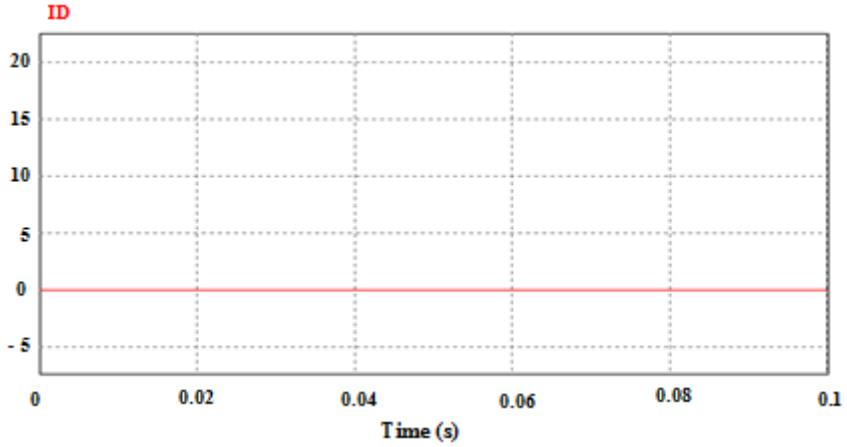

(b)

Figure 6.14. (a) Voltage across the fault blocking diode (b) Current across the fault blocking diode

The voltage across the fault blocking diode shown in Figure 6.14 (a) has a peak inverse value of 1700 V, and the current wave shown in Figure 6.14 (b) has zero value because of diode reverse mode. The diode blocking current and voltage are 200 A and 5000 V. Voltage and current ratings are also 5000 V and 200 A, the forward voltage is 1.1 V.

6.3.5 Operation under transient fault conditions

Short-circuit fault was applied in a DC-link for one unit. The DC and AC output voltage and current waveforms are shown in Figures 6.15 and 6.16; the rectifier and inverter output voltages and currents are zero magnitude due to short-circuit fault in a DC-link.

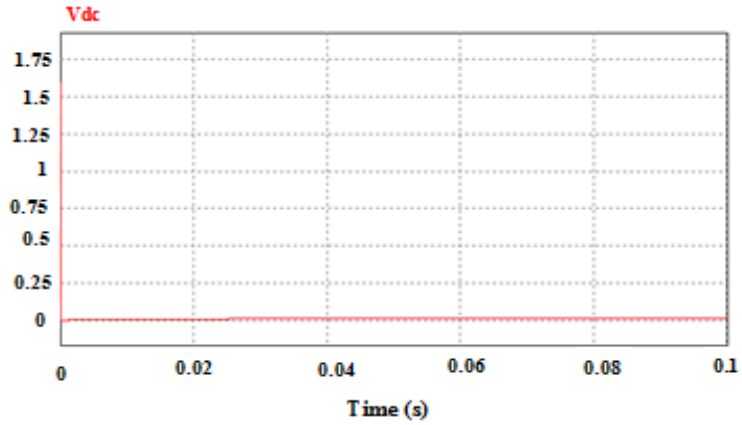

(a)

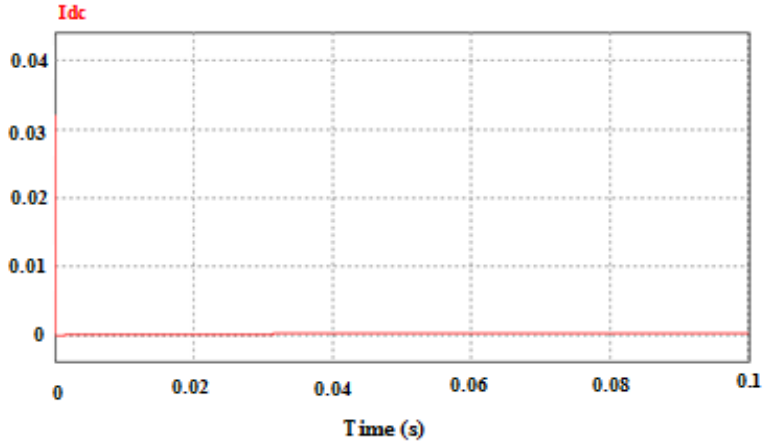

(b)

Figure 6.15. Rectifier output (a) Output voltage (b) Output current

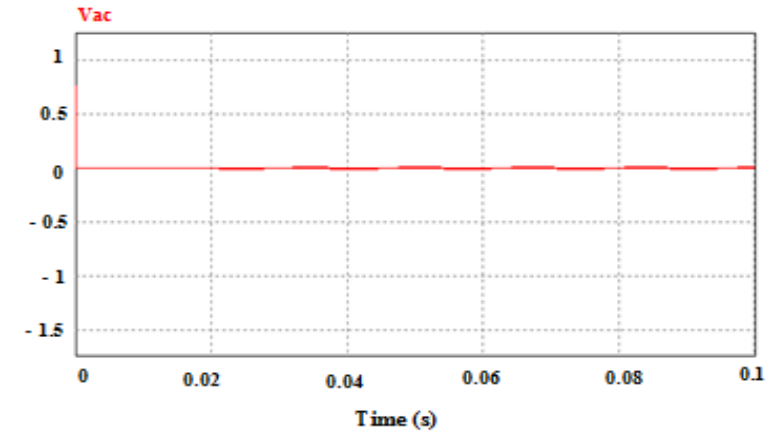

(a)

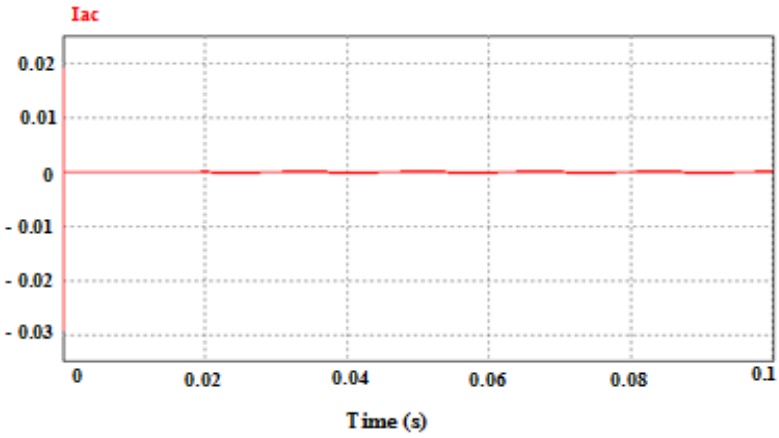

(b)

Figure 6.16. Inverter output (a) Output voltage (b) Output current

6.3.6 FRT controller's mode of operation

The rectifier output voltage and current are around 400 V and 40 A as shown in Figure 6.17 (a) and (b), with small ripple magnitudes. The positive points of these waveforms are (i) less transient time; 0.01 s for voltage and current waveforms (ii) no under or overshooting in the waveforms (iii) high output voltage and current values compared with the rectifier input values; due to the boost ability of the rectifier (iv) small ripple percentage; around 5 % for voltage and current.

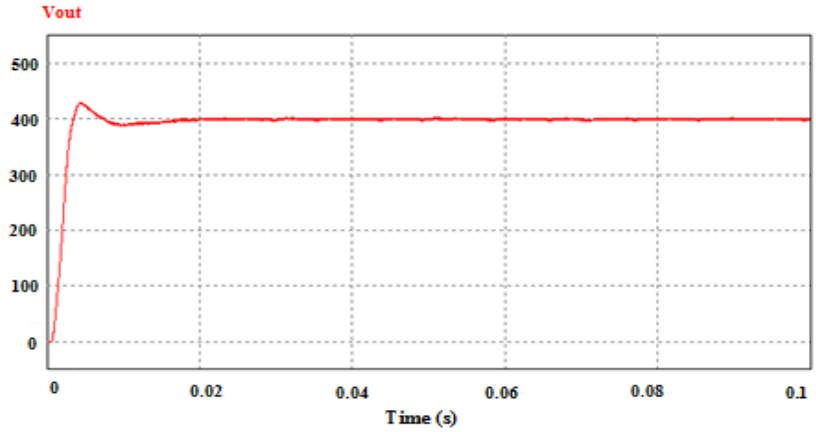

(a)

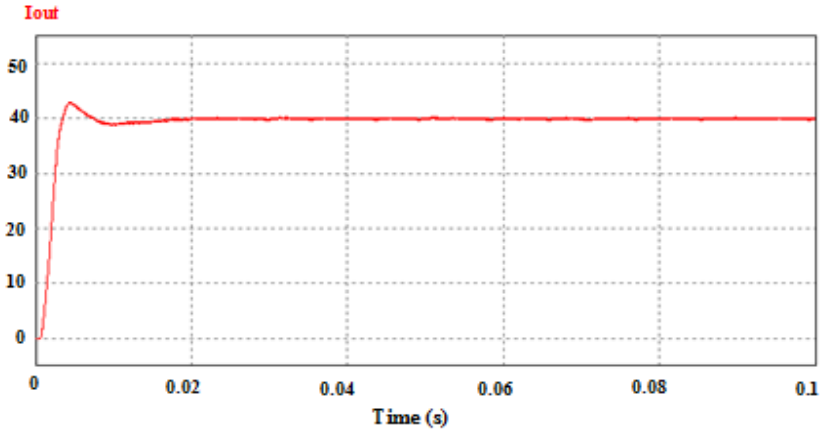

(b)

Figure 6.17. Rectifier output (a) Output voltage (b) Output current

The inverter output voltage and current values are around 400 V and 40 A, respectively. V_m is equal to 480 V, and I_m is equal to 48 A. The THD is 1.2 % for AC voltage and current waves at switching frequency of 60 Hz. The critical feature of these waveforms is fewer transients of the voltage and current waves.

For the first cycle of the voltage waveform shown in Figure 6.18 (a), the peak value is around 320 V, for the second cycle wave the peak value is around 480 V, and the rated value for the rest is 400 V. For the first cycle of the current wave shown in Figure 6.18 (b), the peak value is around 32 A, for the second wave the peak value is around 48 A, and the rated value for the rest is 40 A.

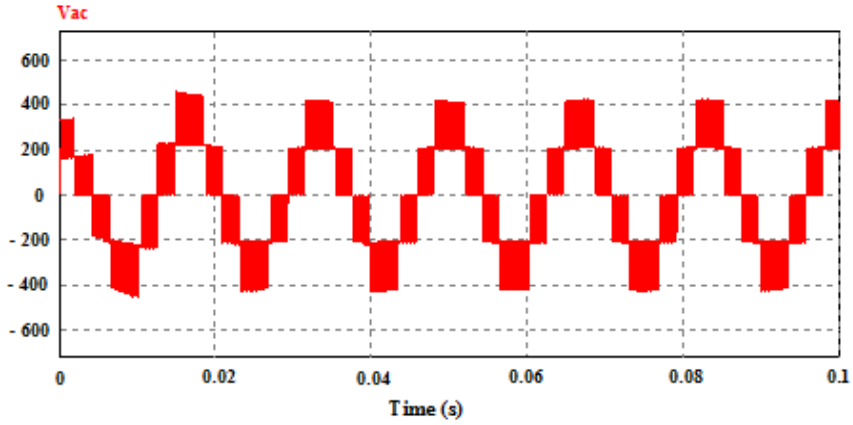

(a)

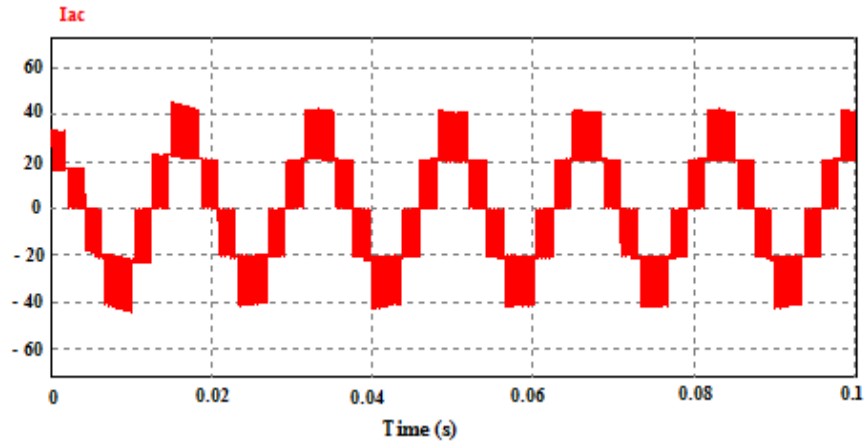

(b)

Figure 6.18. Inverter output (a) Output voltage (b) Output current

The rectifier and inverter output voltages and currents shown in Figures 6.17 and 6.18, respectively, are in steady-state operation. Thus, the FRT controller is reliable.

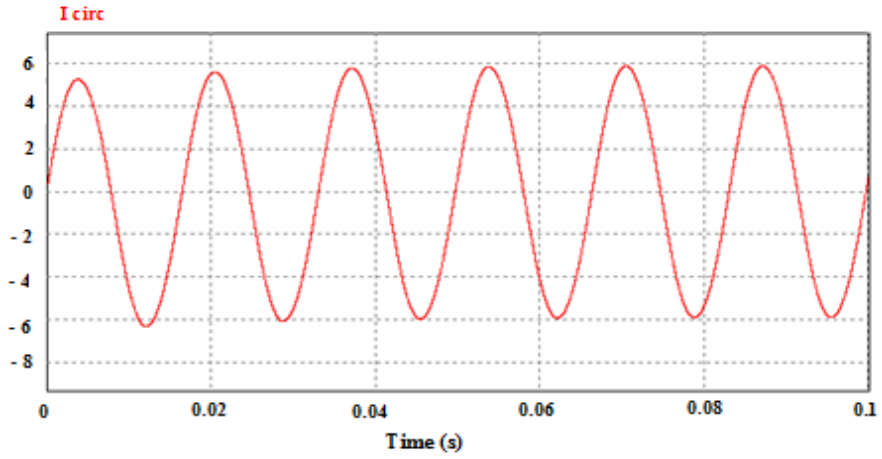

Figure 6.19. Circulating current

The AC waveform representing the circulating current is shown in Figure 6.19. The magnitude of the circulating current is around 6 A, i. e. 15% of the output current, which is an acceptable percentage and indication of robust design of arm inductance and sub-module capacitance.

6.3.7 Fault time determination

In the absence of the controller, the switching versus output voltage will be as shown in Figure 6.20, V_{sw} expresses the switching voltage and V_{ac} is the AC output voltage. The voltage is fluctuating at the instant of the fault occurrence from -0.0008 to zero volt due to sudden short circuit.

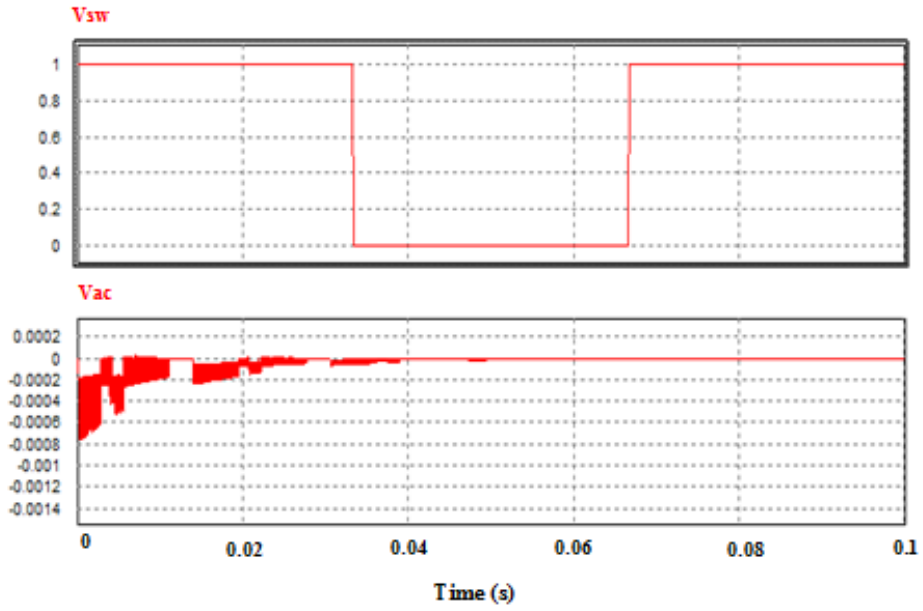

Figure 6.20. Switching versus output voltage

The voltage has less value because the measurement is applied at the moment of fault occurrence, and this fluctuation will continue from 0 to 0.035 s from the beginning of the fault (i. e. the fault time is 0.035 s).

6.4 THE VIRTUAL WIND FARM III MODEL

6.4.1 System analysis

The WPP, which consists of three parallel-connected WECUs supplying a DC load at a cost of 3012.5 USD; for building a system consisting of fifty-four diodes, nine IGBT switches, three AC power supplies, and DC load resistor, is simulated and discussed. The values used in a simulation are shown in Table 6.3. An AC fault is applied to unit 2 terminals as shown in Figure 6.21. This type of fault is due to unbalance between phases and is called an unsymmetrical shunt fault. A shunt fault is defined as “an unbalance between phases or between phase and ground”. A series fault is defined as “an unbalance in the same line impedances” [121].

Table 6.3 Parameters used for the simulation

Parameter	Description	Value
E	Rated voltage of the PMSG	400 V
R	Generator resistance	1 Ω
L	Generator inductance	2 mH
I	Generator rated current	40 A
f	Generator frequency	60 Hz
Ro	Load resistance	50 Ω
Co	Rectifier output capacitor	2000 μF

Shunt faults are an essential class of faults and include various types of short circuits as well as unbalanced loads, and can be summarized as follows:

1. Line to ground faults
2. Line to line faults.
3. Double line to ground faults
4. Triple line to ground faults [121-126]

In this model generator, line to ground and double line to ground faults have been discussed. Figure 6.21 explains the simulated system. If the fault current exceeds the thermal capability of the Vienna rectifier-I valves, the IGBT switch will be blocked, and the system will stop operating until the fault is cleared. In such a case, the system needs to be restarted.

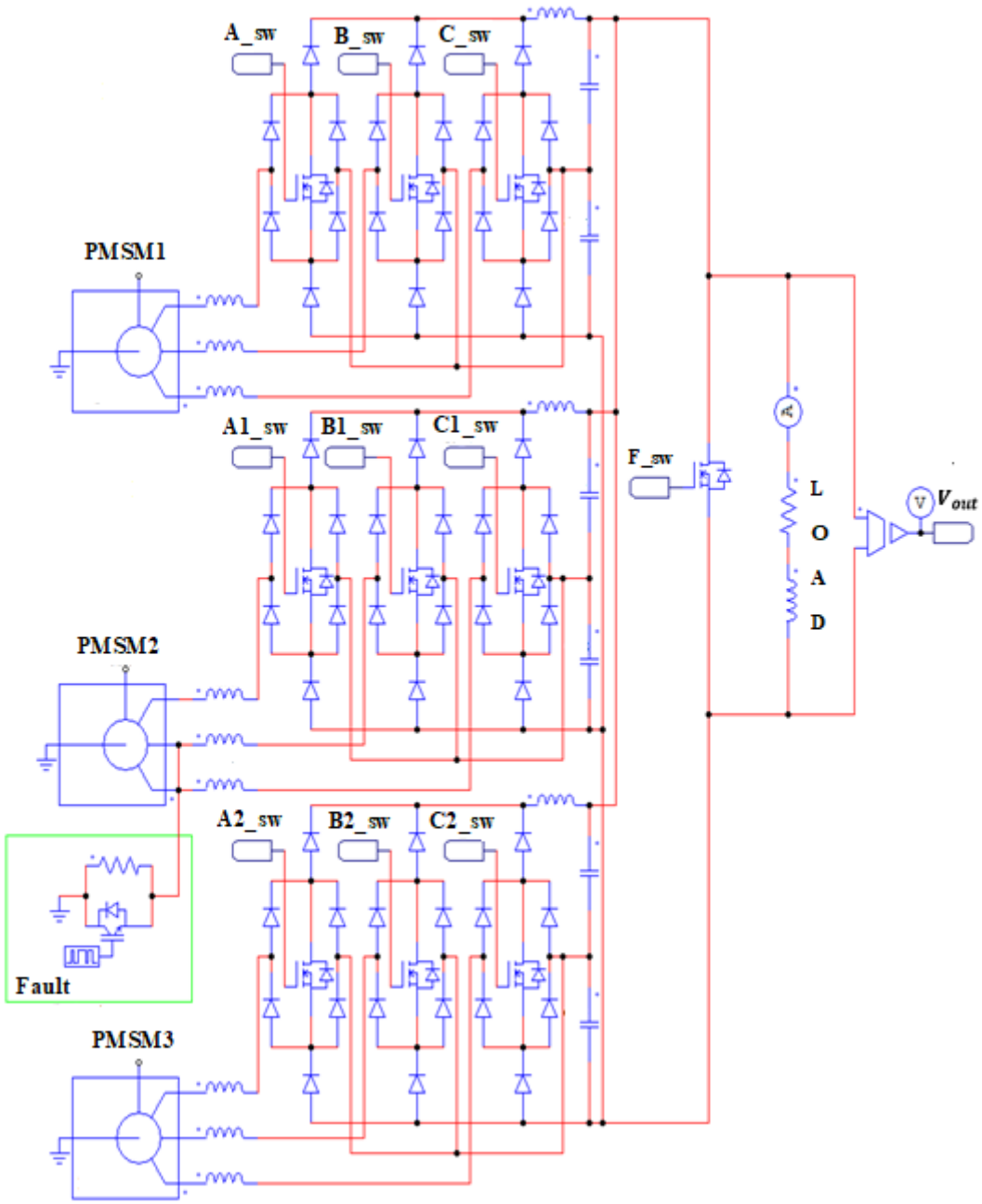

Figure 6.21. The simulated system considering the fault in generator 2

Figure 6.22 shows the FRT controller. The rectifier output voltage $V_{out}(t)$ is sensed with the sensor gain H (s), the sensor output will be $H(s) \times V_{out}(s)$ which is compared with a reference input voltage $V_{ref}(s)$. In case of disturbances or component variations in the compensator, the difference in the V_{ref} "the input voltage reference" and $H(s) \times V_{out}(s)$ "the sensor output" is named an error signal.

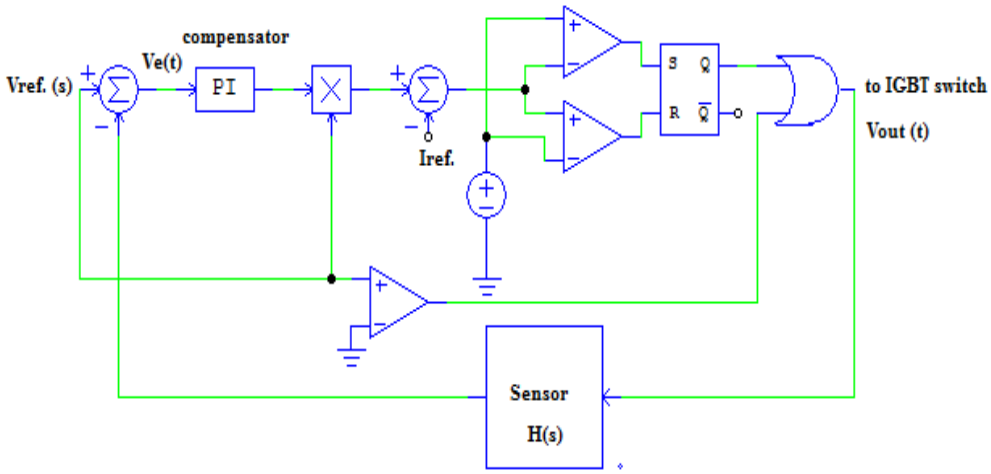

Figure 6.22. Schematic diagram of the FRT controller

The aim is to let H (s)×Vout (s) equal to Vref (s) to obtain zero error, but practically, the error signal is commonly a small value. The output of the controller is the gate triggering circuit (F_sw) which is shown in Figure 6.21. The proposed sub-module control circuit has been constructed to reduce the fault effect. The recent grid codes require that AC generator based variable speed WPP should be holding in operation during fault cases.

6.4.2 Steady-state mode of operation

At the steady-state operation, the switch will be locked for a long time, so the voltage and current waves are in stable performance. Figure 6.23 shows the generator AC output voltage is 390 V, and the current is 38 A. There are small transients at the beginning of both voltage and current waves, due to the starting of the generator.

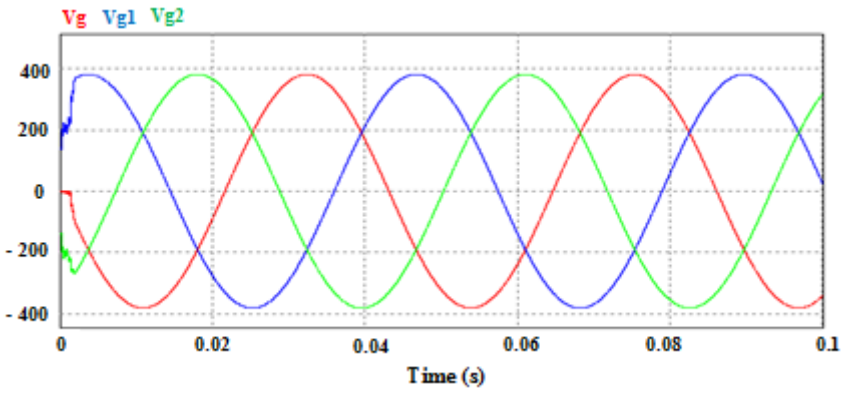

(a)

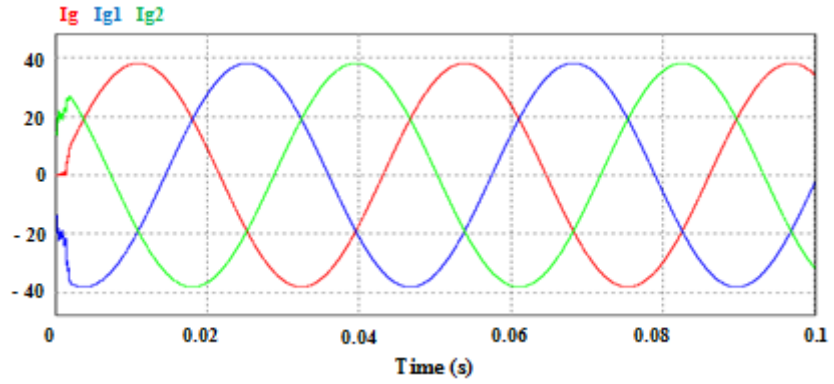

(b)

Figure 6.23. Generator output (a) Output voltage (b) Output current

Figure 6.24 (a) and (b), shows the rectifier output voltage and current waveforms. The output voltage is in steady-state condition and is stable at 400 V after overshooting to 420 V due to system start-up. Same as the output voltage, the output current is in regular performance and stable at 40 A after overshooting up to 52 A.

The positive points of these waveforms are (i) less transient time; 0.03 s for voltage and current waveforms (ii) the under and overshooting are running in a short time and one cycle; in 0.025 s; 152 V overshooting and 50 V undershooting, 12 A overshooting and 5 A undershooting (iii) no ripple disturbance in the voltage and current waves.

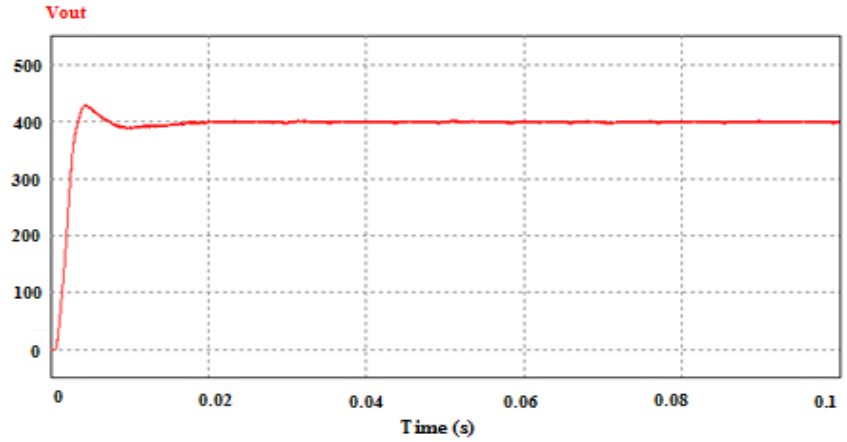

(a)

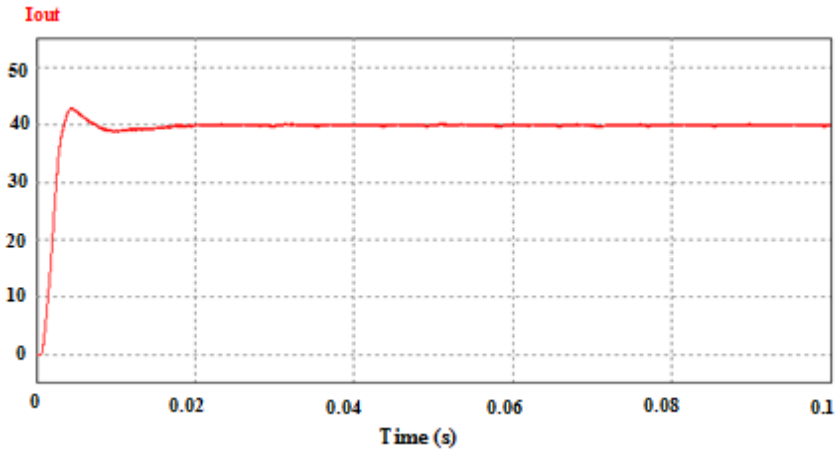

(b)

Figure 6.24. Steady-state components (a) Output voltage (b) Output current

6.4.3 Unsymmetrical fault simulation

6.4.3.1 Line to ground fault

When the line to ground fault occurs, the output parameters are still the same as steady-state parameters because of the parallel connection of units; if the unit collapses, the system remains in synchronism.

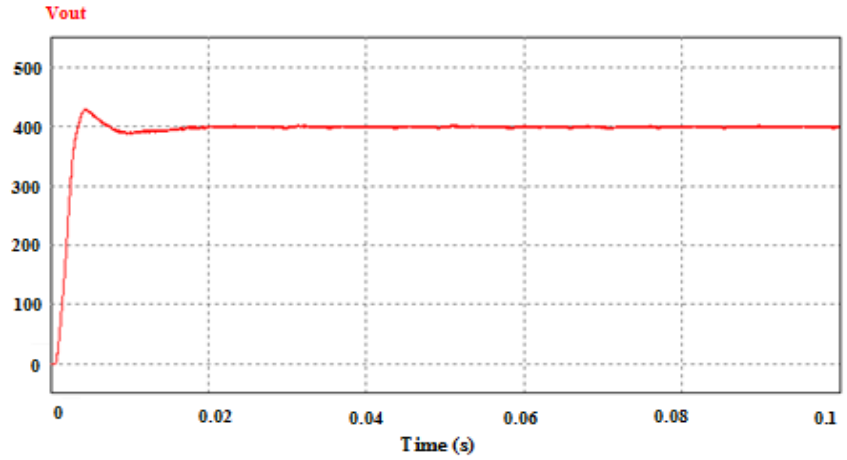

(a)

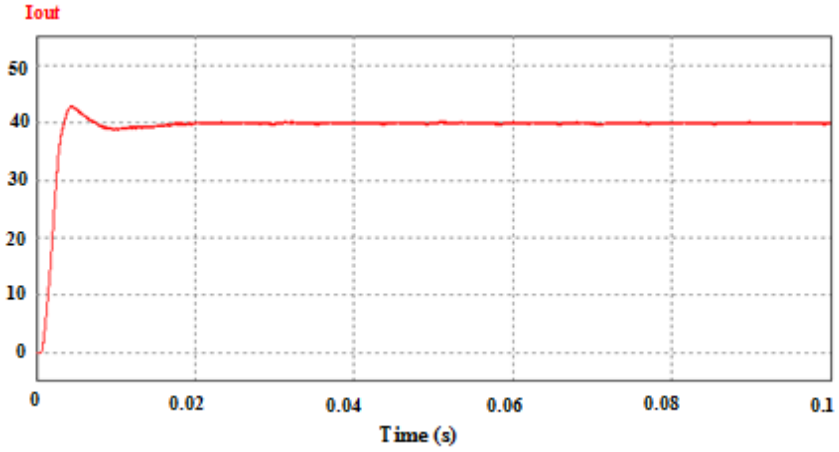

(b)

Figure 6.25. (a) Output voltage (b) Output current

Figure 6.25 (a), shows the output voltage waveform; which is identical to the steady-state value and stable at 400 V after over and undershooting at one cycle of around 102 V or 25.5 % from the original voltage value, and down to around 50 V or 12.5 % from the original voltage value. Also, the output current in Figure 6.25 (b), is stable and constant at 40 A after small overshooting (due to switching) up to 11 A or 27.5 % from the original current value, and undershooting to 5 A or 12.5 % from the original current value. The transients in voltage and current waves are continuing for very few seconds, approximately 0.025 s.

6.4.3.2 Double line to ground fault

When applying double line to ground fault as shown in Figure 6.26 (a) and (b), the output voltage and current waves fluctuate (current is fluctuating through the load) due to the fault.

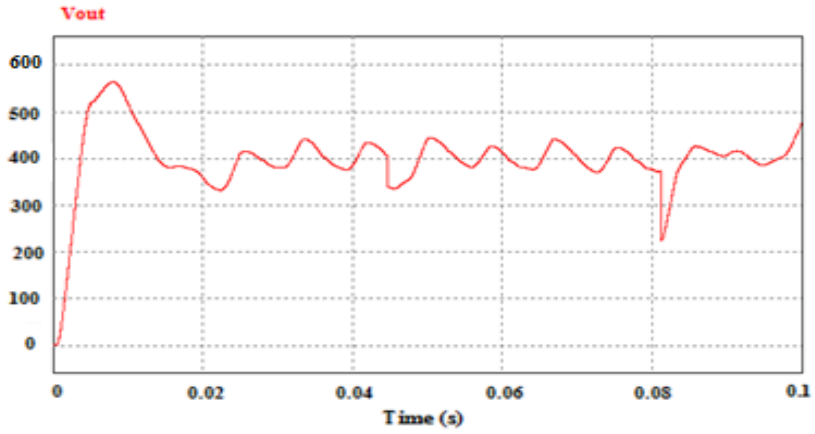

(a)

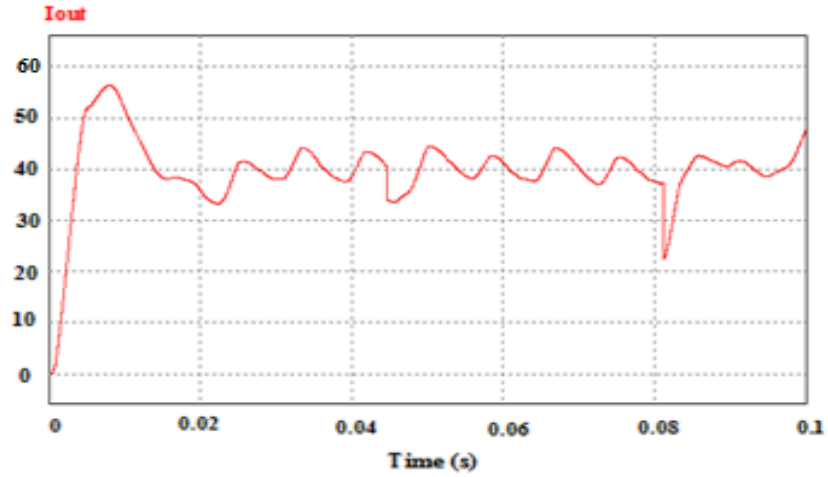

(b)

Figure 6.26. (a) Output voltage (b) Output current

The output voltage, as presented in Figure 6.26 (a) is fluctuating around 400 V, with overshooting up to about 560 V and shooting down to about 215 V. The output current wave, as indicated in Figure 6.26 (b), is fluctuating through 40 A after overshooting up to 56 A and shooting down to 21 A.

6.4.4 FRT controller

Figure 6.27 shows the voltage and current waveforms when the faulted system runs with the use of a controller; for two line to ground fluctuation faults, to enhance the system stability and reliability; by allowing the path of current from capacitors through the diodes and the rectifier to the load. If the switch is opened, the diode will become forward-biased, relative to the capacitors.

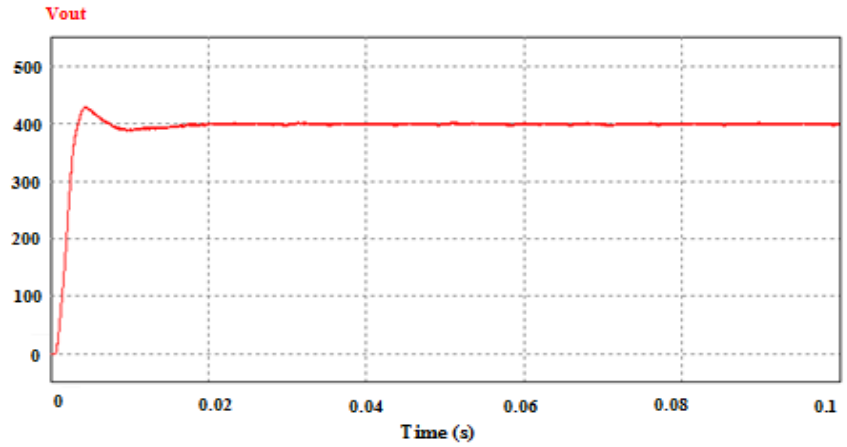

(a)

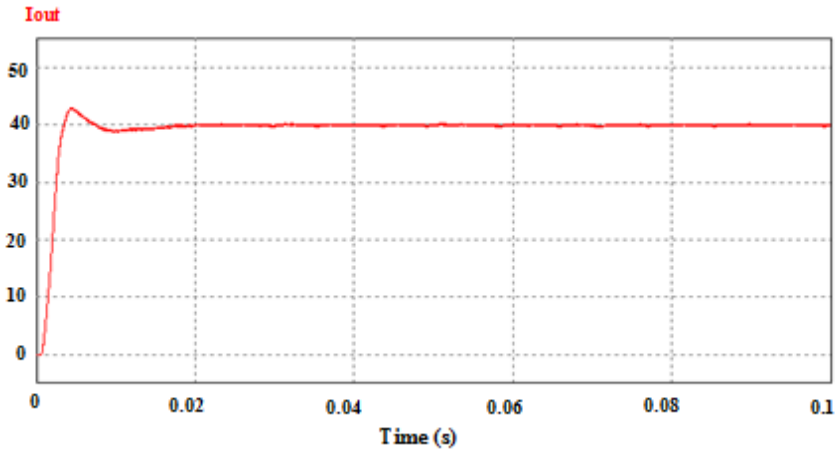

(b)

Figure 6.27. (a) Output voltage (b) Output current

The voltage and current magnitudes are around 400 V and 40 A, with accepted voltage and current ripple percentage; around 1.3 % for both. There is overshooting in a voltage wave

around 110 V or 27.5 % of the original voltage value due to switching and continuing for only one cycle. Also, there is shooting down 20 V or 5 % of the original voltage value. For the current wave, there is shooting up about 12 A or 30 % of the original current value and shooting down about 3 A or 7.5 % of the original current value.

6.4.5 Simulation under steady-state operation with the use of a FRT controller

The proposed FRT components simulated with the system in steady-state operation i.e. treated as permanently occupied with the system for economical operation, the voltage and current waveforms are presented in Figure 6.28 (a) and (b).

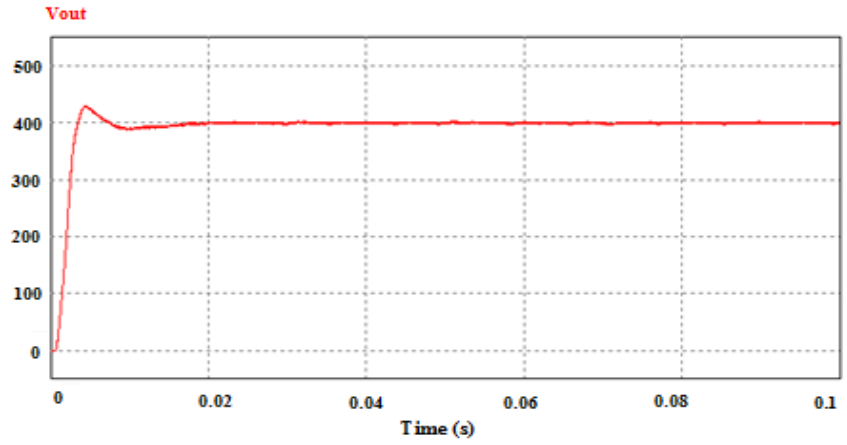

(a)

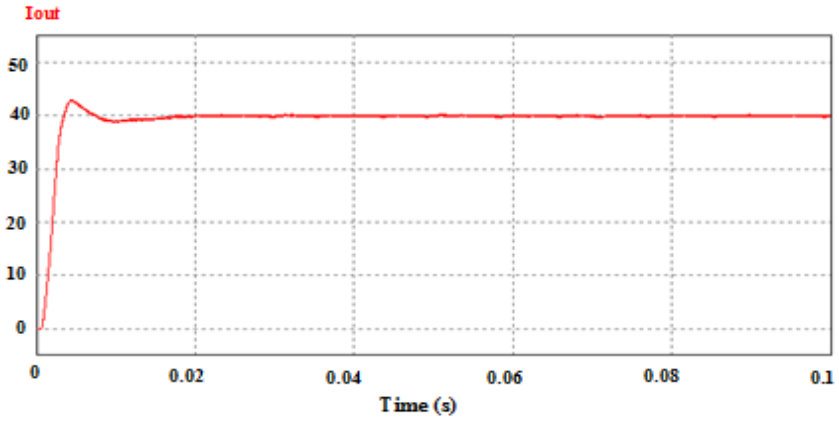

(b)

Figure 6.28. (a) Output voltage (b) Output current

At steady-state condition, the voltage and current magnitudes are 400 V and 40 A, and there is no observed ripple in the waveforms. The transient time for both voltage and current waves is around 0.01 s. There is 20 V overshooting or 5 % of the original voltage magnitude due to switching. There is also shooting up to about 2 A or 5 % of the original current magnitude for the current wave.

While the FRT controller has been treated as permanently occupied within the original system, as presented in Figure 6.28 (a) and (b), the system remains in a stable condition in a technical and economical operation. Thus, it will not result in generation loss, and there is no need for the auxiliary circuit to control the sub-module to operate when needed.

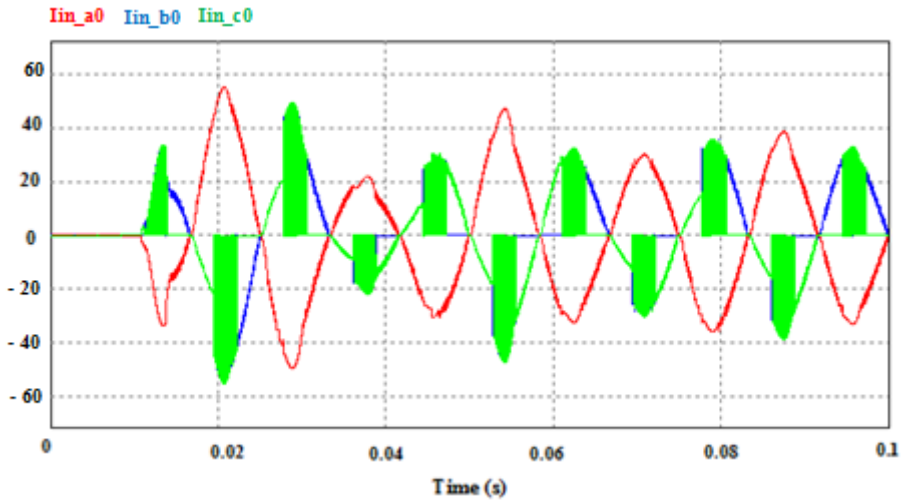

Figure 6.29. Generator output currents while the double line to ground fault occurs

The operation under the unsymmetrical fault creates unbalanced currents between phases and torque pulsations, as shown in Figure 6.29. If this situation is continued long-term, the unbalanced currents might produce heating in the three-phases, which affects the insulation of windings and operation under symmetrical fault turns to high short circuit currents at the fault location [28].

Vsw, as shown in Figure 6.30, is a switching voltage, Vout is a DC output voltage. The rated voltage is 400 V and the acceptable error is around $\pm$ 5 %, so it is from 440 V up and 300 V

down. The fault time started when the voltage was fluctuating from 300 V until 470 V at 0.06 s, and the fault clearance time should be after 120 ms.

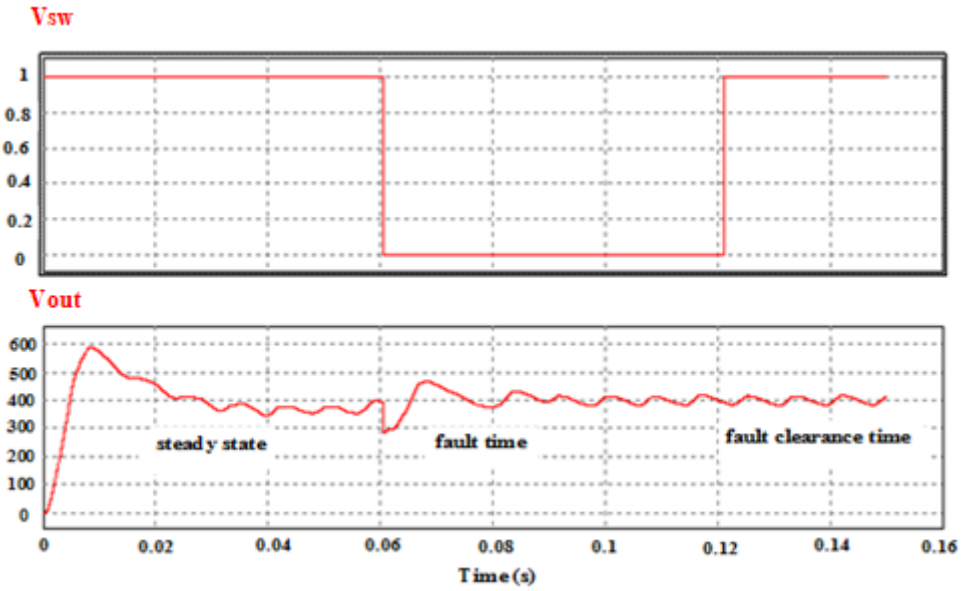

Figure 6.30. Switching and output voltages to clarify the fault time

6.5 CHAPTER SUMMARY

In this section, three virtual wind farms structures of generation units supplying a DC or AC load-based DC transmission link are simulated and discussed. The objective is to ride-through AC and DC faults, to ensure the power stability and sustainability considering an economical operation. Section 6.2 presents a system consisting of three WECUs connected in parallel and supplying a DC load, and the fault is proposed to be at the DC-link, which is detected by a fault blocking diode and a controller. In Section 6.3, three WECUs integrated with power electronic converters supplying an AC load are proposed. A fault blocking diode and a FRT controller circuit are used to protect the system by controlling the inverter side. An unsymmetrical fault is cleared in Section 6.4 with the use of FRT controller in a system consisting of three WECUs connected in parallel feeding a DC load. It was observed that AC and DC faults can be cleared with the use of fault blocking diode and FRT controllers, to maintain power stability and system reliability

CHAPTER 7 CONCLUSION AND FUTURE WORK

7.1 STUDY SUMMARY AND RESULTS

In this study, three virtual wind farms have been proposed and simulated. The first one has presented an improved topology with a FRT capability when subjected to a DC-link fault based WPP employing a Vienna active rectifier-I. The proposed system is capable of mitigating a fault occurring on the DC-link side using the PWM-controller technique implemented on the Vienna active rectifier. The simulation results presented the performance of the proposed FRT capability controller, which involve sub-modules consisting of controller and fault blocking diode. The fault blocking diode has detected the fault very fast and protected power system from thermal over stresses with the controller assistance, by creating a new current path to eliminate the fault current effect.

This work proved that the unidirectional HVDC scheme could protect the transmission line from the transient faults that can occur due to a short circuit. The current and voltage loop controllers have been designed to maintain a constant voltage at steady-state conditions. Also, the supply side filter that consists of inductor and capacitor has been designed in order to decrease the input voltage and current ripple values. Simulation results demonstrate the suitability of the control strategy. The use of proposed WECU topology has led to the improvement of system stability by maintaining the constant output voltage. The WECU combining Vienna active rectifier-I is also confirmed as a feasible technology that can be operated in a large-scale renewable power generation, to recognize technical and economical efficient grids-based DC transmission systems.

The second virtual wind farm presented the analysis of a novel mechanism for riding-through a DC fault of a five-level three-phase MMC as a controller, integrated with a DC-link based WPP with the use of fault blocking diode. A 16 kW, 60 Hz PMSG and wind-turbine integrated with the MSC, and GSC are utilized as wind farm components, along with DC transmission grid. This topology contributes to the stability and reliability of the system by ensuring continuous output power under transient fault conditions. The functional response of the system is presented using PSim software to demonstrate the performance of the proposed controller.

Several modes of operation have been discussed; in the steady-state case, the use of a fault blocking diode does not change the values of a DC and AC output waveforms. In a faulted system mode of operation, with the use of a controller, it was observed that the controller can ride through the DC fault and a stable operation can be obtained from the rectifier and inverter sides. In the absence of the controller, the system collapsed. Therefore, the simulation results show that the proposed control strategy for riding-through a DC-link fault ensures reliable operation of the system during transient faults. Furthermore, the DC bus voltage controller is designed to maintain a constant DC voltage during steady-state operations using the compensated loop gain relation. The stability of the unit is also tested under steady-state conditions using bode plots.

The third virtual wind farm proposes an improved Vienna-I topology with the use of diodes and capacitor sub-module for riding-through AC faults. Three parallel WECUs supplying a DC load are simulated and discussed. It was observed that the suggested sub-module eliminates the fault current effect by creating a separate current path.

Several modes of operation have been simulated and discussed. The simulation results confirm the reliability of the proposed rectifier with FRT module. Fault current can be blocked rapidly to protect power system from overheating problems.

It was observed that the WTG integrated with a proposed sub-module Vienna-I based DC transmission system is a practical candidate that can be employed in large-scale WPPs to realize a stable and reliable operation.

7.2 RECOMMENDATIONS AND FUTURE WORK

The optimal control strategies proposed in this research have demonstrated their ability to ensure an efficient and reliable operation for a WECS. Although the simulation results acquired in this thesis represent those of fully functional design, and the objectives and research questions for this research have been met, the following enhancements are, suggested for future work:

- Experimental validation should be applied for all the three virtual wind farms that have been simulated.
- Implementation of different kinds of PWMs techniques for the Vienna rectifier-I and the MMC converter.
- Higher voltage-level of MMC can be introduced to improve the efficiency and the performance of the MMC.
- Future studies can implement the MMC as a rectifier and inverter in the same WECS and compare the results to the use of Vienna-I as a rectifier.
- The control at the generator-side should be focused on, with the use of the same WPPs implemented for this work. After that, an economic analysis can be conducted comprehensively.
- A comprehensive review of the technological trend of DC collection grid for offshore and onshore wind farm can be undertaken.
- Greater analysis can also be conducted focusing on the HVDC systems that combine various types of modular VSC.

REFERENCES

[1] M. K. Bakhshizadeh, J. Hjerrild, L. Kocewiak, B. Hesselbæk, T. Sørensen, F. Blaabjerg, C. L. Bak, and F. F. da Silva, "Harmonic modelling, propagation and mitigation for large wind power plants connected via long HVAC Cables: review and outlook of current research," presented at *IEEE International Energy Conference (ENERGYCON)*, Leuven, Belgium, 2016.

[2] Z. Guiping, D. Xiaowei, and Z. Chen, "Optimisation of reactive power compensation of HVAC cable in off-shore wind power plant," *IET Renew. Power Gen.*, vol. 9, no. 7, pp. 857-863, 2015.

[3] S. Chaithanya, V. N. B. Reddy, and R. Kiranmayi, "A narrative review on offshore wind power transmission using low frequency AC system," presented at *International Conference on Smart Technology for Smart Nation, Bangalore, India, 2017, pp. 52-58.*

[4] V. Akhmatov, M. Callavik, C. M. Franck, S. E. Rye, T. Ahndorf, M. K. Bucher, H. Muller, F. Schettler, and R. Wiget, "Technical guidelines and prestandardization work for first HVDC grids," *IEEE Trans. Power Del.*, vol. 29, no. 1, pp. 327-335, 2014.

[5] S. Wang, N. Chen, D. Yu, A. Foley, L. Zhu, K. Li, and J. Yu, "Flexible fault ride-through strategy for wind farm clusters in power systems with high wind power penetration," *Energy Conv. and Management*, vol. 93, pp. 239-248, 2015.

[6] S. K. Chaudhary, R. Teodorescu, P. Rodriguez, and P. C. Kjær, "Chopper controlled resistors in VSC-HVDC transmission for WPP with full-scale converters," presented at the *IEEE Sustainable Alternative Energy (SAE) Conf.*, Valencia, Spain, 2009.

[7] X. Ding, Z. Qian, Y. Xie, and Z. Lu, "Three-phase z-source rectifier," presented at the *36th Power Electronics Specialists Conf.*, Recife, Brazil, 2005, pp. 494-500.

[8] H. Krishnamoorthy, M. Daniel, J. Ramos-Ruiz, P. Enjeti, L. Liu, and E. Aeloiza, "Isolated AC–DC converter using medium frequency transformer for off-shore wind turbine DC collection grid," *IEEE Trans. Indust. Electron.*, vol. 64, no. 11, pp. 8939-8947, 2017.

[9] L. Chen, Y. Dai, Y. Min, and K. Hou, "Study on the mechanism of transient voltage stability of wind power with power electronic interface," presented at the *Asia-Pacific Power and Energy Engineering Conf.*, Brisbane, Australia, 2015.

[10] J. Tan, and Y. Zhang, "Coordinated control strategy of a battery energy storage system to support a wind power plant providing multi-time scale frequency ancillary services," *IEEE Trans. Sust. Energy*, vol. 8, no. 3, pp. 1140-1153, 2017.

[11] M. A. Pe˜nalba, O. G. Bellmunt, and M. Martins, "Coordinated control for an offshore wind power plant to provide fault ride through capability," *IEEE Trans. Sust. Energy*, vol. 5, no. 4, pp. 1253-1261, 2014.

[12] I. M. O. Mohammed, M. N. Gitau, R. C. Bansal, and K. Musasa, "Modelling and control of a vienna smart rectifier-I for wind power systems integrated under transient conditions," *Technol. Econ. Smart Grids Sustain. Energy*, vol. 4, no. 2, pp. 1-13, 2019.

[13] J. S. Manguelle, M. H. Todorovic, S. Chi, S. K. Gunturi, and R. Datta, "Power transfer capability of HVAC cables for subsea transmission and distribution systems," *IEEE Trans. Indust. App.*, vol. 50, no. 4, pp. 2382-2391, 2014.

[14] C. J. Chou, Y. K. Wu, G. Y. Han, and C. Y. Lee, "Comparative evaluation of the HVDC and HVAC Links Integrated in a Large Offshore Wind Farm-An Actual Case Study in Taiwan," *IEEE Trans. Indust. App.*, vol. 48, no. 5, pp. 1639-1648, 2012.

[15] E. Muljadi, M. Singh, and V. Gevorgian, "Doubly fed induction generator in an offshore wind power plant operated at rated V/Hz," *IEEE Trans. Indust. App.*, vol. 49, no. 5, pp. 2197-2205, 2013.

[16] E. T´omasson, and L. S¨oder, "Generation adequacy analysis of multi-area power systems with a high share of wind power," *IEEE Trans. Power Syst.*, vol. 33, no. 4, pp. 3854-3862, 2018.

[17] J. Shi, W-J. Lee, and X. Liu, "Generation scheduling optimization of wind-energy storage system based on wind power output fluctuation features," *IEEE Trans. Indust. App.*, vol. 54, no. 1, pp. 10-17, 2018.

[18] Q. Wang, and S. Niu, "Design, modeling, and control of a novel hybrid-excited flux-bidirectional-modulated generator-based wind power generation system," *IEEE Trans. Power Electron.*, vol. 33, no. 4, pp. 3086-3096, 2018.

[19] G. Silva, R. Vieira, and C. Rech, "Discrete-time sliding-mode observer for capacitor voltage control in modular multilevel converters," *IEEE Trans. Indust. Electron.*, vol. 65, no. 1, pp. 876-886, 2018.

[20] A. K. Thet, and H. Saitoh, "Pitch control for improving the low-voltage ride-through of wind farm," presented at the *Transmission & Distribution Conference & Exposition: Asia and Pacific*, 2009.

[21] L. H. Hansen, L. Helle, F. Blaabjerg, E. Ritchie, S. Munk-Nielsen, H. W. Bindner, P. E. Sørensen, and B. Bak-Jensen, "Conceptual survey of generators and power electronics for wind turbines," *Risø National Laboratory*, Roskilde, Denmark 2001.

[22] Y. Xiao-ping, D. Xian-feng, F. Fan, and T. Lu-lin, "Low voltage ride-through of directly driven wind turbine with permanent magnet synchronous generator," presented at the *Power and Energy Engineering Conference (APPEEC)*, Wuhan, China, 2009.

[23] J. F. Conroy, and R. Watson, "Low-voltage ride through of a full converter wind turbine with permanent magnet generator," *IET Renew. Power Gen.*, vol. 1, no. 3, pp. 182-189, 2007.

[24] L. Barote, R. Weissbach, R. Teodorescu, C. Marinescu, and M. Cirstea, "Stand-alone wind system with vanadium redox battery energy storage," presented at the *11th*

International Conference on Optimization of Electrical and Electronic Equipment, Brasov, Romania, 2008.

[25] A. Mullane, G. Lightbody, and R. Yacamini, "Wind-turbine fault ride-through enhancement," *IEEE Trans. Power Sys.*, vol. 20, no. 4, pp. 1929-1937, 2005.

[26] C. Feltes, H. Wrede, F. W. Koch, and I. Erlich, "Enhanced fault ride-through method for wind farms connected to the grid through VSC-based HVDC transmission," *IEEE Trans. Power Sys.*, vol. 24, pp. 1537-1546, Aug. 2009.

[27] F. Deng, and Z. Chen, "Low-voltage ride-through of variable speed wind turbines with permanent magnet synchronous generator," presented at the *35th Annual Conference of IEEE Industrial Electronics*, Porto, Portugal, 2009.

[28] A. C. Lopes, and A. C. Nascimento, "Reactive power control of direct drive synchronous wind generators to enhance the low voltage ride-through capability," presented at the *IREP Symposium Bulk Power System Dynamics and Control-VIII (IREP)*, Rio de Janeiro, Brazil, 2010.

[29] L. Huan-ping, and Y. Jin-ming, "The performance research of large scale wind farm connected to external power grid," presented in *3rd International Conference on Power Electronics Systems and Applications PESA*, Hong Kong, China, pp. 1-5, 2009.

[30] M. H. Ali, and B. Wu, "Comparison of stabilization methods for fixed-speed wind generator systems," *IEEE Trans. Power Del.*, vol. 25, no. 1, pp. 323-331, 2010

[31] M. H. Haque, "Compensation of distribution system voltage sag by dvr and d-statcom," presented in *IEEE Power Tech. Proceedings*, Porto, Portugal, 2001, no. 1.

[32] M. N. Eskander, and S. I. Amer, "Mitigation of voltage dips and swells in grid-connected wind energy conversion systems," presented in *ICCAS-SICE, Fukuoka*, Japan, 2009, pp. 885-890.

[33] S. Raphael, and A. Massoud, "Unified power flow controller for low voltage ride through capability of wind-based renewable energy grid-connected systems," presented at the *8th International Multi-Conference on Systems, Signals & Devices*, Sousse, Tunisia, 2011.

[34] S. Swain, and P. K. Ray, "Short circuit fault analysis in a grid connected DFIG based wind energy system with active crowbar protection circuit for ride through capability and power quality improvement," *Int. J. Electrical Power and Energy Sys.*, vol. 84, pp. 64-75, 2016.

[35] X. Zhang, X. Cao, W. Wang, and C. Yun, "Fault ride-through study of wind turbines," *J. of Power and Energy Eng.*, vol. 1, no. 5, pp. 25-29, 2013.

[36] A. Howlader, and T. Senjyu, "A comprehensive review of low voltage ride through capability strategies for the wind energy conversion systems," *Renewable and Sust. Energy Reviews*, vol. 56, pp. 643-658, 2016.

[37] A. D. Hansen, N. A. Cutululis, H. Markou, P. Sørensen, and F. Iov, "Grid fault and design-basis for wind turbines-Final report," *Risø DTU National Laboratory for Sustainable Energy*, 2010.

[38] J. Yang, "Fault analysis and protection for wind power generation systems," Ph.D. thesis, Electronics and Electrical Engineering, School of Engineering College of Science and Engineering, University of Glasgow, UK, 2011.

[39] V. Yaramasu, A. Dekka, M. J. Duran, S. Kouro, and B. Wu, "PMSG-based wind energy conversion systems: survey on power converters and controls," *IET Electric Power App.*, vol. 11, no. 6, pp. 956-968, 2017.

[40] Y. Zhao, C. Wei, Z. Zhang, and W. Qiao, "A review on position/speed sensor less control for permanent-magnet synchronous machine-based wind energy conversion systems," *IEEE J. of Emerging and Selected Topics in Power Electron.*, vol. 1, no. 4, pp. 203–216, 2013.

[41] B. C. Babu, and K. B. Mohanty, "Experimental validation of improved control strategy of grid-interactive power converter for wind power system," *Technol. Econ. Smart Grids Sustain. Energy*, vol. 2, no. 5, pp. 1-12, 2017.

[42] G. P. Adam, O. Anaya-Lara, G. Burt, S. J. Finney, and B. W. Williams, "Comparison between two VSC-HVDC transmission systems technologies: modular and neutral point clamped multilevel converter," presented at the *35th Annual Conference of IEEE Industrial Electronics*, 2009, pp. 277-282.

[43] X. Li, W. Liu, Q. Song, H. Rao, and S. Xu, "An enhanced MMC topology with DC fault ride-through capability," presented at *39th Annual Conference of the IEEE Industrial Electronics Society IECON*, Vienna, Austria, 2013, pp. 6182-6188.

[44] Z. Bian, and Z. Xu, "Fault ride-through capability enhancement strategy for VSC-HVDC systems supplying for passive industrial installations," *IEEE Trans. Power Del.*, vol. 31, no. 4, pp. 1673-1682, 2016.

[45] E. Kontos, R. Teixeira Pinto, and P. Bauer, "Providing dc fault ride-through capability to H-bridge MMC-based HVDC networks," presented at *9th International Conference on Power Electronics-ECCE Asia*, Seoul, Korea, 2016, pp. 1542-1551.

[46] L. Shi, G. P. Adam, R. Li, and L. Xu, "Control of offshore MMC during asymmetric offshore AC faults for wind power transmission," early access article *IEEE J. of Emerging and Selected Topics in Power Electron.*, pp. 1-10, 2019.

[47] J. Hu, R. Zeng, and Z. He, "DC fault ride-through of MMCs for HVDC systems: a review," *Journal of Engineering*, vol. 2016, no. 9, pp.321-331, 2016.

[48] S. Heinig, K. Jacobs , K. Ilves, L. Bessegato, P. Bakas, S. Norrga, and H. Nee, "Implications of capacitor voltage imbalance on the operation of the semi-full-bridge submodule," *IEEE Trans. Power Electron.*, vol. 34, no. 10, pp. 9520-9535, 2019.

[49] C. Chen, G. P. Adam, S. Finney, J. Fletcher, and B. Williams, "H-bridge modular multi-level converter: control strategy for improved DC fault ride-through capability without converter blocking," *IET Power Electron.*, vol. 8, no. 10, pp.1996-2008, 2015.

[50] R. A. Ibrahim, M. S. Hamad, Y. G. Dessouky, and B. W. Williams, "A review on recent low voltage ride-through solutions for PMSG wind turbine," presented at *International Symposium on Power Electronics*, Electrical Drives, Automation and Motion (SPEEDAM), Sorrento, Italy, 2012.

[51] A. Rath, S. R. Ghatak, and P. Goyal, "Optimal allocation of distributed generation (DGs) and static VAR compensator (SVC) in a power system using revamp voltage stability indicator," presented at *National Power System Conference (NPSC)*, Bhubaneswar, India, 2016.

[52] L. Wu, D. S. Ha, J. Kuang, X. D. Do, and S. G. Lee, "An active rectifier with optimal flip timing for the internal capacitor for piezoelectric vibration energy harvesting," presented at the *IEEE 58th International Midwest Symposium on Circuits and Systems (MWSCAS)*, Fort Collins, CO, USA, 2015.

[53] R. Žatkoviþ, and J. Dudrik, "Novel soft switching DC/DC converter with active rectifier for wide load range," presented at the *International Conference on Electr ical Drives and Power Electronics (EDPE)*, Tatranska Lomnica, Slovakia, 2015.

[54] X. Ding, Z. Qian, Y. Xie, and Z. Lu, "Three-phase Z-source rectifier," presented at the *2005 IEEE 36th Power Electronics Specialists Conference*, Recife, Brazil, 2005.

[55] S. Sabri, E. V. Brunt, A. Barkley, B. Hull, M. O'Loughlin, A. Burk, S. Allen, and J. Palmour, "New generation 6.5 kV SiC power MOSFET," presented at the *IEEE 5th Workshop on Wide Bandgap Power Devices and Applications (WiPDA)*, Research Triangle Park, NC, USA, 2017.

[56] C. L. K. Konga, and M. N. Gitau, "Three-phase quasi-Z-source rectifier modeling," presented at the *Twenty-Seventh Annual IEEE Applied Power Electronics Conference and Exposition (APEC)*, Orlando, FL, USA, 2012.

[57] E. Karaman, M. Farasat, and A. M. Trzynadlowski, "A comparative study of series and cascaded Z-source matrix converters," *IEEE Trans. Indust. Electron.*, vol. 61, no. 10, pp. 5164-5173, 2014.

[58] W. Li, Z. Yuan, B. Lai, and Q. Zhang, "A control method of three-phase Z-source integrated charger with motor windings," presented at the *IEEE Conference on Industrial Electronics and Applications (ICIEA)*, Wuhan, China, 2018.

[59] C. L. K. Konga, M. N. Gitau, and R. C. Bansal, "Steady-state and small-signal models of a three-phase quasi-Z-source AC–DC converter for wind applications," *IET Renew. Power Gen.*, vol. 10, no. 7, pp. 1033–1040, 2016.

[60] Q. Zhang, T. Na, L. Song, and S. Dong, "A novel modulation for soft-switching three-phase quasi-Z-source rectifier without auxiliary circuit," *IEEE Trans. Indust. Electron.*, vol. 65, no. 6, pp. 5157-5166, 2018.

[61] D. Vinnikov, and I. Roasto, "Quasi-Z-source-based isolated DC/DC converters for distributed power generation," *IEEE Trans. Indust. Electron.*, vol. 58, no. 1, pp. 192-201, 2011.

[62] J. W. Kolar, and H. Ertl, "Status of the techniques of three-phase rectifier systems with low effects on the mains," presented at the *21st International Telecommunications Energy Conference*, Copenhagen, Denmark, 1999.

[63] J. S. Lee, and K. B. Lee, "Carrier-based discontinuous PWM method for vienna rectifiers," *IEEE Trans. Power Electron.*, vol. 30, pp. 2896-2900, 2015.

[64] W. Lin, J. Wen, and S. Cheng, "Multiport DC–DC auto transformer for interconnecting multiple high-voltage DC systems at low cost," *IEEE Trans. Power Electron.*, vol. 30, no. 12, pp. 6648-6660, 2015.

[65] J. Yang, Z. He, H. Pang, and G. Tang, "The hybrid-cascaded DC–DC converters suitable for HVDC applications," *IEEE Trans. Power Electron.*, vol. 30, no. 10, pp. 5358-5363, 2015.

[66] W. Lin, "DC–DC auto transformer with bidirectional DC fault isolating capability," *IEEE Trans. Power Electron.*, vol. 31, no. 8, pp. 5400-5410, 2016.

[67] X. Wang, G. Tang, Z. He, X. Wei, H. Pang, and X. X., "Modeling and control of an isolated module multilevel DC/DC converter for DC grid," *CSEE J. of Power and Energy Sys.*, vol. 3, no. 2, pp. 150-159, 2017.

[68] B. W. McConnell, "Applications of high temperature superconductors to direct current electric power transmission and distribution," *IEEE Trans. Applied Super Conductivity*, vol. 15, no. 2, pp. 2142-2145, 2005.

[69] H. Wang, and M.A. Redfern, "The advantages and disadvantages of using HVDC to interconnect AC networks," presented at the *International Universities Power Engineering UPEC*, Cardiff, Wales, UK, 2010.

[70] J. Zhang, and C. Zhao, "The research of SM topology with DC fault tolerance in MMC-HVDC," *IEEE Trans. Power Del.*, vol. 30, no. 3, pp. 1561-1568, 2015.

[71] *Analysis, design and control of voltage source converter based HVDC system*, R. Agarwal, Electrical and Instrumentation Engineering, Deemed University, Sant Logowal Institute of Engineering and Technology, India, 2016.

[72] J. Mohammadi, S. Afsharnia, and S. Vaez-Zadeh, "Efficient fault-ride-through control strategy of DFIG-based wind turbines during the grid faults," *Energy Conv. and Management*, vol. 78, pp. 88-95, 2013.

[73] S. Romphochai, and K. Hongesombut, "Evaluation of fault-ride through capability enhancement of DFIG-based wind turbine with Bi-2212 superconducting fault current limiter," Presented at *Bangkok*, Thailand, 2015.

[74] L. Chen, F. Zheng, C. Deng, Z. Li, and F. Guo, "Fault ride-through capability improvement of DFIG-based wind turbine by employing a voltage-compensation-type active SFCL," *Canadian J. of Electrical and Computer Eng.*, vol. 38, pp. 132-142, 2015.

[75] N. Amutha, and B. K. Kumar, "Improving fault ride-through capability of wind generation system using DVR," *Int. J. Electrical Power and Energy Sys.*, vol. 46, pp. 326-333, 2013.

[76] G. Mokryani, P. Siano, A. Piccolo, and Z. Chen, "Improving fault ride-through capability of variable speed wind turbines in distribution networks," *IEEE Systems Journal*, vol. 7, pp. 713-722, 2013.

[77] A. Rajaei, M. Mohamadian, and A. Y. Varjani, "Vienna-rectifier-based direct torque control of PMSG for wind energy application," *IEEE Trans. Indust. Electron.*, vol. 60, no. 7, pp. 2919-2929, 2013.

[78] T. Gao, S. Zhang, S. Zhang, and J. Zhao, "A dynamic model and modified one-cycle control of three-level front-end rectifier for neutral point voltage balance," *IEEE J. and Magazines*, vol. 5, pp. 2000-2010, 2017.

[79] J. Claire, and G. L. Borgne, "Double boost effect topology for AC/DC converter with unity power factor," presented at the *IEEE Power Electronics Specialists Conf.*, Rhodes, Greece, 2008, pp. 3199-3205.

[80] J. W. Kolar, U. Drofenik, and F. C. Zach, "Vienna rectifier II-a novel single-stage high-frequency isolated three-phase PWM rectifier system," *IEEE Trans. Indust. Electron.*, vol. 46, no. 4, pp. 674-691, 1999.

[81] *Power electronics, converters, applications, and design*, 3rd Ed., N. Mohan, T. M. Undeland, and W. P. Robbins, USA, 2003.

[82] T. Praveen, M. Munish, and J. Pidanic, "A review on microgrid based on hybrid renewable energy sources in South-Asian perspective," *Technol Econ Smart Grids Sustain Energy*, vol. 2, no. 10, pp. 1-16, 2017.

[83] R. M. M. Pereira, C. M. M. Ferreira, and F. P. M. Barbosa, "Comparative study of STATCOM and SVC performance on dynamic voltage collapse of an electric power system with wind generation," *IEEE Latin America Trans.*, vol. 12, no. 2, pp. 138-145, 2014.

[84] K. Musasa, M. N. Gitau, and R. C. Bansal, "Analysis of a DC collector-based power converter topology for an offshore wind farm", *Elect. Power Comp. and Sys.*, vol. 43, no. 8-10, pp. 1113-1121, 2015.

[85] S. Li, K. Zhang, J. Li, and C. Liu, "On the rejection of internal and external disturbances in a wind energy conversion system with direct-driven PMSG," *ISA Trans.*, vol. 61, pp. 95-103, 2016.

[86] R. Errouissi, and A. Al-Durra, "A novel PI-type sliding surface for PMSG-based wind turbine with improved transient performance," *IEEE Trans. Energy conv.*, vol. 33, no. 2, pp. 834-844, 2018.

[87] D. Thakur, and J. Jiang, "Control of a PMSG wind-turbine under asymmetrical voltage sags using sliding mode approach," *IEEE Power and Energy Techn. Sys. J.*, vol. 5, no. 2, pp. 47-55, 2018.

[88] K. Musasa, M. N. Gitau, and R. C. Bansal, "Performance analysis of power converter based active rectifier for an offshore wind park," *Elect. Power Comp. and Sys.*, vol. 43, no. 8-10, pp. 1089-1099, 2015.

[89] Y. Wang, and R. Hai, "Power control of permanent magnet synchronous generator directly driven by wind turbine," *Int. J. of Signal Processing Sys.*, vol. 1, no. 2, pp. 244-249, 2013.

[90] Y. K. Wu, C. Y. Lee, and G. H. Shu, "Taiwan's first large-scale offshore wind farm connection-A real project case study with a comparison of wind turbine," *IEEE Trans. Ind. Appl.*, vol. 47, no. 3, pp. 1461-1469, 2011.

[91] D. Berenguel, M. D. Prada, O. G. Bellmunt, and M. Martins, "Electrical interconnection options analysis for offshore wind farms," presented at the *Europe's Premier Wind Energy Event (EWEA)*, Vienna, Austria, 2013.

[92] G. Q. Varela, G. W. Ault, O. A. Lara, and J. R. McDonald, "Electrical collector system options for large offshore wind farms," *IET Renew. Power Gen.*, vol. 1, no. 2, pp. 107-114, 2007.

[93] M. H. C. Meyer, A. Peterson, and R. W. D. Donckeri, "Control and design of DC grids for offshore wind farms," *IEEE Trans. Ind. App.*, vol. 43, no. 6, pp. 1475-1481, 2007.

[94] K. Meah, and S. Ula, "Comparative evaluation of HVDC and HVAC transmission systems," presented at the *IEEE Power Engineering Society General Meeting, Tampa,* FL, USA, 2007.

[95] K. Musasa, "Design and control of a DC collection grid for offshore wind farm," Ph.D. thesis, Electrical, Electronic and Computer Engineering, Univ. of Pretoria, Pretoria, South Africa, 2016.

[96] S. D. Round, P. Karutz, M. L. Heldwein, and J. W. Kolar, "Towards a 30 kW/liter, three-phase unity power factor rectifier," presented at the *Power Conversion Conf.*, Nagoya, Japan, 2007.

[97] J. Adhikari, P. I. V., and S. K. Panda, "Voltage oriented control of the three-level vienna rectifier using vector control method," presented at the *Applied Power Electronics Conf. and Exposition (APEC)*, Long Beach, USA, 2016.

[98] H. M. Teshnizi, A. Moallem, M. Zolghadri, and M. Ferdowsi, "A dual-frame hybrid vector control of vector-modulated VIENNA I rectifier for unity power factor operation under unbalanced mains condition," presented at the *Applied Power Electronics Conf. and Exposition*, 2008, Austin, USA, pp. 1402-1408.

[99] L. Hang, H. Zhang, S. Liu, X. Xie, C. Zhao, and S. Liu, "A novel control strategy based on natural frame for Vienna-Type rectifier under light unbalanced-grid conditions," *IEEE Trans. Indust. Electron.*, vol. 62, no. 3, pp. 1353-1362, 2015.

[100] X. Jiang, J. Yang, J. Han, and T. Tang, "A survey of cascaded multi-level PWM rectifier with VIENNA modules for HVDC system," presented at the *International Power Electronics and Application Conference and Exposition*, Shanghai, China, 2014.

[101] N. B. H. Youssef, K. Al-Haddad, and H. Y. Kanaan, "Implementation of a new linear control technique based on experimentally validated small-signal model of three-phase three-level boost-type vienna rectifier," *IEEE Trans. Indust. Electron.*, vol. 55, no. 4, pp. 1666- 1675, 2008.

[102] A. Lesnicar, and R. Marquardt, "An innovative modular multilevel converter topology suitable for a wide power range," presented at the *IEEE Power Tech Conf.*, Bologna, Italy, 2003.

[103] G. J. Kish, and P. W. Lehn, "Linearized DC-MMC models for control design accounting for multifrequency power transfer mechanisms," *IEEE Trans. Power Del.*, vol. 33, no. 1, pp. 271-281, 2018.

[104] T. Nguyen, and D. Lee, "A novel submodule topology of MMC for blocking DC-fault currents in HVDC transmission systems," *9th International Conf. on Power Electronics-ECCE Asia*, Seoul, Korea, pp. 2057-2063, 2015.

[105] R. Li, J. Fletcher, L. Xu, D. Holliday, and B. Williams, "A hybrid modular multilevel converter with novel three-level cells for DC fault blocking capability," *IEEE Trans. Power Del.*, vol. 30, no. 4, pp. 2017-2026, 2015.

[106] X. Li, W. Liu, Q. Song, H. Rao, and S. Xu, "An enhanced MMC topology with dc fault ride-through capability," presented at the *39th Annual Conference of the IEEE Industrial Electronics Society*, Vienna, Austria, 2013.

[107] S. Lee, and Y. Heng, "A tuning-less model predictive control for modular multilevel converter capable of unbalanced grid fault," *Int. J. Elect. Power and Energy Sys.*, vol. 94, pp. 213-224, 2018.

[108] G. S. da Silva, R. P. Vieira, and C. Rech, "Discrete-time sliding-mode observer for capacitor voltage control in modular multilevel converters," *IEEE Trans. Indust. Electron.*, vol. 65, no. 1, pp. 876-886, 2018.

[109] A. Jamshidifar, and D. Jovcic, "Small-signal dynamic DQ model of modular multilevel converter for system studies," *IEEE Trans. Power Del.*, vol. 31, no. 1, pp. 191-199, 2016.

[110] J. Freytes, G. Bergna, J. A. Suul, S. D'Arco, F. Gruson, F. Colas, H. Saad, and X. Guillaud, "Improving small-signal stability of an MMC with CCSC by control of the internally stored energy," *IEEE Trans. Power Del.*, vol. 33, no. 1, pp. 429-439, 2018.

[111] *Voltage-sourced converters in power systems: modelling, control and applications*, A. Yazadani, and R. Iravani, Hoboken, New Jersey and Canada, 2010.

[112] D. G. Holmes, T. A. Lipo, B. P. McGrath, and W. Y. Kong "Optimized design of stationary frame three phase AC current regulators," *IEEE Trans. Power Electron.*, vol. 24, pp. 2417-2426, 2009.

[113] Y. Yang, K. Zhou, and F. Blaabjerg, "Enhancing the frequency adaptability of periodic current controllers with a fixed sampling rate for grid-connected power converters," *IEEE Trans. Power Electron.*, vol. 31, no. 10, pp. 7273-7285, 2016.

[114] R. Erickson, and D. M. vic, *Switch realization in fundamentals of power electronics*, 2nd ed., New York, Boston: Secaucus, 2000, pp. 63-101, 377-400.

[115] S. Golestan, M. Monfared, F. D. Freijedo, and J. M. Guerrero, "Advantages and challenges of a type-3 PLL," *IEEE Trans. Power Electron.*, vol. 28, no. 11, pp. 4985-4997, 2013.

[116] S. Zhou, X. Zou, D. Zhu, L. Tong, Y. Zhao, Y. Kang, and X. Yuan, "An improved design of current controller for LCL-type grid-connected converter to reduce negative effect of PLL in weak grid," *IEEE J. of Emerging and Selected Topics in Power Electron.*, vol. 6, no. 2, pp. 648-663, 2018.

[117] S. Golestan, M. Ramezani, J. M. Guerrero, and M. Monfared, "dq-frame cascaded delayed signal cancellation-based PLL: analysis, design, and comparison with moving average filter-based PLL," *IEEE Trans. power Electron.*, vol. 30, no. 3, pp. 1618-1632, 2015.

[118] A. F. Zobaa, and R. C. Bansal, *Handbook of renewable energy technology*, 1st edition, World Scientific Publishing Company, Singapore, 2011.

[119] F. de Bosio, M. Pastorelli, L. A.de S. Ribeiro, M. S. Lima, F. Freijedo, and J. M. Guerrero, "Current control loop design and analysis based on resonant regulators for microgrid applications," presented at the *IEEE Indust. Electron. Conf.*, Yokohama, Japan, 2015.

[120] S. Howell, S. Filizadeh, and A. M. Gole, "Unidirectional HVDC topology with DC fault ride-through capability," *Canadian J. of Electrical and Computer Eng.*, vol. 40, no. 1, pp. 41-49, 2017.

[121] P.M. Anderson, Analysis of faulted power systems, IEEE press, 1995.

[122] M. Stemmle, C. Neumann, F. Merschel, U. Schwing, K. Weck, M. Noe, F. Breuer, and S. Elschner, "Analsis of unsymmetrical faults in high voltage power systems with superconducting fault current limiters," *IEEE Trans. Applied Supperconduc.*, vol. 17, no. 2, pp. 2347-2350, 2007.

[123] L. Max, "Design and control of a DC collection grid for a wind farm," Ph.D. thesis, Chalmers Univ. of Technology, Sweden, 2009.

[124] C. Wessels, N. Hoffmann, M. Molinas, and F. W. Fuchs, "Stat com control at wind farms with fixed-speed induction generators under asymmetrical grid faults," *IEEE Trans. Indust. Electron.*, vol. 60, no. 7, pp. 2864-2873, 2013.

[125] M. Stemmle, C. Neumann, F. Merschel, U. Schwing, K. H. Weck, M. Noe, F. Breuer, and S. Elschner, "Analysis of unsymmetrical faults in high voltage power systems with superconducting fault current limiters," *IEEE Trans. on Applied Superconductivity*, vol. 17, no. 2, pp. 2347-2350, 2007.

[126] Y. Zhao, J. Palma, J. Mosesian, R. Lyons, Jr., and B. Lehman B, "Line–line fault analysis and protection challenges in solar photovoltaic arrays," *IEEE Trans. Power Del.*, vol. 60, no. 9, pp. 3784-3795, 2013.

ADDENDUM A

A.1 THE TRANSFER-FUNCTION PARAMETERS

A.1.1 ($G_{ab\beta\gamma}$) calculations

The equations that represent the transfer-functions drawn in section 4.3 are shown as follows:

$$G_{id11}(s) = -\frac{V_o^*}{2L}\frac{(S^2+\delta_{11}S)}{den(s)} \tag{A.1}$$

where $den(s) = S^3 + \tau_0 S^2 + (\omega_0^2\delta_{12} + \delta_{13})S + \tau_0\omega_0^2$ (A.2)

$$G_{id12}(s) = -\frac{V_o^*\omega_0}{2L}\frac{(S+\delta_{11})}{den(s)} \tag{A.3}$$

$$G_{id13}(s) = 0 \tag{A.4}$$

$$G_{id21}(s) = -\frac{V_o^*\omega_0}{2L}\frac{(\delta_{11}S+\tau_0)}{den(s)} \tag{A.5}$$

$$G_{id22}(s) = -\frac{V_o^*}{2L}\frac{(S^2+\tau_o S+\delta_{13})}{den(s)} \tag{A.6}$$

$$G_{id23}(s) = 0 \tag{A.7}$$

$$G_{iv11}(s) = \frac{(S^2+\tau_o S+\delta_{16})}{L\times den(s)} \tag{A.8}$$

$$G_{iv12}(s) = \frac{\omega_0}{L}\frac{(S^2+\delta_{11})}{den(s)} \tag{A.9}$$

$$G_{iv21}(s) = -\frac{\omega_0}{L}\frac{(S^2+\delta_{17})}{den(s)} \tag{A.10}$$

$$G_{iv22}(s) = \frac{(S^2+\tau_0 S+\delta_{13})}{L\times den(s)} \tag{A.11}$$

$$G_{vd11}(s) = \frac{3\sqrt{2}\times I_s^*}{2\times C_0}\frac{(S^2+\delta_{14}S)}{den(s)} \tag{A.12}$$

$$G_{vd12}(s) = \frac{3\sqrt{2}\times I_S^*\times\omega_0}{2\times C_0}\frac{(S^2+\delta_{14})}{den(s)} \quad (A.13)$$

$$G_{vd13}(s) = 0 \quad (A.14)$$

$$G_{\Delta vd11}(s) = 0 \quad (A.15)$$

$$G_{\Delta vd12}(s) = 0 \quad (A.16)$$

$$G_{\Delta vd13}(s) = \frac{\delta_{11}\sqrt{2}\times I_S^*}{C_0\times(S+\delta_{15})} \quad (A.17)$$

$$G_{vv11}(s) = \frac{3\sqrt{2}\times V_S}{L\times C_0\times V_0^*}\times\frac{S+\delta_{18}}{den(s)} \quad (A.18)$$

$$G_{vv12}(s) = -\frac{3\sqrt{2}\times I_S^*\times\omega_0}{C_0\times V_0^*}\times\frac{(S-\delta_{14})}{den(s)} \quad (A.19)$$

$$G_{\Delta vv11}(s) = 0 \quad (A.20)$$

$$G_{\Delta vv12}(s) = 0 \quad (A.21)$$

A.1.2 ($G_{ab\beta\gamma}$) parameters calculations

The parameters that can solve the transfer-function equations shown in Section A.1 are represented as follows:

$$\tau_0 = \frac{1}{C_oR_o} = \frac{1}{2000\times 10\text{^}-6\times 50} = 10 \quad (A.22)$$

$$\delta_{11} = \tau_0 + \frac{6V_S\times I_S^*}{C_o\times V_o^{*2}} = 310 \quad (A.23)$$

$$\delta_{12} = 1 + \frac{6L\times I_S^{*2}}{C_o\times V_o^{*2}} = 1.06 \quad (A.24)$$

$$\delta_{13} = \frac{6V_S^2}{LC_oV_o^{*2}} = 1.5\times 10^6 \quad (A.25)$$

$$\delta_{14} = -\frac{V_S}{LI_S^*} = -0.2\times 10^6 \quad (A.26)$$

$$\delta_{15} \cong 2\tau_0 = 20 \quad (A.27)$$

$$\delta_{16} = \frac{6\times L\times\omega_0^2\times I_S^{*2}}{C_o\times V_o^{*2}} = 8527.3 \quad (A.28)$$

$$\delta_{17} = \tau_0 + \frac{6\times V_S\times I_S^{*2}}{C_o\times V_o^{*2}} = 12010 \quad (A.29)$$

$$\delta_{18} = L\omega_0^2 I_S^* = 79.6\times 10^6 \quad (A.30)$$

$$den(s) = S^3 + \tau_0 S^2 + (\omega_0^2 \delta_{12} + \delta_{13})S + \tau_0 \omega_0^2 = S^3 + 10S^2 + (1.65 \times 10^6)S + (1.4 \times 10^6) \quad (A.31)$$

A.2 THE TRANSFER-FUNCTION PARAMETERS MODEL

By using transfer-functions that are demonstrated in A.1, Figure A. 2 can be obtained.

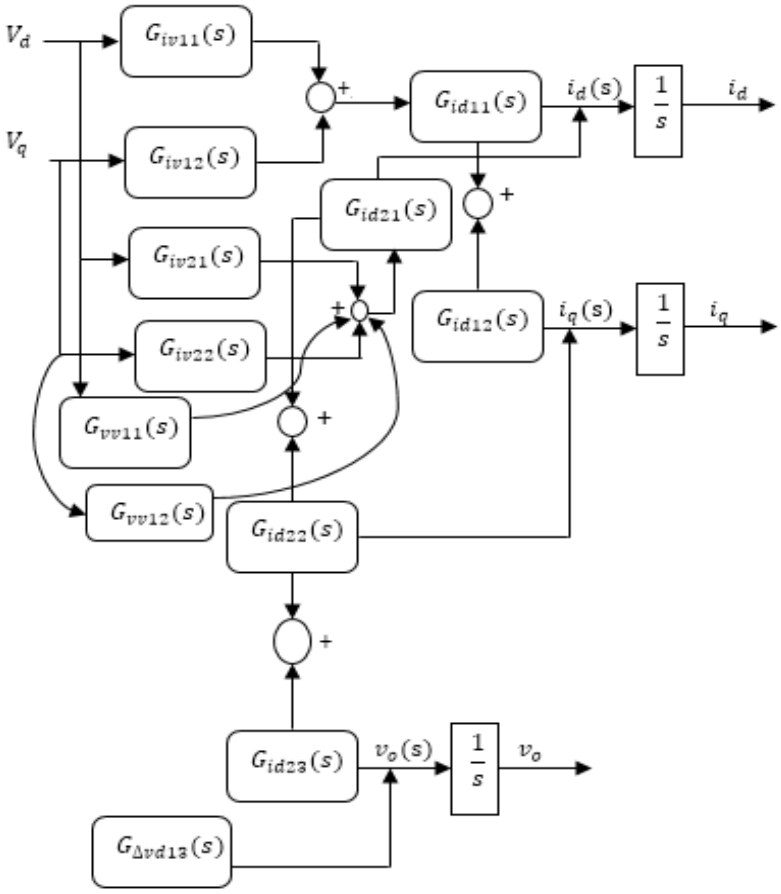

Figure A.2. Summarized model transfer-function block diagram of the proposed rectifier in small-signal procedure.